A Study of the Effects of Stochastic Inertial Sensor Errors

in Dead-Reckoning Navigation

Except where reference is made to the work of others, the work described in this thesis is my own or was done in collaboration with my advisory committee. This thesis does not include proprietary or classified information.

John H. Wall

Certificate of Approval:

George T. Flowers
Professor
Mechanical Engineering

David M. Bevly, Chair
Assistant Professor
Mechanical Engineering

John Y. Hung
Professor
Electrical and Computer Engineering

Joe F. Pittman
Interim Dean
Graduate School

A Study of the Effects of Stochastic Inertial Sensor Errors in Dead-Reckoning Navigation

John H. Wall

A Thesis

Submitted to

the Graduate Faculty of

Auburn University

in Partial Fulfillment of the

Requirements for the

Degree of

Master of Science

Auburn, Alabama
August 4, 2007

A Study of the Effects of Stochastic Inertial Sensor Errors in Dead-Reckoning Navigation

John H. Wall

Signature of Author

Date of Graduation

Thesis Abstract

A Study of the Effects of Stochastic Inertial Sensor Errors in Dead-Reckoning Navigation

John H. Wall

Master of Science, August 4, 2007
(B.S.M.E., Christian Brothers University, 2005)

144 Typed Pages

Directed by David M. Bevly

The research presented in this thesis seeks to quantify the error growth of navigation frame attitude, velocity, and position as solely derived from acceleration and rotation-rate measurements from a strapdown Inertial Measurement Unit (IMU). The wide-spread availability of the Global Positioning System (GPS) and increased technological advances in Inertial Navigation Systems (INS) technology has made possible the use of increasingly affordable and compact GPS/INS navigation systems. While the fusion of GPS and inertial sensing technology offers exceptional performance under nominal conditions, the accuracy of the provided solution degrades rapidly when traveling under bridges, dense foliage, or in urban canyons due to loss of communication with GPS satellites. The degradation of the navigation solution in this inertial dead-reckoning mode is a direct result of the numerical integration of stochastic errors exhibited by the inertial sensors themselves. As the accuracy of the GPS/INS combined system depends heavily on the standalone performance of the INS, firm quantification of the performance of inertial dead-reckoning is imperative for system selection and design.

To provide quantification of the accuracy of inertial dead-reckoning, stochastic models are selected which approximate the noise and bias drift present on a wide variety of both accelerometers and rate-gyroscopes. The stochastic identification techniques of Allan variance and experimental autocorrelation are presented to illustrate the extraction of process parameters from experimental data using the assumed model forms. The selected models are then used to develop analytical expressions for the variance of subsequent integrations of the stochastic error processes. The resulting analytical expressions are validated using Monte Carlo simulations. The analytical analysis is extended to a simple navigation scenario in which a vehicle is constrained to travel on a planar surface with no lateral velocity. Monte Carlo simulation techniques are employed to exemplify and compare the expected results of inertial navigation in higher dynamic scenarios.

Acknowledgments

I would like to thank my thesis advisor, Dr. David Bevly, for providing me with the invaluable opportunity to work as a graduate research assistant in the GPS and Vehicle Dynamics Lab (GAVLab) at Auburn University. His ever enthusiastic vigor for new research and his comfortable attitude made my experience as a master's student most rewarding. I also give thanks to Dr. George Flowers for his warm welcome to Auburn and support throughout my time in the program.

I owe much of my success as a student and researcher to all the students in the GAVLab. My sincere gratitude is due to my fellow labmates for their helping hands in the theoretical and experimental and the willingness with which they shared their expertise.

I thank my brother, Michael, for his multi-dimensional support as a roommate, friend, and technical advisor. I thank my parents, who have given their unconditional love and support. I thank Julia, for her earnest ear and ardent companionship that has kept my spirit high throughout this entire experience.

Style manual or journal used Journal of Approximation Theory (together with the style known as "aums"). Bibliography follows the IEEE Transactions format.

Computer software used The document preparation package TEX (specifically LATEX) together with the departmental style-file `aums.sty`.

Table of Contents

List of Figures

Chapter 1

Introduction

1.1 Overview

With the wide-spread availability of the Global Positioning System (GPS) and continued technological advances in Inertial Navigation Systems (INS), the field of navigation continues to exploit these ever expanding resources. One of the most popular methods of current-day navigation involves the synergy of these two systems and is commonly known as GPS/INS integration. The basic idea of the GPS/INS navigation approach is to utilize the complementary strengths and weaknesses of each system in order to navigate with accuracy superior to that of either component system's stand alone performance. GPS provides precise global position, velocity, and heading information, but updates at a relatively slow rate, is subject to interference, and requires a clear view of the sky. The INS most commonly consists of an *inertial measurement unit* (IMU) which is typically attached rigidly to the frame of the navigating body. The IMU is a device in which three *accelerometers* and three *rate-gyroscopes* (referred henceforth simply as *rate-gyros*) are orthogonally mounted in a sealed unit. Its purpose is to measure the body accelerations and rotation rates in the corresponding component directions and about the corresponding axes as defined by its alignment on the vehicle. The inertial sensors which make up an IMU are available in a wide-variety of grades determined by the basic principle of operation, quality of materials, and integrity of methods/design. The accelerometers and rate-gyros, as with many electronic sensors, are corrupted by stochastic-type disturbances (noise) which manifest themselves on the

sampled output of the device as random variables. The characteristics of these random variables depend upon the principle of operation and integrity of materials/methods used to produce the device. To achieve navigation information from such an INS, the outputs must be numerically integrated and transformed to attain the desired attitude, velocity, and position information. Due to the stochastic errors on the sensors, the integral values exhibit an ever increasing variance. Therefore, in contrast to GPS, Inertial Navigation Systems provide high update information, but will digress with time without corrections. In summary, the GPS/INS combined system uses the high update inertial measurements of the INS to boost the slow rate of the position information from GPS.

The most common GPS/INS approach employs an optimal estimation technique known as the *Kalman Filter* [1]. This *Navigation Kalman Filter* numerically blends the high-rate, short term accuracy of the INS with the long term accuracy of the GPS in an optimal way. Many variations and approaches of the GPS/INS Kalman Filtering method have been researched with the intent of providing the best possible navigation solution. The loosely-coupled GPS/INS uses the common measurements from a standard receiver and requires at least four satellites for normal operation. More advanced approaches such as tightly-coupled and deeply-integrated GPS/INS probe deeper within the GPS receiver and blend the INS with more of the available GPS information. Both of these methods intend to improve some of the weaknesses of the common GPS/INS system for more robust navigation performance [2]. In addition to the GPS/INS only approach, researchers have also developed and implemented navigation systems which include other aiding measurements such as vision [3, 4], odometry [5], and laser-scanners [6]. These additional measurements supplement the existing GPS/INS system to improve the overall navigation performance, especially during GPS outages.

For the case when GPS is unavailable, the INS and other sensors become the sole means of navigation, and the accuracy of the attitude, velocity and position information as derived from body-frame-only measurements degrades with time. This GPS-less navigation mode is known as *dead-reckoning* whereby the body in motion navigates only with information on board itself. The characteristic error growth in the dead-reckoning mode depends upon the amount of time since the GPS signal outage, the equations used in providing the navigation solution (kinematics of vehicle motion), and the integrity of the sensors used to dead-reckon.

The particular focus of the research presented in this text is to perform an analysis of inertial-only navigation in which both GPS and other sensors are not used. This analysis provides a quantification of the dead-reckoning accuracy of the GPS/INS system when GPS is unavailable. As there are many different types and grades of inertial measurement units, the navigation system designer is charged with the tasks of selecting an IMU appropriate for the environment in which it will be employed, the budget of the project, and specific objectives of the final system. The typical manufacturer specifications of the raw inertial measurement errors do not fully depict its performance as a navigation means. That is, they fail to provide the information necessary to firmly quantify the navigation performance of an IMU within the common scenarios encountered. The common specifications from the sensor manufacturer provide only a rough quantification of the raw output of the sensors; no information of the propagated error is available. Therefore, to accurately compare and distinguish the dead-reckoning performance of the many varieties of IMUs, an analysis of the integrated inertial measurements is imperative.

1.2 Prior Art

GPS/INS integration is a very widely implemented and studied scheme as it provides high rate (100 Hz) and high accuracy positioning (1-10 meters) information to a navigating vehicle at a reasonable cost [2]. As GPS is susceptible to signal loss, the performance of the GPS/INS system is often quantified by its INS-only (i.e. dead-reckoning) performance. Approaches to the quantification of the INS-only navigation performance have been based heavily on experimental results. Techniques such as parametric modeling of IMU-derived positioning data [7] and comparisons based on the use of vehicle dynamics in mechanization algorithms [8] all intend to quantify the performance of the GPS/INS system during GPS outages. These post-processing analyses, while giving precise information about the INS-only system performance for particular experimental cases, fail to provide information in support of the general performance of inertial dead-reckoning. In support of the more general approach to the quantification of performance of inertial dead-reckoning, research has been conducted in which the analysis commences with initial investigation of the inertial sensor errors themselves. Such approaches have investigated the characteristics of the stochastic behavior of the raw inertial sensor outputs by using experimental identification techniques of Allan variance [9, 10, 11, 12, 13], and autocorrelation [11, 14]. Based on stochastic error models selected using the identification techniques, the research has been extended to provide the exact error growth of the integral values of the stochastic process [11]. Other researchers following the same path, have investigated the analytical propagation of error into the navigation solution when mechanized in simple scenarios [14, 15]. These propagation analyses, however, have restricted their analytical study to the the effect of white (wide-band) noise on

the navigation solution thereby neglecting significant effects due to sensor bias-drift [14]. The research presented in this thesis has expanded the previous analytical work to include analytical results of the influence of both wide-band noise and sensor drift on the integral sensor outputs. Additional studies of the sensor errors in more complex vehicle motion and mechanization methods are presented as well.

1.3 Contributions

To accomplish the goals of this research, this thesis presents a study of the stochastic inertial sensor error characteristics to provide a practical quantification of the uncertainty growth when dead-reckoning with inertial measurements. This quantification provides the a priori information on the performance of GPS/INS/AuxSensor navigation in support of the system designer's goal of achieving the best navigation performance within the criteria of given objectives. The research presented provides quantification of inertial navigation through:

- Proposing a candidate sensor model sufficient to capture the stochastic behavior of inertial sensor outputs and detailing the means by which the model parameters may be identified.
- Development of expressions for the variance of the integrated values of the inertial sensor error sources.
- An analysis on the relative influence of sensor error model parameters on the variance of integrated outputs.
- A study of the propagation of inertial sensor errors into the navigation equations for a vehicle kinematically constrained in a two-dimensional scenario.

- A comparison of the influence of the navigation equations on the performance of inertial navigation under various vehicle motion assumptions.

1.4 Thesis Organization

Chapter 2 introduces a simple inertial error model consisting of the sum of two stationary Gaussian random processes. The processes model the stochastic behavior of white noise and sensor bias drift observed on both accelerometers and rate-gyros. The means of experimental identification of the specific error process parameters with the use of Allan variance and Autocorrelation techniques are presented.

Chapter 3, the heart of this research, utilizes the stochastic models presented in Chapter 2 to derive analytical expressions for the variance of numerically integrated and double-integrated error processes. The derived expressions are validated using Monte Carlo computer simulations with fixed parameters. A simple example is used to illustrate the applicability of the integrated error variance expressions for a simple single-axis navigation scenario. This chapter concludes its contribution with a study of the effects of the stochastic error process parameters on the integrated sensor error growth.

Chapter 4 applies the information from Chapter 3 to study a simple navigation scenario in which a vehicle travels on a flat plane with no lateral velocity (i.e no side-slip). Expressions for the variance of 2-D velocity error are derived in closed-form and the framework for 2-D position error is shown. The analysis is then extended to the more general 2-D case where a vehicle experiences side-slip and exhibits lateral velocity. A Monte Carlo computer simulation is used to show the additional error when no-slip trajectory is processed with the assumed-slip equations.

Chapter 5 introduces the six degrees-of-freedom (6-DOF) navigation equations as required for the inertial navigation of a body experiencing motion in the most general sense. The characteristics of the error for the 6-DOF inertial navigation scenario are exemplified with the use a computer simulation. In the simulation, the inertial navigation error from the 6-DOF method is compared to the planar navigation method for a planar vehicle trajectory. The purpose of this chapter is to show the effect of additional sensors and transformations when they are not required.

Chapter 6 concludes the work of this thesis with a summary of the results, discussion of the various assumptions and approximations employed in the text, and suggestions for future research.

Chapter 2

Inertial Sensor Modeling

2.1 Introduction

A preliminary step in describing the behavior of inertial navigation error is to determine appropriate error models of the inertial sensors themselves. This chapter presents a simple inertial sensor model sufficient to describe the approximate stochastic nature of the outputs of both accelerometers and rate-gyros across the range of available devices. The identification of the models of two random processes presented in this chapter, have been well researched by many authors including [9, 11, 16] and the applicable techniques and limitations of these methods are presented proceeding the models in the following sections.

2.2 Simple Sensor Models

Simple stochastic sensor models are selected to provide approximate representations to the behavior of that observed on a wide range of inertial measurement sensors. These simple models apply to both accelerometers and rate-gyros and lend themselves well for deriving analytical results which quantify the propagation of sensor errors into their processed states. Although more advanced stochastic models could be developed, the simpler models provide approximations in support of the goals of this thesis: closed-form expressions for the error growth when dead-reckoning with inertial measurements.

The general inertial measurement model used in this study has the form of Equation (2.1) and is suitable for either an accelerometer or rate-gyro.

$$y_{meas} = (SF)\, y + \epsilon + c \tag{2.1}$$

y	is the true sensor value
ϵ	are stochastic 'static' terms
c	is the constant bias
SF	is the scale factor

The scale factor, though shown in [17] to exhibit some stochastic behavior throughout the range of sensor motion and temperature, is assumed to have fixed relationship between the sensor's input and output. The bias, c is also a fixed quantity, exhibits a deterministic behavior with respect to the motion the sensor is sensing. Simple calibration techniques can easily ascertain the scale-factor and constant bias and are thus removable prior to implementation. The stochastic terms however, are not predictable and remain even on a calibrated sensor output. Therefore, a fully calibrated static sensor output as measured can be described by Equation (2.2).

$$y_{meas} = \epsilon \tag{2.2}$$

The stochastic terms, ϵ, are, at this point in the heuristic approach, unknown. The following section introduces simple stochastic processes which intend to capture the unpredictable stochastic behavior of the calibrated sensor output.

2.3 Stochastic Sensor Models

2.3.1 Gaussian White Noise

Inspection of a short-duration static sensor output reveals that the value of the signal jumps from one value to the next in an unpredictable, or random, manner. Successive samples in time of such a signal are described as *uncorrelated* from one time-step to the next. A random process whose successive values in time are uncorrelated is known as a *white noise* process. While the conceptual abstraction of white noise implies that there is infinite frequency content in the process, the sensor output is better described by *wide-band noise*. As as the frequency content of a signal is limited by sampling equipment, materials, and other phenomena, *wide-band* noise is, like white-noise, uncorrelated, but for all measurable or applicable frequencies.

Closer observations of the short-duration static output indicate that the values of the static output at any given time are scattered in higher density about some mean value and becoming scarcer with increasing value from the mean. A good statistical model for this scattering of the data is the Gaussian or Normal Distribution, whose probability density function is given by Equation (2.3).

$$f_X(x) = \frac{1}{\sqrt{2\pi}\sigma_x} \exp\left[-\frac{1}{2}\left(\frac{x - m_x}{\sigma_x}\right)^2\right] \tag{2.3}$$

m_x is the mean of random variable x

σ_x is the standard deviation of random variable x

Complete probabilistic characterization of a random variable, x, with a Gaussian distribution requires knowledge only of the mean value, m_x, and variance ${\sigma^2}_x$. Therefore, for the uncorrelated wide-band Gaussian noise process, the sensor output value at any time is described by a Gaussian distribution with the same mean and variance. Therefore, each successive time sample of the process is *independent* (i.e. no relationship exists between the values from one step to the next). An example of a zero mean, unit-variance Gaussian wide-band noise process is shown in Figure 2.1.

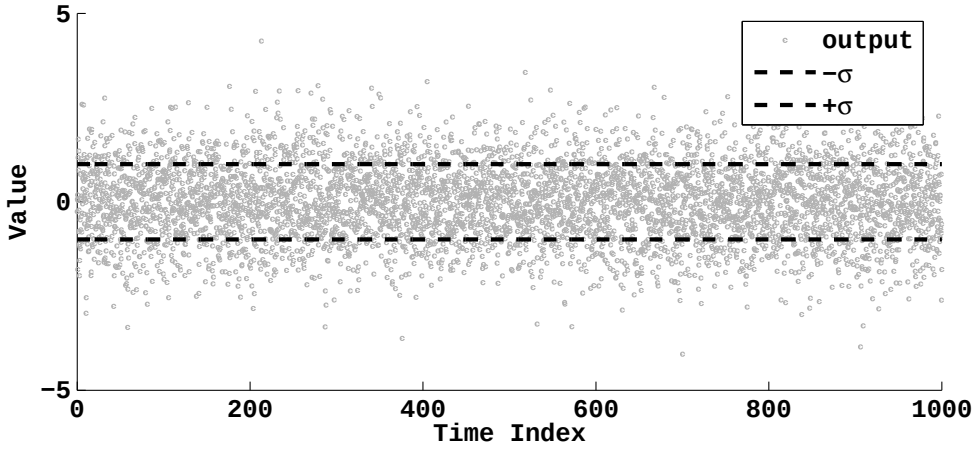

Figure 2.1: Sample Plot of Wide Band Noise, $\sigma^2 = 1$

For high grade sensors, the static output for short time durations (order of minutes) can solely be described by a wide-band noise process. However as the cost of sensor decreases, the integrity of the its output also decreases and other stochastic phenomena can be observed on the measurement. The output of lower-grade sensors exhibit both uncorrelated (wide-band) noise and additional stochastic noises which exhibit varying levels of time correlation, discontinuity, and other irregularities. The discontinuities and irregularities pose a problem in stochastic characterization as their presence dominates in

less-expensive sensor outputs. As a result, a significant amount of study has been dedicated to the development of sophisticated models that accurately capture such low-grade sensor behaviors. However, for the purpose of this research, a simple stochastic model is selected to provide a conservative approximation to the bias drift in accordance with the practical utility of the modeling approach of this thesis. The dominant phenomena on the low grade sensors often materialize as a slowly wandering error in the output and are often referred to as a sensor's *drifting bias*, or *bias drift*. The following section presents an approximate model for this stochastic drifting behavior.

2.3.2 The Gauss-Markov Process

The *1st-order Gauss-Markov process* has been used extensively in the navigation and estimation community to model the various stochastic drift characteristics present on many types of navigation system outputs [11, 18]. For the purpose of the research goals of this thesis, this process provides a conservative approximation to the observed bias drift on many inertial measurements.

A random process is said to be *Markovian* if its probability density function (PDF) at any point in future time can be completely specified with the knowledge of the process PDF at the current time. The Markovian property is analogous to the concept in linear state-space systems whereby the future states can be ascertained by current states and inputs. A *Gauss-Markov* process is a stochastic process whose underlying random phenomenon that drives the process is as a Gaussian sequence of random variables [19].

A commonly used 1st-order Gauss-Markov process model is simply the output of a low-pass filter with a zero-mean white noise input. The governing stochastic linear differential equation for such a process is expressed as

$$\dot{b} = -\frac{b}{\tau} + \omega_b \tag{2.4}$$

τ is the time constant

ω_b is a zero mean Gaussian random variable with variance, $\sigma^2_{\omega_b}$

The process given by Equation (2.4), in continuous time, is somewhat of an abstraction of the more applicable discrete version of the Gauss-Markov process (or sequence). This stochastic sequence is given by the linear stochastic difference Equation (2.5).

$$\begin{aligned} b_k &= \Phi_k b_{k-1} + w_{bk} \\ \Phi_k &= e^{-\frac{\Delta t_k}{\tau}} \end{aligned} \tag{2.5}$$

Φ is the state-transition matrix for the process

w_b is a zero mean Gaussian random variable with variance, $\sigma^2_{w_b}$

As seen by Equation (2.5) the process output is the sum of the Gaussian driving noise, ω, and past values of itself. The output of the process therefore can also be described by a Gaussian distribution and can be completely probabilistically characterized by its mean and variance functions. In contrast to wide-band noise, however, the Markov process exhibits a non-zero time correlation for any given realization of the process because of its dependence on its past values. This correlation characteristic is what causes

the process to appear as a slowly drifting bias, which is the desired model. One such example of the Gauss-Markov process is shown in Figure 2.2.

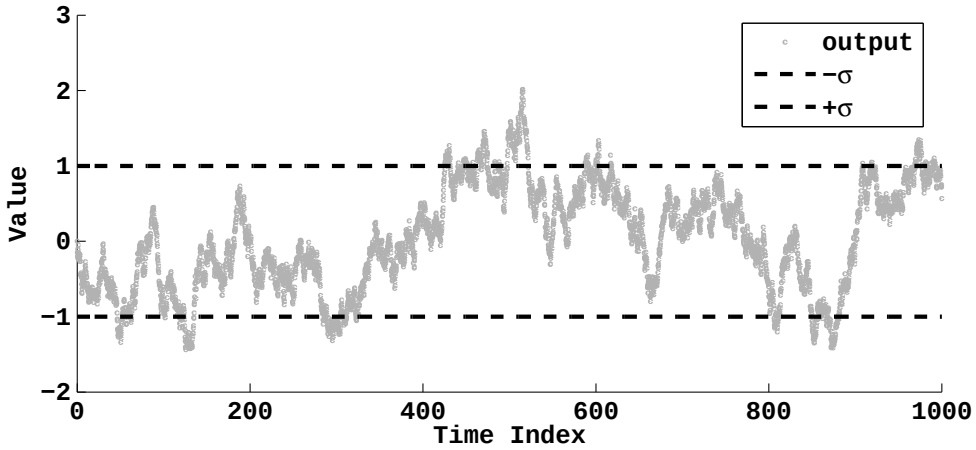

Figure 2.2: Sample Plot of Gauss-Markov process, ${\sigma^2}_b = 1$, $\tau = 100$

Since the driving process is zero mean and Gaussian, the output of the process is zero mean and Gaussian with a transformed variance. Since the time constant is a value greater than the sampling frequency (generally much larger), the characteristic root of the 1^{st}-order Markov dynamics is inside the unit circle, and thus the process is stable. The stability of the process indicates that the variance of its output will reach a steady state value after some initial settling time at which point the process is considered to be *stationary*. Once steady state has reached, the process autocorrelation function takes the form of Equation (2.6).

$$R_{bb}(T) = {\sigma_b}^2 e^{-T/\tau} \tag{2.6}$$

τ is the time constant or correlation time

σ_b is the variance of the process $\sigma^2_{\omega_k}$

The simple autocorrelation expression lends itself well to experimental identification as it is straightforward to extract the magnitude and time constant of the process from a given plot of (2.6). Due to the form of Equation (2.6), the Gauss-Markov process is also referred to as *exponentially correlated noise* [16].

2.3.3 A Simple Stochastic Model

For short time intervals an inertial sensor's output appears as uncorrelated noise (white noise); however for longer time intervals the sensor exhibits a correlated noise (drifting bias). An approximate model of this behavior is simply the sum of the two random processes introduced in the previous sections. The error due to the stochastic behavior of an inertial sensor at time step, k, can thus be described by Equation (2.7).

$$\epsilon_k = \omega_k + b_k \tag{2.7}$$

ω_k is uncorrelated wide-band noise with zero mean and variance σ^2_ω

b_k is a 1^{st}-order Gauss-Markov process with time constant, τ and variance σ^2_b

The model above assumes that both processes are zero-mean and no correlation exists between the white noise process and the Gauss-Markov process; they are independent. The model consists of three parameters which allow for three degrees of freedom

in describing the sensor behavior of any given accelerometer or rate-gyro. The following section introduces methodologies used in determining the best set of parameters from experimental data of a given inertial sensor.

2.4 Stochastic Identification Techniques

Several techniques exist to process experimental sensor data and determine the various types of error sources present. Given that the raw sensor output is modeled by Equation (2.7), such identification techniques allow the extraction of the stochastic model parameters σ_ω, σ_b^2, and τ. Of the array of stochastic modeling techniques, the Allan variance technique has become widely popular in the inertial navigation community due to its intuitive implementation, straightforward interpretation, and in most cases unique indication of various stochastic disturbances [20]. This section shows its use as a comprehensive means to determine approximate parameters to describe a given inertial sensor. Following the Allan variance technique, the experimental autocorrelation method is presented. Supplemental to the Allan variance, the autocorrelation method is used for specific identification of the parameters associated with the Gauss-Markov process, σ_b^2, and τ.

2.4.1 The Allan Variance

The Allan variance technique was introduced by David Allan in the 1960s to characterize the frequency stability of high-precision atomic clocks [21]. The Allan variance technique is sometimes analogized to the time domain version of the Fourier transform as it provides a measure of the dominance of a stochastic process over various ranges of time. The technique computes the variance of arrangements of successive averages of a

time set of data which indicates the contribution or dominance of various error sources as a function of averaging time. Inspection of plots of the Allan variance versus averaging time indicate the presence of specific stochastic processes present on a measurement. The square root of the Allan variance (root Allan variance) for many common stochastic processes appear as straight lines on a log-log scale. As a result, simple visual inspection of the root Allan variance provides immediate information about a sensor's overall stochastic behavior.

The precise definition of the Allan variance is repeated below as adapted from [9]. Given a set of N inertial measurements, Ω, sampled at a rate of f_s Hz, define a vector of averaging times, T, ranging from T_0 seconds to up to half the total time length of the data set ($\frac{N}{2f_s}$) as shown in Equation (2.8).

$$T = \begin{bmatrix} T_0 & T_0 + f_s & T_0 + 2f_s & \dots & \frac{N}{2f_s} \end{bmatrix} \tag{2.8}$$

For each averaging time, T, define $K = N/M$ clusters where M is the number of samples per cluster ($M = Tf_s$). Compute cluster averages with Equation (2.9) where k is the time index of the raw data.

$$\bar{\Omega}(T) = \frac{1}{M} \sum_{i=1}^{M} \Omega_{(k-1)M+i}, \qquad k = 1, ..., K \tag{2.9}$$

The Allan variance is then computed using Equation (2.10), with an approximation to the true ensemble average [22].

$$\sigma^2{}_{AV}(T) = \frac{1}{2(K-1)} \sum_{k=1}^{K-1} \left[\bar{\Omega}_{k+1}(M) - \bar{\Omega}_k(M)\right]^2 \tag{2.10}$$

The Allan variance can be expressed as a simple sum of the Allan variance contributions of each of the dominant processes. For example, the Allan variance as a function the contribution of process 1, 2, 3 and so on is expressed as

$$\sigma_{AV}^2 = \sigma_{p1}^2 + \sigma_{p2}^2 + \sigma_{p3}^2 + ... \tag{2.11}$$

Well-known analytical expressions of the power spectral density (PSD) of common stochastic processes have been related to analytical expressions for the Allan variance [9, 22]. The result of this relationship has yielded Allan variance equations for each noise process in terms of its processes parameters and the *averaging time*, T. The component Allan variances can be summed using Equation (2.11) to yield the total Allan variance curve as a function of averaging time. A full description of the method used to compute the Allan variance from experimental data can be found in [20].

The inertial sensor model introduced in Section 1.3 is the sum of the two stochastic processes: wide-band noise and exponentially correlated noise (Gauss-Markov). The wide-band noise is quantified by the "random walk" parameter, σ_{rw}, which is the standard-deviation of the process normalized to the square-root of the sampling frequency, f_s in Hertz. The Allan variance expression for wide-band noise is thus given by Equation (2.12).

$$\sigma_{rw}^2(T) = \left(\frac{\sigma_w}{\sqrt{f_s}}\right)^2 \tag{2.12}$$

The Allan variance expression for a first-order Markov process is given in terms of its time constant, τ, and driving noise variance, ${\sigma^2}_{\omega_b}$, as shown in Equation (2.13).

$$\sigma^2_{bias}(T) = \frac{\left(\sigma_{\omega_b}\tau\right)^2}{T}\left[1 - \frac{\tau}{2T}\left(3 - 4\exp^{\frac{-T}{\tau}} + \exp^{\frac{-2T}{\tau}}\right)\right] \tag{2.13}$$

The resulting analytical expression for the Allan variance of a static sensor sensor output with a stochastic model as in Equation (2.7) is given as the sum of equations (2.12) and (2.13) as shown in equation (2.14).

$$\sigma^2_{AV}(T) = \sigma^2_{rw}T + \frac{\left(\sigma_{\omega_b}\tau\right)^2}{T}\left[1 - \frac{\tau}{2T}\left(3 - 4\exp^{\frac{-T}{\tau}} + \exp^{\frac{-2T}{\tau}}\right)\right] \tag{2.14}$$

The root Allan variance as is most commonly plotted is simply the square root of the summed quantities in Equation (2.11). Figure 2.3 shows a sample root Allan variance plot as computed from a simulated sensor output with specifications as labeled.

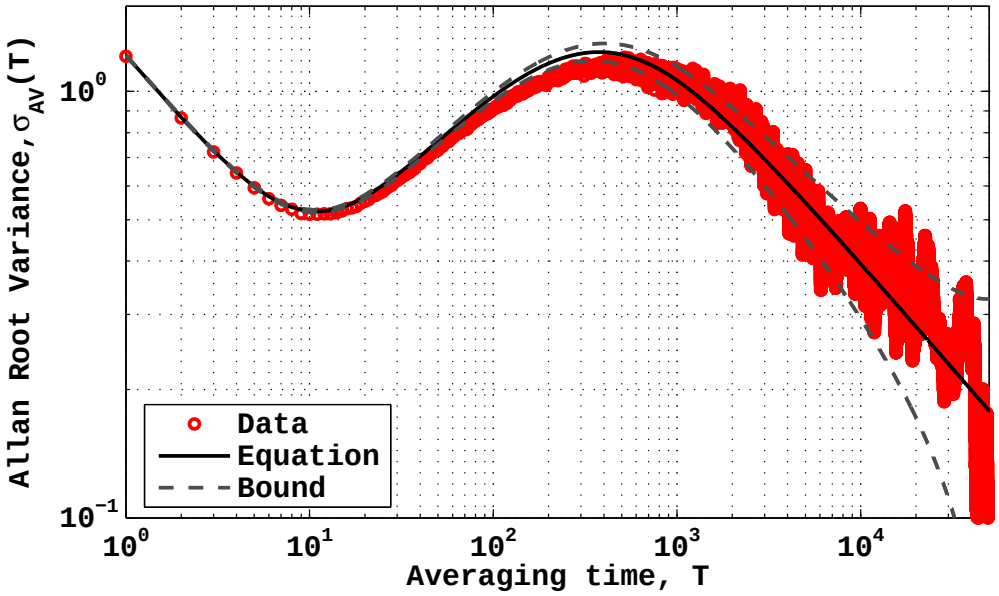

Figure 2.3: Allan Variance of Simulated Data 5 Hz ${\sigma^2}_{rw} = 1.2$, ${\sigma^2}_b = 4$, $\tau = 300$

The analytical expressions shown above have been used by others to curve-fit experimental Allan variance data for the purpose of extracting the underlying stochastic process parameters and thus characterizing the process. [9, 22, 13]. For example, the random walk parameter is straightforward to extract as it is simply the value of the Allan variance at the averaging time equal to one second. However, since the expression for the Markov process in Equation (2.13) is a non-linear function of the process parameters, estimation becomes difficult and employment of manual methods may be necessary to provide an estimate of the process magnitude and time constant.

One such problem in practical utilization of the Allan variance for sensor characterization is that its accuracy is limited by the time-length of the experimental data set. The range of averaging time is computed for half the range of experimental data. Additionally, the number of segments of averaged data for which the variance is computed

become smaller as the averaging time increases and thus yields statistically less significant values. As a result, the bounds on the accuracy of the Allan variance increase with averaging time at rates dependent upon the total length of the experimental data set. This behavior can been seen in the sample Allan variance in Figure 2.3. Such bounds are discussed further in [9]. Due to this requirement, accurate Allan variance identification of an inertial sensor exhibiting slow drift characteristics requires a sample data set of length many times greater the time constant of the particular drift of interest. For many inertial measurements, the times required for reasonable accuracy can be on the order of several days. Additionally, the time constant for the sensor is simply unknown since it is to be identified. Some rules of thumb are suggested for the length and required sample frequency of the sensor data set to ensure accurate Allan variance identification for time-varying processes in [20].

2.4.2 Experimental Autocorrelation

The Allan variance technique, while sufficient to extract the parameter associated with the white noise process, remains a difficult method for the bias drift characterization. As the Gauss-Markov process in steady-state has an autocorrelation in the form of Equation (2.6), the bias time constant, τ, and magnitude of drift, σ_b, can be extracted from the experimental autocorrelation. However, since the sensor is modeled as the sum of the two processes, successful identification of the Markov process requires its isolation. Approximate isolation can be performed by low-pass filtering the raw sensor output. The filtering removes the higher-frequencies for which the output is uncorrelated while leaving the correlated low-frequency data of interest. However, despite the attenuation of the

higher frequencies of the wide-band noise process, its lower-frequencies still exist as additive noise on the drifting bias, increasing the difficulty of identification. Furthermore, appropriate selection of the isolating filter cut-off frequency requires some knowledge of the approximate time constant of the drift process. As it is the time constant that is to be identified, the autocorrelation technique is an approximate and iterative process.

Equation (2.6) gives the characteristic autocorrelation function of the Gauss-Markov process, which is a simple exponential decay with an initial magnitude of σ_b^2 and time constant, τ. Figure 2.4 shows a sample autocorrelation plot of a simulated Markov process and its analytical curve. As is shown by the dotted lines on the plot, the time constant is found by reading the time-shift for which the autocorrelation value decays to $\frac{1}{e}$ of its initial magnitude. The initial magnitude of the Gauss-Markov process is simply the y-intercept, or variance of the filtered process.

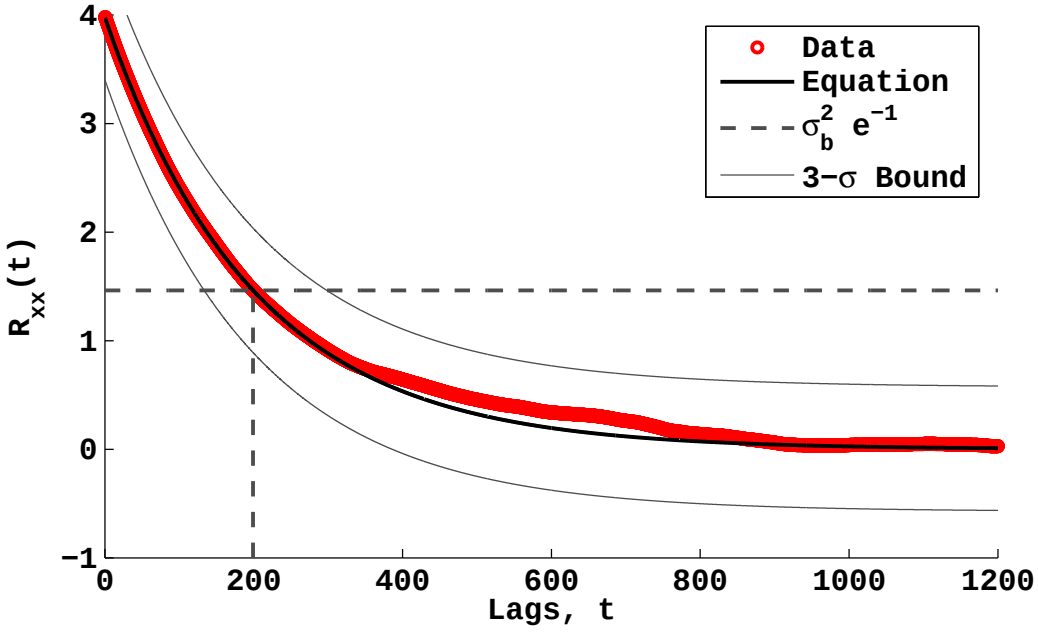

Figure 2.4: Sample Autocorrelation: 1.7x10^5 time units, $f_s = 5$ Hz, $\sigma^2{}_b = 4$, $\tau = 200$sec

Unfortunately, the experimental autocorrelation shares the same practical drawback with the Allan variance: the accuracy of the autocorrelation is dependent upon the length of the dataset. In general, the data set must be a length sufficiently longer than the time constant of interest. Experiments performed by the author in an attempt to extract reasonable parameters from raw gyro and accelerometer data proved very difficult as long data sets often carried un-modeled disturbances (such as temperature effects, long initial settling time). For a stochastic model with an autocorrelation in the form of Equation 2.6, the upper bound of the variance of the empirically-derived autocorrelation, R_{bbexp} at any lag-value can be expressed by Equation (2.15) [23].

$$\mathrm{VAR}[R_{bbexp}] <= \frac{2{\sigma^4}_b\tau}{T_d} \tag{2.15}$$

Where, ${\sigma^2}_b$ is the variance, τ is the time-constant, and T_d is the time-length of the experimental data set.

The bounds plotted in Figure 2.4 show the large uncertainty in the Gauss-Markov process experimental autocorrelation for a data set of length much longer than its time constant. For the specific sample of data generated in the figure, the time length of data set was more than 150 times the time constant.

2.4.3 Implementation Issues

As discussed for both methods, accurate identification of the process for the slowly-varying stochastic behavior of inertial sensors requires a data set many times longer than the time constant of the process. For many inertial sensors the bias drift is a slow process

(large time constant) yet still contributes significantly to the output. Effective identification for such a process requires a very long data set, sometimes outside the range of logging capabilities or a feasible window of time. Additionally, since the sensor parameters are unknown, the required length of the data set is therefore unknown and several iterations may be necessary. Additionally, the approximate Gaussian models presented may not provide a sufficient characterization of their observed behavior, especially for lower grade sensors. The identifier of these irregular sensors must then resort to highly conservative parameter estimates which simply give rough values comparable to that supplied by the sensor's manufacturer. Discussion on the supplied sensor specifications and the need for accurate identification follows in the next section.

2.5 Experimental Quantification and Identification

2.5.1 Manufacturer Sensor Specifications

Sensor specification sheets give a simple overview of a sensor's operating characteristics including measurement range, input power consumption, data format, as well as expected accuracy. The accuracy of the sensor, as it is limited by the magnitude of the stochastic processes on the output, is quantified in varying detail across the broad spectrum of sensors and their listed specifications. The specifications often indicate parameters which coarsely bound the expected accuracy based on two assumed stochastic characteristics: noise and bias. The noise is quantified by the random walk parameter as introduced in the Allan variance identification section. The random walk parameter,σ_{rw} is defined by Equation (2.12). Its units are usually given in two forms shown in Equation

(2.16).

$$\begin{aligned} \sigma_{rw} &= \frac{[\text{output units}]}{\sqrt{\text{Hz}}} \\ \sigma_{rw} &= \frac{\int [\text{output units}] dt}{\sqrt{\text{Hr}}} \end{aligned} \tag{2.16}$$

The random walk parameter is easily extracted from experimental Allan variance data as shown in the previous section.

A wider array of specifications are listed to quantify the bias drift. As a minimum, sensor manufacturers publish a conservative maximum value or maximum standard deviation within which the properly calibrated sensor is expected to output. Others give bias drift quantification in terms of a value ascertained from the Allan variance chart. Reference [24] indicates that the *bias variation* or *bias instability* parameter listed in some sheets is the lowest point on the Allan variance chart. In addition to the magnitude of the bias drift, some manufacturers of higher grade devices include some indication of the speed at which this bias drifts from the mean value by a *correlation time*. In any case, inertial sensor manufacturers provide very little information in support of full stochastic characterization of the outputs.

2.5.2 Experimental Approach

Upon review of the available literature, manufacturers provide only conservative bounds on a sensor's stochastic characteristics. This information gives only a rough starting point for the accurate characterization of this research. This section presents the basic methodology by which sufficient identification can be performed. A general methodology can be roughly outlined by the following steps:

1. Examine available specifications by manufacture
2. Determine required sampling frequency and duration of data set based on specs
3. Acquire completely static data set (on level surface)
4. Remove constant bias (subtract the mean)
5. Run the Allan variance of the data set, extract the wide-band noise magnitude
6. Filter(zero-phase filter) the data to reveal the underlying moving bias
7. Process the filtered data in the autocorrelation and extract time constant

The success of experimental identification is often difficult in practice due to many of the reasons discussed in the preceding sections. The main difficulties are that the sensor drift model is only an approximation, the approximate model parameters are unknown, and the bias can not be fully isolated. As a result, the general methodology remains a long and highly iterative process. The general process of stochastic sensor error parameter identification is demonstrated in Appendix A following the chapters of this thesis. The appendix presents the use of the techniques of this chapter to identify the stochastic model parameters with experimental data from an automotive-grade IMU.

2.6 Conclusion

In this chapter, a simple inertial sensor error model that provides an approximation to the stochastic behavior observed on a a wide-range of inertial sensors grades and types has been presented. The model consists of the sum of two stationary, Gaussian random processes which describe the short-term and long-term stochastic behavior of static inertial sensor outputs. The techniques of Allan variance and autocorrelation were presented

as means to identify the three parameters required to describe the assumed model form from experimental sensor data. The experimental procedure was then outlined and difficulties of the method presented. In the following chapters, each of the error processes as detailed in this chapter are used for the purpose of quantifying the error in position, velocity, and attitude when dead-reckoning with an IMU in various kinematic scenarios.

Chapter 3

Covariance Propagation of Stochastic Errors

3.1 Introduction

Bounded accuracy in inertial navigation depends upon regular position, velocity, and attitude measurements to compensate for the error growth of the integrated IMU signals. Many navigation methods employ regular measurements from GPS sensors, vision, odometry, and other sources of velocity, position, and attitude data. These measurements are often fused together in a navigation Kalman filter resulting in an optimal estimate of the vehicle's state. As GPS requires an unobstructed line-of-sight to at least four satellites, it fails to provide accurate data when traveling under bridges, heavily wooded areas, and in downtown city streets where tall buildings bound the path of the receiver. Under such conditions when the GPS data becomes unavailable, the Kalman filter reduces to a simple algorithm in which the navigation states are derived solely from the integrated outputs of the inertial sensors initialized to the last "best estimate". As all inertial sensors are inherently corrupted with stochastic type errors (as introduced in Chapter 2), the integration of these signals cause the uncertainty in the resulting navigation states to increase with each step in time. As a result, the error in the estimated position, velocity, and attitude states grow with time. It is the goal of this chapter to quantify the the error growth due to the integrated stochastic errors present on the inertial measurements.

By using the stochastic models from Chapter 2, this quantification is achieved by deriving expressions for the variance of the integrated sensor errors using a technique

modeled after [11]. The variance expressions are then validated using a Monte Carlo simulation. For a single-axis sensor, the variance describes the error expected when dead-reckoning in one degree of freedom motion. The chapter concludes with a sensitivity analysis illustrating the influence of the stochastic model parameters on the variance of the integrated sensor.

3.2 Simplified Navigation Scenario: Single Axis

The motion of a navigating body in the inertial or navigation frame can be derived from body-fixed inertial measurements of acceleration, a, and rotation rate, g. To attain the vehicle states of velocity, orientation, and position in the navigation frame in the general sense, the body-frame measurements are transformed using nonlinear differential equation relationships (shown later in Chapter 5). As a building block in providing an analysis of the general navigation scenario, preliminary attention is first turned to a simple one degree-of-freedom (1-DOF) motion scenario in which a single axis gyro or single axis accelerometer is integrated to provide the navigation frame states in its component direction. Equations (3.1-3.3) show the single-axis vehicle states of orientation, velocity, and position (ψ, V, P) as derived from the integrations of the corresponding inertial measurements.

$$\psi = \int g\, dt \tag{3.1}$$

$$V = \int a\, dt \tag{3.2}$$

$$P = \int V\, dt \tag{3.3}$$

It is the task of the following sections to quantify the error resulting from the use of Equations (3.1-3.3) with inertial sensors modeled as shown in Chapter 2.

3.3 General Characterization of Raw Sensor Measurement

Recall the simple sensor model from Chapter 2 as described by Equation (2.1)

$$y_{meas} = (SF)\, y + \epsilon + b$$

As stochastic terms are assumed zero-mean, the mean value of the sensor output is simply the deterministic terms.

$$\begin{aligned} \mathrm{E}[y_{meas}(t)] &= \mathrm{E}[(SF)\, y(t)] + \mathrm{E}[\epsilon(t)] + \mathrm{E}[b] \\ &= (SF)\, y(t) + b \end{aligned} \tag{3.4}$$

The variance of the sensor output is equal to the variance of the stochastic error.

$$\begin{aligned} \mathrm{VAR}[y_{meas}] &= \mathrm{E}[y_{meas}^2(t)] - \mathrm{E}[y_{meas}(t)]^2 \\ &= \mathrm{E}[((SF)\, y + \epsilon(t) + b)\,((SF)\, y(t) + \epsilon(t) + b)] - ((SF)\, y(t) + \epsilon(t) + b)^2 \\ {\sigma_{y_{meas}}}^2(t) &= {\sigma_\epsilon}^2(t) \end{aligned} \tag{3.5}$$

Since the error sources are Gaussian and uncorrelated, the variance in the sensor output can be expressed as the sum of the variances of the two contributing error sources: wide band noise, ω, and Gauss-Markov process, b, as introduced in Chapter 2.

$${\sigma_\epsilon}^2(t) = {\sigma_\omega}^2(t) + {\sigma_b}^2(t) \tag{3.6}$$

3.4 Characterization of Integrated Sensor Measurement

Given a sensor modeled with Equation (2.1) and whose stochastic errors are characterized as the sum of the independent noise sources introduced in Chapter 2, the purely integrated sensor is characterized as follows. The mean of the integrated sensor is simply the value of the integrated deterministic terms.

$$\begin{aligned} \mathrm{E}[\int y_{meas}(t)\,dt] &= \mathrm{E}\left[\int [(SF)\,y(t)+b]\,dt\right] + \mathrm{E}\left[\int \epsilon(t)\,dt\right] \\ &= \int [(SF)\,y(t)+b]\,dt + 0 \\ &= SF\int y(t)\,dt + bt \end{aligned} \tag{3.7}$$

The variance of the integrated sensor output is the variance of the integrated independent stochastic error sources.

$$\begin{aligned} \mathrm{E}[\int y_{meas}^2(t)\,dt] &= \mathrm{E}[\left(\int (SF)\,y + \epsilon(t) + bdt\right)\left(\int (SF)\,y(t) + \epsilon(t) + bdt\right)] \\ &\quad -\left(\int (SF)\,y(t) + \epsilon(t) + bdt\right)^2 \\ &= \int \mathrm{E}[\epsilon^2(t)]\,dt \end{aligned} \tag{3.8}$$

The variance of the integrated sensor output is equal to the sum of the variances of the independent integrated error sources.

$$\sigma_{\int y_{meas}}{}^2(k) = \sigma_{\int \omega}{}^2(k) + \sigma_{\int b}{}^2(k) \tag{3.9}$$

Applying the same methods to the double integrated case yields.

$$\begin{aligned} \mathrm{E}[\iint y_{meas}(t)\,dt] &= \mathrm{E}\left[\iint [(SF)\,y(t)+b]\,dt^2\right] + \mathrm{E}\left[\iint \epsilon(t)\,dt^2\right] \\ &= \iint [(SF)\,y(t)+b]\,dt^2 + 0 \\ &= SF\iint y(t)\,dt^2 + bt^2 \end{aligned} \tag{3.10}$$

Performing analogous operations yields the resulting variance for the double-integrated sensor output.

$$\sigma_{\iint y_{meas}}{}^2(k) = \sigma_{\iint \omega}{}^2(k) + \sigma_{\iint b}{}^2(k) \tag{3.11}$$

As shown in Equations (3.9) and (3.11), the variance in the integrated sensor output is equal to the sum of the variances of the integrated stochastic error sources. In the following sections the expressions of the individual variance functions of the random error processes and their integrals are derived.

3.5 Single Axis Stochastic Error Contributions

Assuming that the numerical integration of the sensor is performed using an Euler approximation, the resulting integral values are simply scaled sums of the inertial values. As the scaled sum is a linear operation and the stochastic processes are Gaussian, the integrated stochastic processes are also Gaussian with transformed mean and variance functions. The following sections in this chapter derive the variance functions of the integrated and double-integrated wide-band noise and Gauss-Markov processes for numerical integration using the Euler method. The straightforward time-domain technique

modeled after [11] is employed here for derivations with the error models presented in Chapter 2.

3.5.1 Variance of Integrated Wide Band noise

A derivation of the variance of integrated wide-band noise using the technique as follows has been shown in [11]. It is repeated here as an instructive example of the methodology by which the proceeding expressions are derived.

Let $\ddot{y}$ represent a wide-band noise process with variance ${\sigma^2}_{\omega}$.

$$\ddot{y} = \omega \tag{3.12}$$

Integrating the $\ddot{y}$ yields its integral value.

$$\dot{y} = \int \omega \, dt \tag{3.13}$$

The above integration can be approximated by Euler's method (left hand sum) with the initial condition $\dot{y}_0 = 0$.

$$\begin{aligned} \dot{y}_k &= \dot{y}_{k-1} + \Delta t \omega_{k-1} \\ &= \dot{y}_0 + \Delta t \sum_{i=0}^{k-1} \omega_i \end{aligned} \tag{3.14}$$

Square both sides to obtain

$$\begin{aligned} \dot{y}_k \dot{y}_k &= \left(\Delta t \sum_{i=0}^{k-1} \omega_i \right) \left(\Delta t \sum_{i=0}^{k-1} \omega_i \right) \\ \dot{y}_k \dot{y}_k &= \Delta t^2 \left(\sum_{i=0}^{k-1} \omega_i \right) \left(\sum_{i=0}^{k-1} \omega_i \right) \end{aligned} \tag{3.15}$$

Take the expected value of the squared expression.

$$\mathrm{E}\left[\dot{y}_k \dot{y}_k \right] = \mathrm{E}\left[\Delta t^2 \left(\sum_{i=0}^{k-1} \omega_i \right) \left(\sum_{i=0}^{k-1} \omega_i \right) \right] \tag{3.16}$$

The expectation of all of cross-terms of ω_i are equal to zero, as successive ω values in time are completely uncorrelated. The expression therefore reduces to

$$\begin{aligned} \mathrm{E}\left[\dot{y}_k \dot{y}_k \right] &= \Delta t^2 \mathrm{E}\left[\sum_{i=0}^{k-1} \omega_i^2 \right] \\ &= \Delta t^2 \sum_{i=0}^{k-1} \mathrm{E}\left[\omega_i \omega_i \right] \end{aligned} \tag{3.17}$$

The final result is an expression for the variance of integrated wide-band noise as a function of the variance of the wide-band noise, time index, and sampling interval.

$$\sigma_{\dot{y}}^2 = \sigma_{\omega}^2 \Delta t^2 k \tag{3.18}$$

3.5.2 Variance of Double Integrated Wide Band noise

Double integrating the wide-band noise process, $\ddot{y}$, to yield its double-integral value is shown below

$$y = \int \dot{y}\, dt = \iint \omega\, dt^2 \tag{3.19}$$

Approximating the double-integration by Euler's method (left hand sum), the following substitution is made

$$\begin{aligned} y_k &= y_{k-1} + \Delta t \dot{y}_{k-1} \\ &= y_0 + \Delta t^2 \sum_{j=0}^{k-1} \left(\sum_{i=0}^{j-1} \omega_i \right) \end{aligned} \tag{3.20}$$

Simplification of the double summation yields a single summation with an indexed coefficient.

$$y_k = \Delta t^2 \sum_{j=0}^{k-1} (k - j - 1)\, \omega_j \tag{3.21}$$

Squaring both sides gives

$$y_k y_k = \Delta t^4 \left(\sum_{j=0}^{k-1} (k - j - 1)\, \omega_j \right) \left(\sum_{j=0}^{k-1} (k - j - 1)\, \omega_j \right) \tag{3.22}$$

Taking the expected value of both sides with knowledge that successive values of ω_j are uncorrelated results in

$$\mathrm{E}\left[y_k y_k\right] = \Delta t^4 \sum_{j=0}^{k-1} (k - j - 1)^2 \mathrm{E}\left[\omega_j \omega_j\right] \tag{3.23}$$

Expansion of the summation leads to

$$\mathrm{E}\left[y_k y_k\right] = \Delta t^4 \left((k-1)^2 \sum_{j=0}^{k-1}(1) - 2(k-1)\sum_{j=0}^{k-1} j + \sum_{j=0}^{k-1} j^2 \right) \mathrm{E}\left[\omega_j \omega_j\right] \tag{3.24}$$

Using the analytic solutions for power series summations the expression reduces to

$$\mathrm{E}\left[y_k y_k\right] = \Delta t^4 \left(k(k-1)^2 - 2(k-1)\frac{1}{2}k(k+1) + \frac{1}{6}k(k+1)(2k+1) \right) \mathrm{E}\left[\omega_j \omega_j\right] \tag{3.25}$$

Further simplification yields an expression for the variance of double integrated wide-band noise as a function of its variance, time index, and sampling interval.

$${\sigma_y}^2 = \Delta t^4 {\sigma_\omega}^2 \left(\frac{1}{3}k^3 + \frac{1}{2}k^2 + \frac{1}{6}k \right) \tag{3.26}$$

3.5.3 Variance of 1st order Gauss-Markov process

The differential equation for the 1st order Gauss-Markov process as given in Equation (2.4) can be realized using an Euler approximation

$$\begin{aligned} b_k &= b_{k-1} + \Delta t \dot{b}_{k-1} \\ &= b_{k-1} + \Delta t \frac{-b_{k-1}}{\tau} + \Delta t \omega_{b_{k-1}} \\ &= \left(1 - \frac{\Delta t}{\tau}\right) b_{k-1} + \Delta t \omega_{b_{k-1}} \end{aligned} \tag{3.27}$$

For clarity in derivation, define $A = \left(1 - \frac{\Delta t}{\tau}\right)$ to get

$$b_k = A b_{k-1} + \Delta t \omega_{k-1} \tag{3.28}$$

The expression can be written as the following summation where the initial condition of the process is assumed to be zero, $b_0 = 0$.

$$\begin{aligned} b_k &= A^{k-1}b_0 + \Delta t \sum_{i=0}^{k-1} A^{k-i-1}\omega_{b_i} \\ b_k &= \Delta t \sum_{i=0}^{k-1} A^{k-i-1}\omega_{b_i} \end{aligned} \tag{3.29}$$

While this zero initial condition assumption simplifies the analysis below, the resulting process may take time to settle into steady state depending on the size of the time constant. As this stochastic process is only an approximation to the observed sensor phenomenon, the significance of the initial condition is uncertain.

Squaring both sides obtains

$$b_k b_k = \left(\Delta t \sum_{i=0}^{k-1} A^{k-i-1}\omega_{b_i} \right) \left(\Delta t \sum_{i=0}^{k-1} A^{k-i-1}\omega_{b_i} \right) \tag{3.30}$$

Applying the expectation operator to both sides with the knowledge that successive ω_{b_i} values in time are completely uncorrelated and exhibit an identical variance results in

$$\begin{aligned} \mathrm{E}\left[b_k b_k\right] &= \Delta t^2 \sum_{i=0}^{k-1} A^{2(k-i-1)} \mathrm{E}\left[\omega_{b_i}\omega_{b_i}\right] \\ &= \Delta t^2 A^{2k-2} \sum_{i=0}^{k-1} A^{-2i} \mathrm{E}\left[\omega_{b_i}\omega_{b_i}\right] \\ &= \Delta t^2 A^{2k-2} \sum_{i=0}^{k-1} A^{-2i} {\sigma^2}_{\omega_b} \end{aligned} \tag{3.31}$$

Using the solution to the geometric series yields the following analytical expression

$$\mathrm{E}\left[b_k b_k\right] = \Delta t^2 A^{2k-2} \left(\frac{1 - A^{-2k}}{1 - A^{-2}}\right) {\sigma^2}_{\omega_b} \tag{3.32}$$

Further simplification results in the following expression for the variance of a 1st order Gauss-Markov process as a function of the variance of the driving noise, ${\sigma^2}_{\omega_b}$, time index, k, and sampling interval, Δt.

$${\sigma^2}_b = \Delta t^2 {\sigma^2}_{\omega_b} \left(\frac{A^{2k} - 1}{A^2 - 1}\right) \tag{3.33}$$

Note that for positive values of τ, A is less than one and therefore ${\sigma^2}_b$ will reach a steady-state value.

3.5.4 Variance of Integrated 1st order Gauss-Markov process

Let $\ddot{x}$ represent the bias drift as modeled by the Gauss-Markov process. Assume the process is realized by an Euler integration with zero initial condition as in Equation (3.27).

$$\ddot{x}_k = b_k = A b_{k-1} + \Delta t \omega_{b_{k-1}} \tag{3.34}$$

Next, approximate the integral using Euler's method with initial condition $\dot{x}_0 = 0$

$$\begin{aligned}
\dot{x} &= \int \ddot{x}\, dt = \int b\, dt \\
&= \dot{x}_{k-1} + \Delta t \ddot{x}_{k-1} \\
&= \dot{x}_0 + \Delta t\big(A\ddot{x}_{k-2} + \Delta t \omega_{b_{k-2}}\big) \\
&= \Delta t^2 \sum_{j=0}^{k-1} \left(\sum_{i=0}^{j-1} A^{j-i-1} \omega_{b_i} \right)
\end{aligned} \tag{3.35}$$

The summation can be rewritten as

$$\dot{x}_k = \Delta t^2 \sum_{j=0}^{k-2} \left(\sum_{i=0}^{j} A^j A^{-i} \omega_{b_i} \right) \tag{3.36}$$

Expand the summation for $k = 5$ and collect the ω_{b_i} terms

$$\begin{aligned}
\dot{x}_5 &= \Delta t^2 \sum_{j=0}^{4} \left(\sum_{i=0}^{j-1} A^{j-i-1} \omega_{b_i} \right) \qquad (3.37) \\
&= \Delta t^2 \left(\omega_{b0} + A\omega_{b0} + \omega_{b1} + A^2\omega_{b0} + A\omega_{b1} + \omega_{b2} + A^3\omega_{b0} + A^2\omega_{b1} + A\omega_{b2} + \omega_{b3} \right) \\
&= \Delta t^2 \left[\omega_{b0} \left(A^0 + A^1 + A^2 + A^3 \right) + \omega_{b1} \left(A^0 + A^1 + A^2 \right) + \omega_{b2} \left(A^0 + A^1 \right) + \omega_{b3} \left(A^0 \right) \right]
\end{aligned}$$

Investigation of the expansion and rearrangement of Equation (3.36) results in simplification to the double summation

$$\dot{x}_k = \Delta t^2 \sum_{i=0}^{k-2} \omega_{b_i} \left(\sum_{j=0}^{k-1-i} A^j \right) \tag{3.38}$$

Using the solution of the geometric series, the expression is further reduced to a single summation

$$\begin{aligned} \dot{x}_k &= \Delta t^2 \sum_{i=0}^{k-2} \left(\frac{1 - A^{k-1-i}}{1 - A} \right) \omega_{b_i} \\ &= \frac{\Delta t^2}{1 - A} \sum_{i=0}^{k-2} \left(1 - A^{k-1-i} \right) \omega_{b_i} \end{aligned} \tag{3.39}$$

Then both sides are squared to obtain

$$\dot{x}_k = \frac{\Delta t^4}{(1 - A)^2} \left(\sum_{i=0}^{k-2} \left(1 - A^{k-1-i} \right) \omega_{b_i} \right) \left(\sum_{i=0}^{k-2} \left(1 - A^{k-1-i} \right) \omega_{b_i} \right) \tag{3.40}$$

Taking the expected value of both sides with knowledge that successive ω_{b_i} values in time are completely uncorrelated results in

$$\begin{aligned} \mathrm{E}\left[\dot{x}_k \dot{x}_k \right] &= \frac{\Delta t^4}{(1 - A)^2} \sum_{i=0}^{k-2} \left(1 - A^{k-1-i} \right)^2 \mathrm{E}\left[\omega_{b_i} \omega_{b_i} \right] \\ &= \frac{\Delta t^4}{(1 - A)^2} \sum_{i=0}^{k-2} \left(1 - \frac{2A^k}{AA^i} + \frac{A^{2k}}{A^2 A^{2i}} \right) \sigma_{\omega_b}^2 \\ &= \frac{\Delta t^4}{(1 - A)^2} \left(\sum_{i=0}^{k-2} (1) - \frac{2A^k}{A} \sum_{i=0}^{k-2} A^{-i} + \frac{A^{2k}}{A^2} \sum_{i=0}^{k-2} A^{-2i} \right) \sigma_{\omega_b}^2 \end{aligned} \tag{3.41}$$

Using the solutions to the geometric series to simplify the summations gives

$$\mathrm{E}\left[\dot{x}_k \dot{x}_k \right] = \frac{\Delta t^4}{(1 - A)^2} \left((k - 1) - \frac{2A^k}{A} \frac{1 - A^{1-k}}{1 - A^{-1}} + \frac{A^{2k}}{A^2} \frac{1 - A^{2-2k}}{1 - A^{-2}} \right) {\sigma_\omega}^2 \tag{3.42}$$

This results in an expression for the variance of single integrated 1st order Gauss-Markov process in terms of the variance of the driving noise, ${\sigma^2}_{\omega_b}$, time index, k, and sampling interval, Δt.

$$ {\sigma_{\dot{x}}}^2 = \Delta t^4 \sigma^2_{\omega_b} \left(\frac{1 + 2A - 2A^k - 2A^{1+k} + A^{2k} - k + kA^2}{-1 + 2A - 2A^3 + A^4} \right) \tag{3.43} $$

The above equation can be expressed in a condensed form

$$ {\sigma_{\dot{x}}}^2 = \Delta t^4 \sigma^2_{\omega_b} \left(-a_1 + a_2 A^k - a_3 A^{2k} + a_4 k \right) \tag{3.44} $$

Where the constants of Equation (3.44) are

$$ \begin{aligned} a_1 &= \frac{1 + 2A}{-1 + 2A - 2A^3 + A^4} \\ a_2 &= \frac{-2 - 2A}{-1 + 2A - 2A^3 + A^4} \\ a_3 &= \frac{1}{-1 + 2A - 2A^3 + A^4} \\ a_4 &= \frac{A^2 - 1}{-1 + 2A - 2A^3 + A^4} \end{aligned} \tag{3.45} $$

3.5.5 Variance of Double Integrated 1st order Gauss-Markov process

Let x represent the double integration of the bias drift, b

$$ x = \int \dot{x}\, dt = \iint b\, dt^2 $$

As before, Euler integration is used to realize the Markov process, $\dot{x}$, using the initial condition $x_0 = 0$. The double integration the process is represented below as a series of

nested summations

$$x_k = \Delta t^3 \sum_{m=0}^{k-1} \sum_{j=0}^{m-1} \sum_{i=0}^{j-1} A^{j-i-1} \omega_{b_i} \tag{3.46}$$

Expanding the summations for $k = 5$ and collect the ω terms results in

$$\begin{aligned} x_5 &= \Delta t^3 \sum_{m=0}^{4} \sum_{j=0}^{m-1} \sum_{i=0}^{j-1} A^{j-i-1} \omega_{b_i} \\ &= \Delta t^3 \left(A^2 \omega_{b0} + (\omega_{b1} + 2\omega_{b0}) A + \omega_{b2} + 2\omega_{b1} + 3\omega_{b0} \right) \\ &= \Delta t^3 \left(\omega_{b0} (A^2 + 2A^1 + 3A^0) + \omega_{b1} (A^1 + 2A^0) + \omega_{b2} (A^0) \right) \end{aligned} \tag{3.47}$$

Investigation of the preceding expansion leads to the simplification of the triple summation expression into two nested summations in which ω_i is removed from the innermost summation

$$\begin{aligned} x_k &= \Delta t^3 \sum_{i=0}^{k-3} \omega_{b_i} \sum_{j=0}^{k-3-i} (j+1) A^{k-3-i-j} \\ &= \Delta t^3 \sum_{i=0}^{k-3} \omega_{b_i} A^{k-3-i} \sum_{j=0}^{k-3-i} (j A^{-j} + A^{-j}) \end{aligned} \tag{3.48}$$

By substituting the following derivatives into Equation (3.48), the following expression is obtained

$$\begin{aligned} \frac{d}{dA} \left(A^{-j} \right) &= -\frac{1}{A} \left(j A^{-j} \right) \\ j A^{-j} &= -A \frac{d}{dA} \left(A^{-j} \right) \end{aligned}$$

where, the iA^{-i} term can be decoupled as shown below

$$x_k = \Delta t^3 \sum_{i=0}^{k-3} \omega_{b_i} A^{k-3-i} \left(\sum_{j=0}^{k-3-i} A^{-j} - A \frac{d}{dA} \sum_{j=0}^{k-3-i} A^{-j} \right) \tag{3.49}$$

Using the solution to the geometric series of A^{-i}, the expression becomes

$$x_k = \Delta t^3 \sum_{i=0}^{k-3} \omega_{b_i} A^{k-3-i} \left(\left(\frac{1 - A^{-k+2+i}}{1 - A^{-1}} \right) - A \frac{d}{dA} \left(\frac{1 - A^{-k+2+i}}{1 - A^{-1}} \right) \right) \tag{3.50}$$

Evaluation of the derivative allows further simplification, yielding

$$\begin{aligned} x_k &= \Delta t^3 \sum_{i=0}^{k-3} \omega_{b_i} A^{k-3-i} \left[\left(\frac{1 - A^{-k+2+i}}{1 - A^{-1}} \right) - A \left(\frac{(-k+2+i)A^{-k+2+i}}{A(1 - A^{-1})} - \frac{1 - A^{-k+2+i}}{A^2 (1 - A^{-1})^2} \right) \right] \\ &= \Delta t^3 \sum_{i=0}^{k-3} \omega_{b_i} \frac{(A^{k-1-i} + A - 2 - kA + k + iA - i)}{(A-1)^2} \end{aligned} \tag{3.51}$$

With the knowledge that successive ω_{b_i} values in time are completely uncorrelated, squaring and applying the expectation operator gives

$$\begin{aligned} \mathrm{E}[x_k x_k] &= \Delta t^6 \sum_{i=0}^{k-3} \mathrm{E}[\omega_{b_i} \omega_{b_i}] \frac{(A^{k-1-i} + A - 2 - kA + k + iA - i)^2}{(A-1)^4} \\ &= \Delta t^3 \frac{\mathrm{E}[\omega_{b_i} \omega_{b_i}]}{(A-1)^4} \sum_{i=0}^{k-3} \Big(A^{2k-2} A^{-i} + (A - 2 - kA + k)^2 + (A-1) i^2) + \\ &\qquad 2A^{k-1}(A - 2 - kA + k) A^{-i} + 2A^{k-1}(A-1) A^i i + \\ &\qquad 2(A - 2 - kA + k)(A-1) i \Big) \end{aligned} \tag{3.52}$$

A distribution of the above summation yields

$$\begin{aligned}\mathrm{E}[x_k x_k] &= \Delta t^6 \frac{\mathrm{E}[\omega_{b_i}\omega_{b_i}]}{(A-1)^4}\Bigg(A^{2k-2}\sum_{i=0}^{k-3}A^{-i} + (A-2-kA+k)^2 + (A-1)^2\sum_{i=0}^{k-3}i^2 + \\ &\quad 2A^{k-1}(A-2-kA+k)\sum_{i=0}^{k-3}A^{-i} + 2A^{k-1}(A-1)\sum_{i=0}^{k-3}iA^i + \\ &\quad 2(A-2-kA+k)(A-1)\sum_{i=0}^{k-3}i\Bigg) \qquad (3.53)\end{aligned}$$

Using the solutions to the geometric and power series allows the summations to be simplified further

$$\begin{aligned}\mathrm{E}[x_k x_k] &= \Delta t^3 \frac{\mathrm{E}[\omega_{b_i}\omega_{b_i}]}{(A-1)^4}\Bigg(A^{2k-2}\frac{1-A^{-2k+4}}{1-A^{-2}} + (A-2-kA+k)^2(k-2) + \\ &\quad (A-1)^2\frac{1}{6}(k-3)(k-2)(2k-5) + \\ &\quad 2A^{k-1}(A-2-kA+k)\frac{1-A^{-k+2}}{1-A^{-1}} + \\ &\quad 2A^{k-1}(A-1)(-A)\frac{d}{dA}\frac{1-A^{-k+2}}{1-A^{-1}} + \\ &\quad (A-2-kA+k)(A-1)(k-3)(k-2)\Bigg) \qquad (3.54)\end{aligned}$$

The final result is an expression for the variance of a double integrated Gauss-Markov process in terms of the in terms of the variance of the driving noise, ${\sigma^2}_{\omega_b}$, time index, k,

and sampling interval, Δt.

$$\begin{aligned}
{\sigma_x}^2 &= \Delta t^6 {\sigma_{\omega_b}}^2 \Big((-2 - 4A + 2A^4 + 4A^3 + 2)k^3 + \\
&\quad (9 - 12A - 6A^2 + 12A^3 - 3A^4)k^2 + \\
&\quad (-13 + 8A - 8A^3 + A^4 + 12A^k - 12A^{2+k})k + \\
&\quad (6 - 12A^2 - 12A^k + 12A^{2+k} + 6A^{2k}) \Big)
\end{aligned} \tag{3.55}$$

The above equation can also be expressed as

$$\begin{aligned}
{\sigma_x}^2 &= \Delta t^6 {\sigma_{\omega_b}}^2 \Big(c_1 k^3 + c_2 k^2 + \\
&\quad (c_3 + 12A^k - 12A^{2+k})k + \\
&\quad (c_4 - 12A^k + 12A^{2+k} + 6A^{2k}) \Big)
\end{aligned} \tag{3.56}$$

where,

$$\begin{aligned}
c_1 &= -2 - 4A + 2A^4 + 4A^3 + 2 \\
c_2 &= 9 - 12A - 6A^2 + 12A^3 - 3A^4 \\
c_3 &= -13 + 8A - 8A^3 + A^4 \\
c_4 &= 6 - 12A^2
\end{aligned}$$

3.5.6 Summary of Results

The preceding sections derived the variance expressions for the raw, integrated, and double integrated stochastic error processes of wide-band noise and exponentially-correlated noise. Tables 3.1 and 3.2 show the resulting expressions in summary. The

left-most column represents the level of integration and the right column indicates the corresponding variance functions. Recall that k is the time index and Δt is the sample interval.

Table 3.1: Variance Contributions of Wide-Band Noise Integrals

State	Variance, $\sigma^2(k)$
ω	σ_ω^2
$\int \omega \, dt$	$\sigma_\omega^2 \Delta t^2 k$
$\iint \omega \, dt^2$	$\Delta t^4 {\sigma_\omega}^2 \left(\frac{1}{3}k^3 + \frac{1}{2}k^2 + \frac{1}{6}k\right)$

Table 3.2: Variance Contributions of 1^{st}-Order Gauss-Markov Process Integrals

State	Variance, $\sigma^2(k)$
b	$\Delta t^2 {\sigma_{\omega_b}}^2 \left(\frac{A^{2k}-1}{A^2-1}\right)$
$\int b \, dt$	$\Delta t^4 \sigma_{\omega_b}^2 \left(-a_1 + a_2 A^k - a_3 A^{2k} + a_4 k\right)$
$\iint b \, dt^2$	$\Delta t^6 {\sigma_{\omega_b}}^2 \Big(c_1 k^3 + c_2 k^2 + (c_3 + 12A^k - 12A^{2+k})k + (c_4 - 12A^k + 12A^{2+k} + 6A^{2k})\Big)$

3.6 Validation of the Error Propagation

In order to validate the derived expressions for the variance functions of the integrated stochastic processes, a Monte Carlo simulation was employed. The basic idea of the simulation is to generate a large number of independent stochastic processes using fixed parameters for a given window of time and then integrate (and double integrate) each simulated process over the duration. The variance over all the simulated runs is

computed for each time step. The computed variance functions represent the variance versus time of the integral processes. The empirically deduced variances are then compared to the derived expressions in Tables 3.1 and 3.2.

The following plots show the analytical variance functions compared against the Monte Carlo results for each of the stochastic processes. In each example figure, the simulated variance matches well to the analytic expression thus validating the expressions derived in the preceding sections.

3.6.1 Propagation of Wide-Band Noise Process

Figures 3.1, 3.2, and 3.3 show the validation of standard deviation functions for a wide-band noise process, its integral, and its double integral, respectively. The plots show that the equations as derived and listed in the Tables match the variance generated in the Monte Carlo simulation.

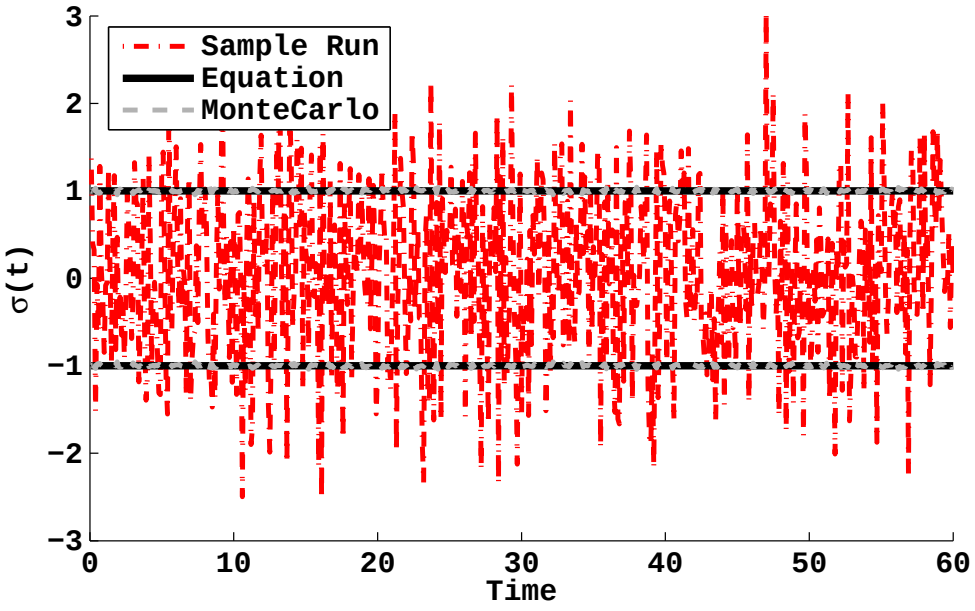

Figure 3.1: Standard Deviation of Wide-Band Noise Process: 10Hz, $\sigma_\omega = 1$, 2000 Monte Carlo iterations

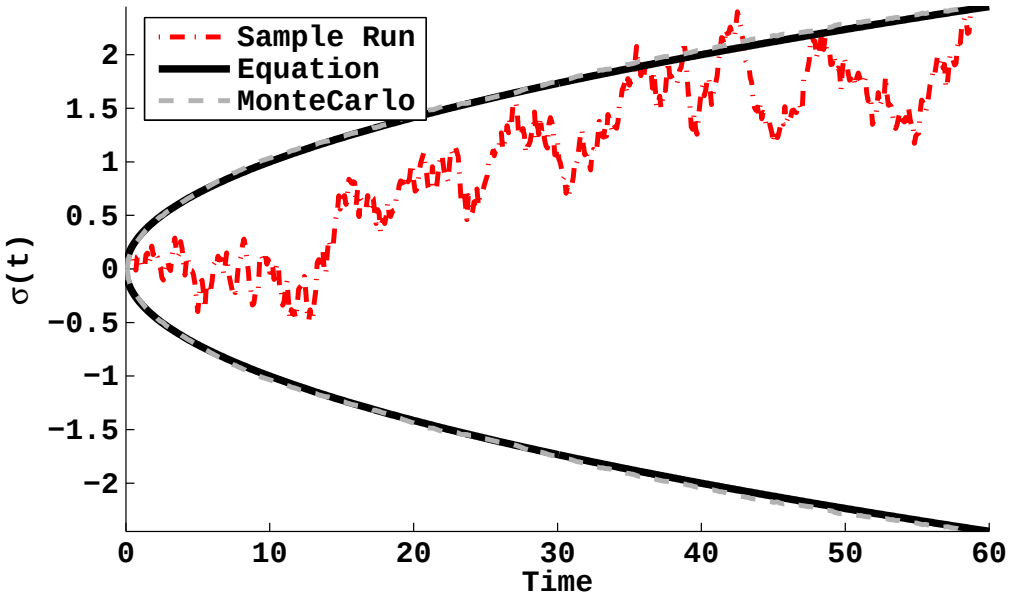

Figure 3.2: Standard Deviation of Integrated Wide-Band Noise Process: 10Hz, $\sigma_\omega = 1$, 2000 Monte Carlo iterations

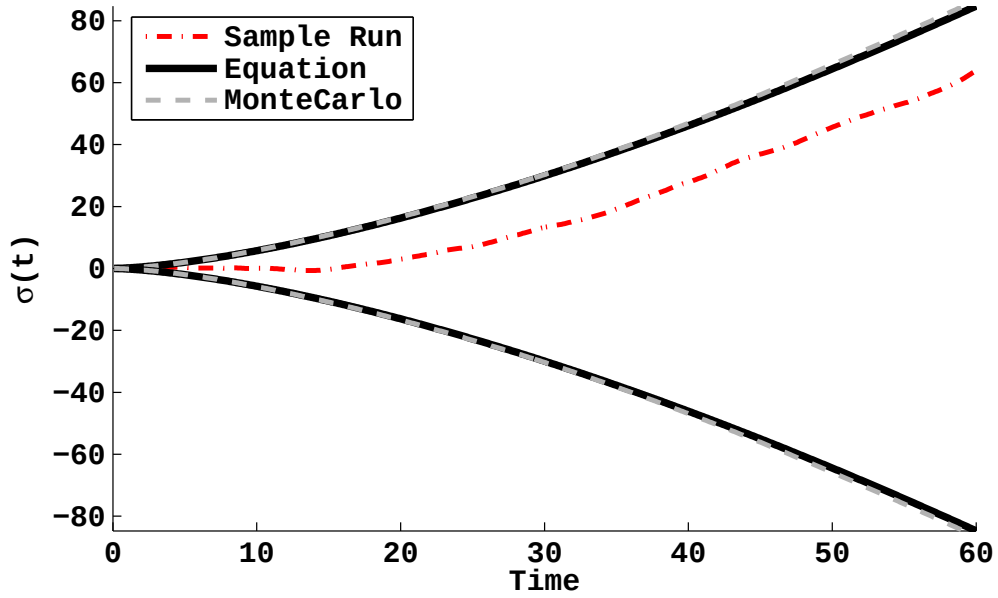

Figure 3.3: Standard Deviation of Double Integrated Wide-Band Noise Process: 10Hz, $\sigma_\omega = 1$, 2000 Monte Carlo iterations

3.6.2 Propagation of Gauss-Markov Process

Figures 3.4, 3.5, and 3.6 show the validation of standard deviation functions for a Gauss-Markov process, its integral, and its double integral. The plots show that the equations as derived and listed in the Tables match the variance achieved through the Monte Carlo simulation. Note that for the non-integrated Gauss-Markov process shown in Figure 3.4, the process variance reaches steady state as determined by Equation (3.33).

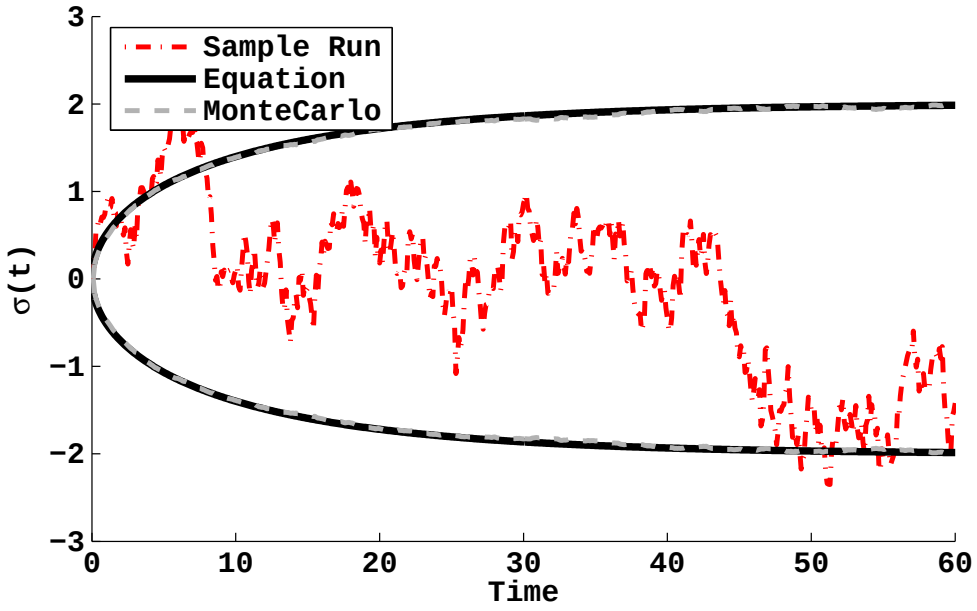

Figure 3.4: Standard Deviation of Gauss-Markov Process: 10Hz, $\sigma_b = 2$, $\tau = 30$, 2000 Monte Carlo iterations

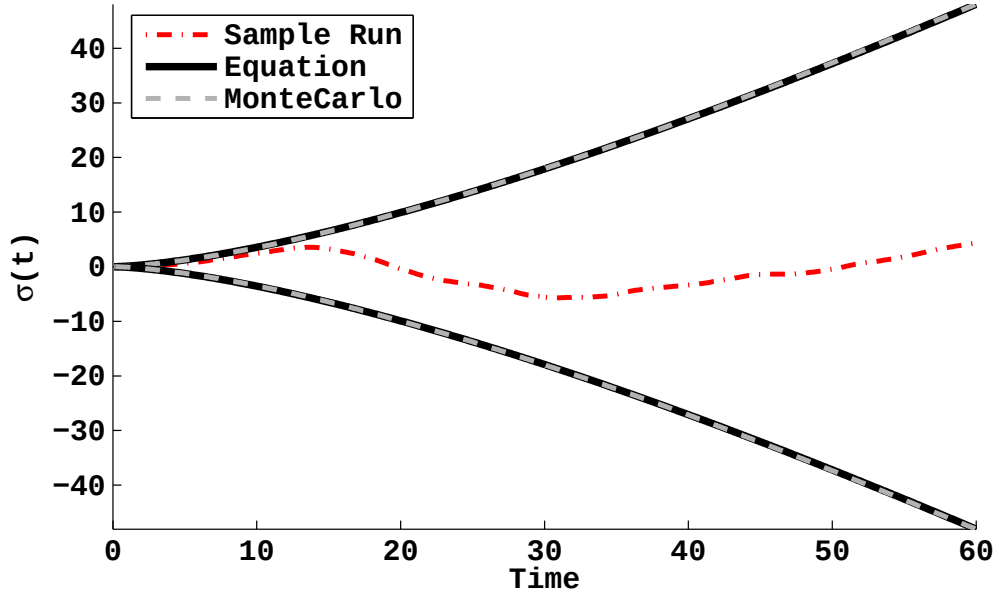

Figure 3.5: Standard Deviation of Integrated Gauss-Markov Process: 10Hz, $\sigma_b = 2$, $\tau = 200$, 2000 Monte Carlo iterations

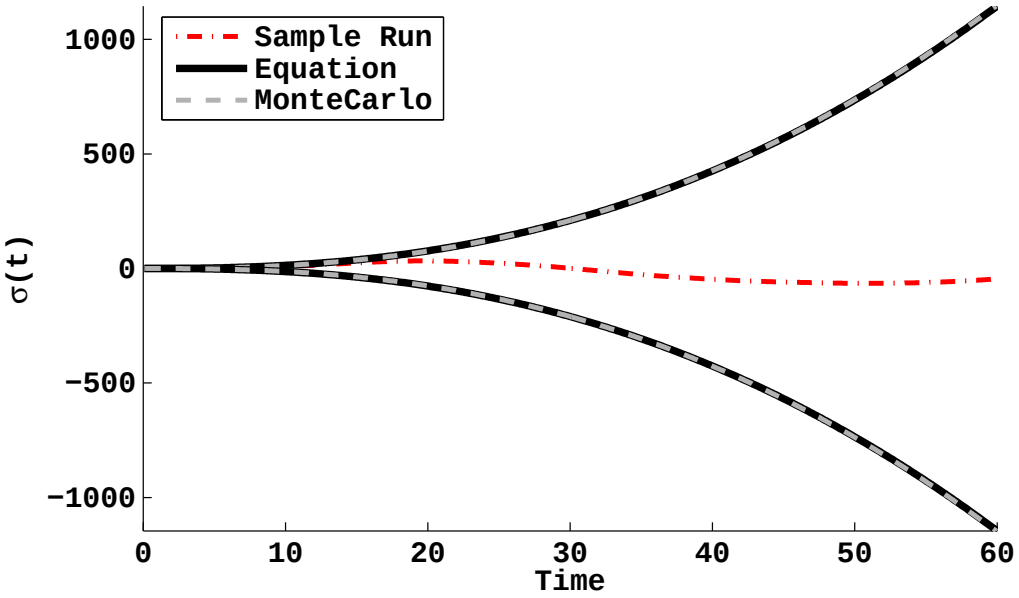

Figure 3.6: Standard Deviation of Double Integrated Gauss-Markov Process: 10Hz, σ_b = 2, τ = 200, 2000 Monte Carlo iterations

3.7 Application Example

While the results obtained in this chapter are in direct support of the more general navigation scenarios presented in later chapters, the expressions for the propagation of the errors in this chapter can be directly applied to a single-axis navigation scenario. It is the purpose of this section to illustrate the use of such expressions with such an example.

Suppose a body is constrained to move in a straight line trajectory as depicted by Figure 3.7. Suppose additionally that the sensitive axis of an accelerometer is coincident with the traveling direction of the body. The accelerometer specifications of random walk, bias drift variance, time constant, and sample frequency are known and the sensor has been fully calibrated to remove any constant bias or effects due to temperature. The

output of the calibrated measurement is integrated to obtain the velocity and position for a given acceleration profile along a straight line position trajectory. For each time step, in addition to the values of velocity and position, the results of this chapter can provide the expected accuracy of the acceleration, velocity, and position.

Figure 3.7: Body Constrained to Travel in One Direction

Assume the sensor specifications for the accelerometer are given in Table 3.3. These specifications represent a low grade accelerometer with an exaggerated bias magnitude.

Table 3.3: Sample Accelerometer Specifications

Specification	Value
f_s	10 Hz
σ_ω^2	0.5 $\frac{m}{s^2}$
σ_b^2	0.25 $\frac{m}{s^2}$
τ	200 s

For any acceleration profile, a, in a single direction, the mean value of the velocity, V and position P in the same direction are simply the integral values of the true

acceleration. The mean values represent the Euler integration of true sensor outputs.

$$\mathrm{E}[V(k)] = \Delta t \sum_{i=0}^{k} a_i \quad \text{meters per second} \tag{3.57}$$

$$\mathrm{E}[P(k)] = \Delta t^2 \sum_{j=0}^{k} \sum_{i=0}^{j} a_i \quad \text{meters} \tag{3.58}$$

The variance of the the velocity, V, is the sum of the variances of the error contributions from integrated wide-band noise and integrated Markov process as listed in Tables 3.1 and 3.2.

$$\sigma^2{}_V(k) = \sigma^2{}_{\int \epsilon}(k) \tag{3.59}$$

$$= \sigma^2{}_{\int \omega}(k) + \sigma^2{}_{\int b}(k) \tag{3.60}$$

The variance of the the position, P, is the sum of the variances of the error contributions from double integrated wide-band noise and double integrated Markov process as listed in Tables 3.1 and 3.2.

$$\sigma^2{}_P(k) = \sigma^2{}_{\int\int \epsilon}(k) \tag{3.61}$$

$$= \sigma^2{}_{\int\int \omega}(k) + \sigma^2{}_{\int\int b}(k) \tag{3.62}$$

To demonstrate these results, consider the sinusoidal acceleration profile as shown in Figure 3.8. This noisy accelerometer when integrated gives the velocity is shown in Figure 3.9. Another step of integration gives the position shown in Figure 3.9. As is evident by the plots, the 1-σ bounds show that the error growth becomes larger in time and with each level of integration. The bounds shown in the plots can be thought of

as a time-dependent corridor in which the integral values of velocity and position are expected to reside. As all error processes are Gaussian, the 1-σ bounds plotted in Figures 3.9 and 3.10 specify the region where approximately 66.7 percent of all trajectories are expected to travel.

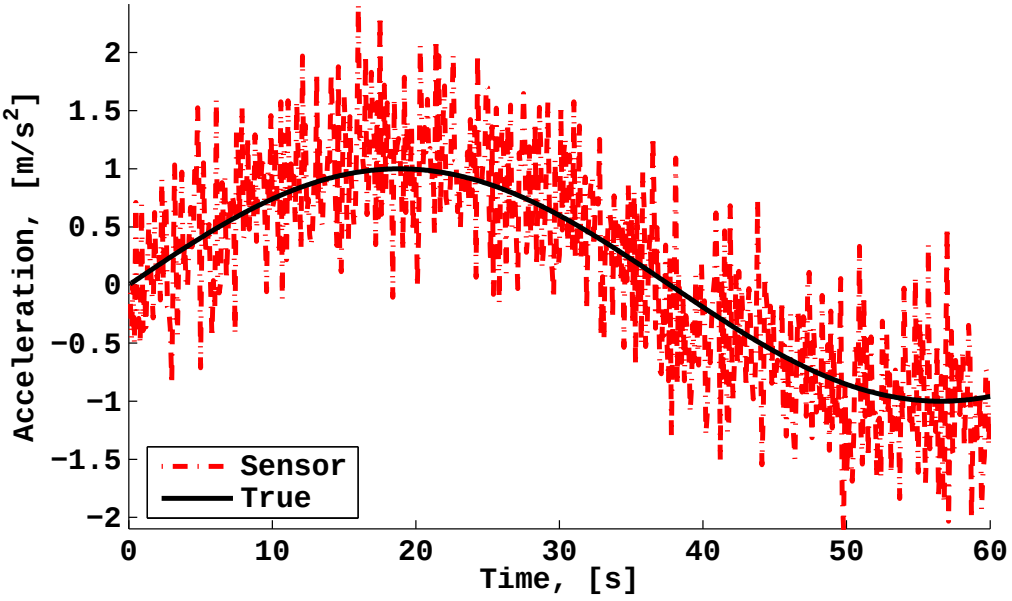

Figure 3.8: Simulated Acceleration Profile: 10Hz, $\sigma_\omega = 0.5$, $\sigma_b = 0.25$, $\tau = 200$

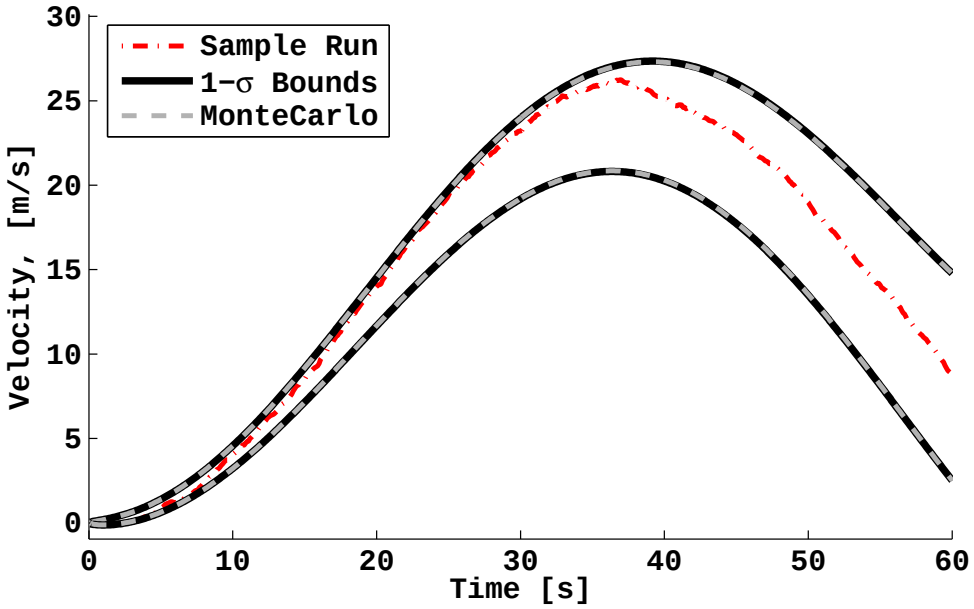

Figure 3.9: Velocity with Bounds from Accel Profile

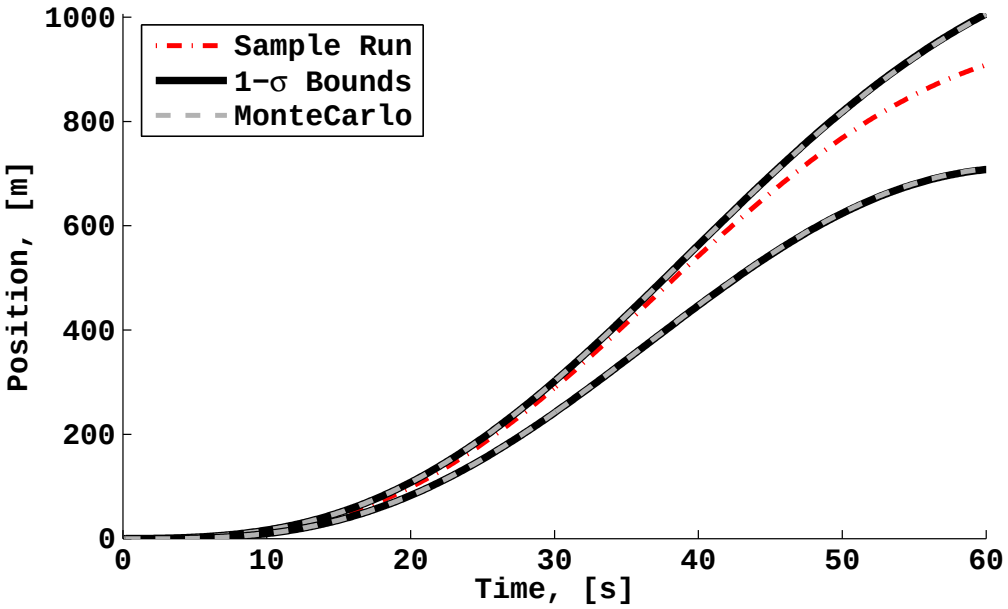

Figure 3.10: Position with Bounds from Accel Profile

3.8 Illustration of Results

Inertial sensors exhibit varying magnitudes of each of their component error processes as well as the characteristic time constant of the drifting component. The following sections illustrate the effect of the component stochastic process parameters on the growth of the variance of the total integrated sensor values.

3.8.1 Relative Magnitudes

The two stochastic error processes, when integrated, each uniquely contribute to variance function of the integrated sensor output. A sensor's wide-band noise component will dominate the error for short integration intervals while the drifting bias dominates for longer durations. This relative effect of each can be investigated by observing the effect of adjusting the ratio of the process magnitudes, $\frac{\sigma_b}{\sigma_w}$, on the variance function of the integrated output for a fixed time constant. Setting the wide-band noise standard deviation to 1, Figures 3.11, 3.12, and 3.13 and show the 1-σ bounds of the integrated sensor output for various ranges of the bias drift standard deviation.

Since the rate of increase of the integrated bias drift variance is higher than that of the integrated wide-band noise for any relative ratio, even small relative bias magnitudes will cause the bias to eventually dominate the variance growth. The general effect of the relative ratio is that an increase Gauss-Markov process magnitude, σ_b, causes it to dominate sooner, resulting in a larger rate of error growth in the integrated sensor output.

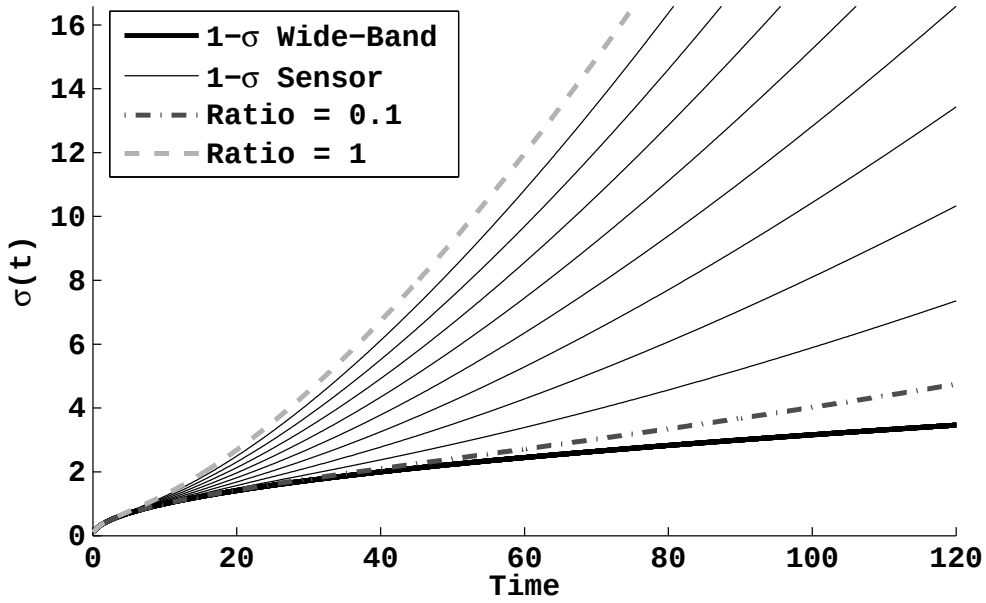

Figure 3.11: Integrated Sensor 1-σ Bounds for Ratio from 0.1 to 1

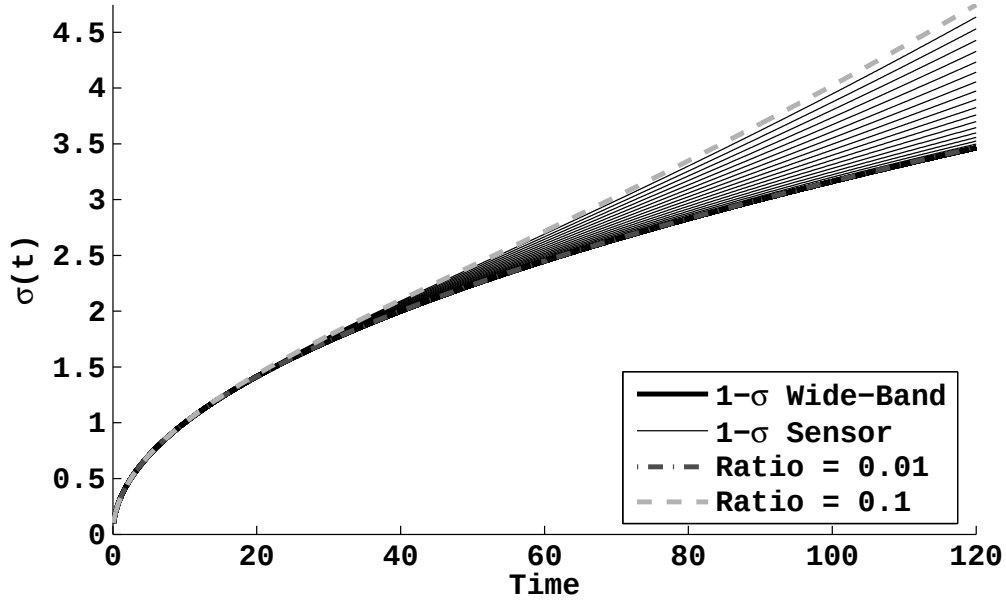

Figure 3.12: Integrated Sensor 1-σ Bounds for Ratio from 0.01 to 0.1

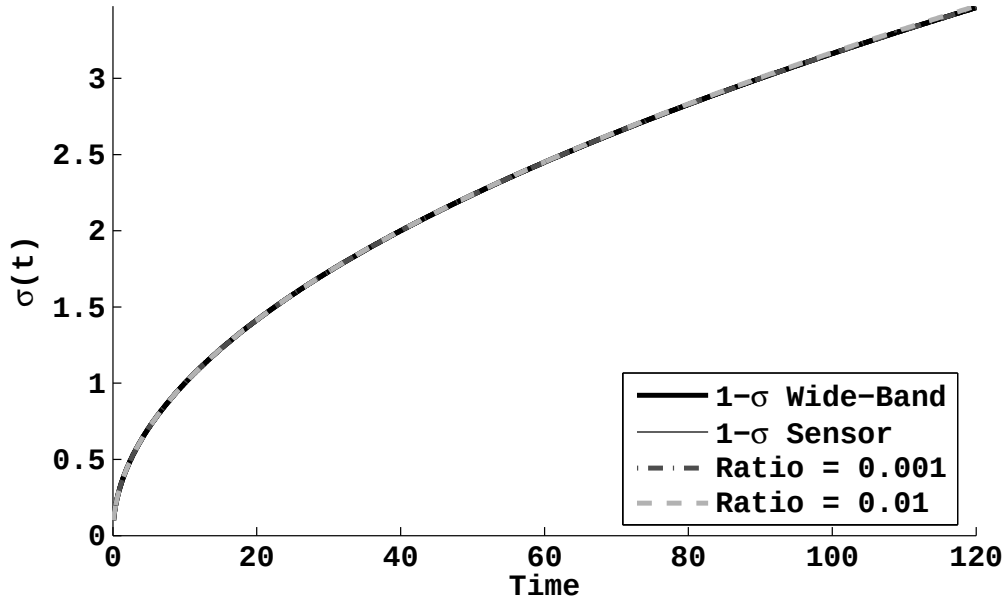

Figure 3.13: Integrated Sensor 1-σ Bounds for Ratio from 0.001 to 0.1

3.8.2 Effect of Time Constant

For a fixed relative magnitude of 0.1, Figure 3.14 illustrates the shape of the bounds for various values of the Markov model time constant, τ. For the range of time constants shown, larger values of τ cause a slower increase in the rate of error propagation, while lower values indicate a faster increase.

For a fixed relative magnitude of 0.1, Figure 3.15 illustrates the effect of a larger range of τ on the value of the integrated sensor error bounds at a particular time of 120 units. For very small values of τ, the initial conditions of the Markov model dominate over the input noise. As the time constant increases, the maximum error value peaks and then levels off in a nonlinear fashion. For most inertial sensors, the time constant is usually much longer than values corresponding to the peak. The result of Figure 3.14 best describes the effect of time constant within its expected range.

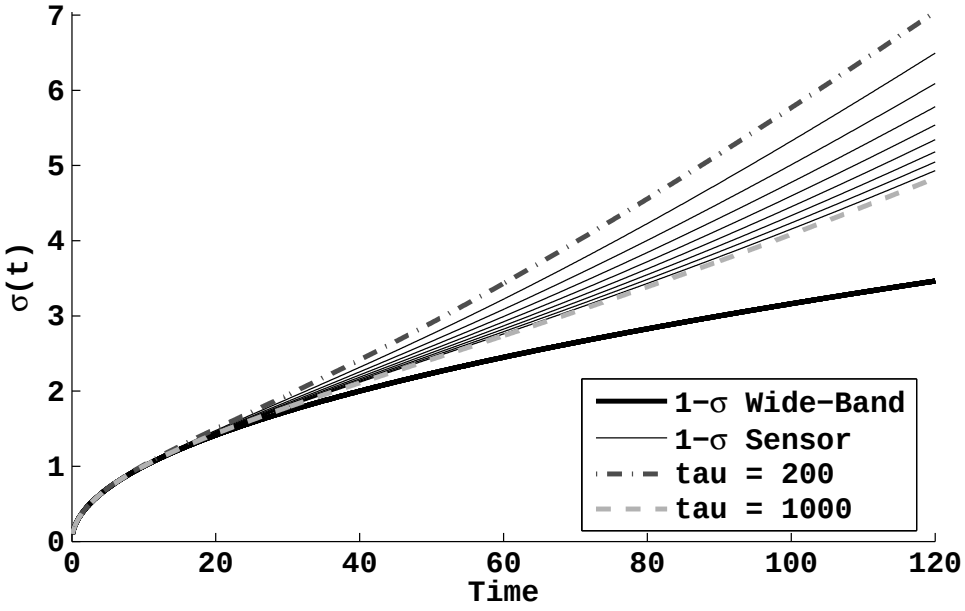

Figure 3.14: Integrated Sensor 1-σ Bounds for Fixed Ratio of 0.1 and τ Between 200 to 1000

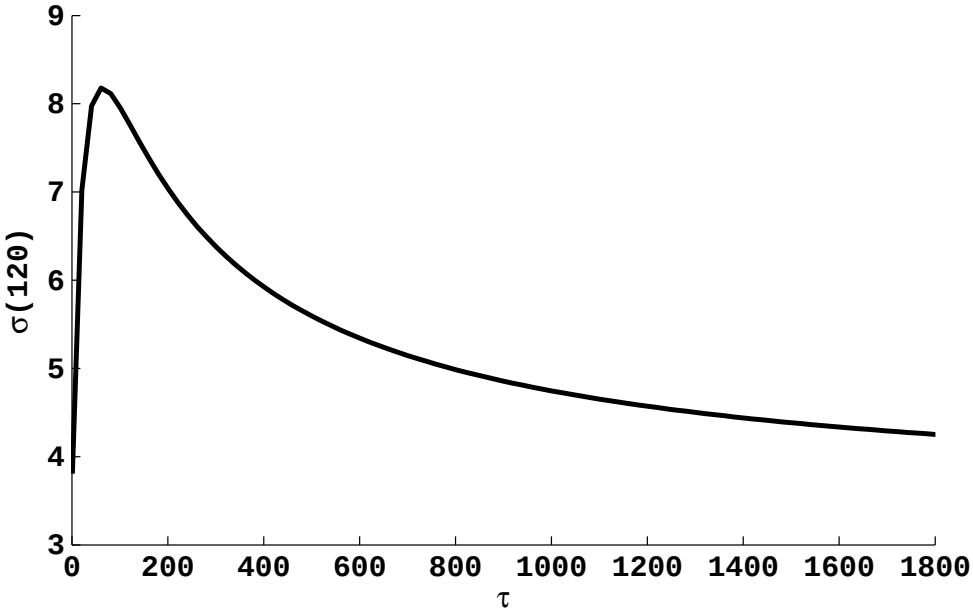

Figure 3.15: Value of Integrated 1-σ Bounds at time index of 120 for Fixed Ratio of 0.1 and τ Between 200 to 1000

3.9 Conclusion

In this chapter, analytical variance expressions have been derived which quantify the error growth of subsequent integrations of inertial sensors exhibiting the assumed stochastic model forms of Chapter 2. A Monte Carlo simulation of the stochastic processes was used to validate the analytical results and further simulations illustrated the use of the expressions in the quantification of accuracy for the single-axis case. The final sections of this chapter showed the relative and total effects of the three stochastic model parameters on the resulting variance functions of the integrated sensor. The results of this chapter are used in direct support of derived expressions and analysis for the planar navigation scenario studied in Chapter 4.

Chapter 4

Two Dimensional Error Propagation

4.1 Introduction

In order to describe the most general motion of a navigating vehicle, six degrees of freedom are required. An inertial measurement unit (IMU) attached to the navigating body takes measurements of these six degrees of freedom which include three orthogonal accelerations (a_x,a_y,a_z) and three orthogonal rotation rates (g_x,g_y,g_z). In order to navigate within a suitable frame of reference such as on the surface of the earth, these measurements must be transformed and integrated to values of orientation, velocity, and position in that frame. For vehicles traveling within short ranges on the earth, a suitable frame of reference is a simple cartesian coordinate system in which North, East, Down (NED) axes are aligned according to the right-hand rule. The orientation of the vehicle in this navigation frame can be described by roll (ϕ), pitch (θ), and yaw (ψ) angles as defined about the North, East, and Down axes, respectively. Figure 4.1 is a three-dimensional diagram depicting the body frame and navigation frame coordinate systems.

It the task of the inertial navigator to perform the necessary operations on the body frame measurements to achieve the desired navigation frame values. This process of operating on the inertial measurements is referred to as inertial *mechanization*. For the 6-DOF scenario the mechanization equations are non-linear and require several calculations involving multiple measurements (see Chapter 5). If, however, the vehicle operates under some kinematic constraints, the resulting governing equations may be greatly simplified.

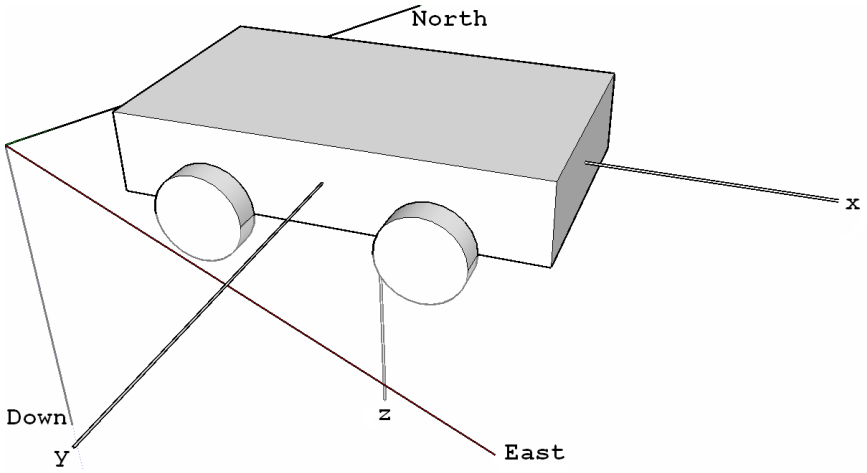

Figure 4.1: Simplified Coordinate Frame

This chapter focuses its attention on the planar navigation scenario in which a vehicle is constrained to move on a North-East plane. Figure (4.2) depicts the simplified motion of the constrained body. The body can translate in the north and east directions and rotate only about the direction orthogonal to the plane. The rotation rate sensed by a gyro about the z-axis on the constrained body is the same as the rotation rate about the down axis in the navigation frame. The yaw angle, ψ, as measured positive from north about the down axis in the navigation frame requires no transformation to the navigation frame and is directly related to the sensed yaw rate, g_z, by simple integration.

The vehicle in this planar navigation scenario, depending upon its capability and trajectory, can operate under additional kinematic constraints. For general motion, the vehicle experiences *side-slip*, in which the body experiences velocity in both the direction it is pointing, body frame x known as *heading* (longitudinal direction), and the body frame y direction (lateral direction). This is the case on many vehicles in which high dynamic maneuvers force the body to point in a direction incoincident with its path of motion. Figure 4.3 shows the dynamic equations for use in navigating a

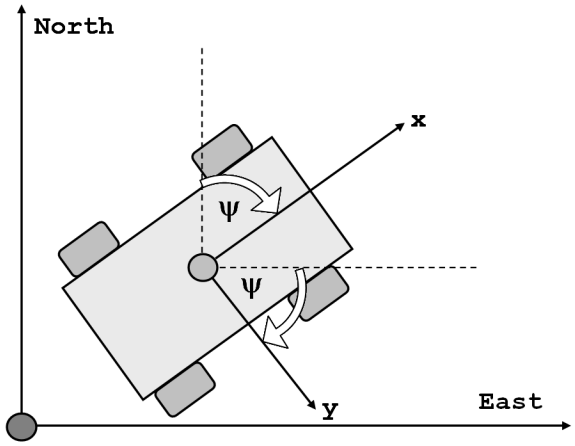

Figure 4.2: Simplified Coordinate Frame 2D

side-slipping vehicle with inertial measurements. As is evident by the diagram, the gyro is first integrated and then used in transforming the acceleration measurements to the navigation frame. The transformed accelerations are then integrated once for velocity, and twice for position.

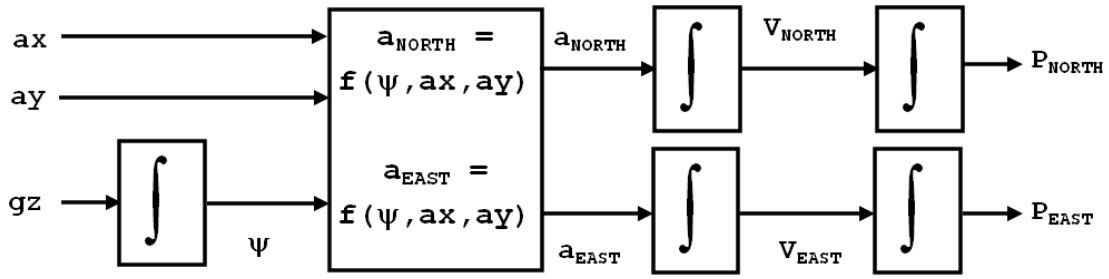

Figure 4.3: Navigation Relationships for Side-Slip Vehicle

For many four-wheeled vehicles performing more moderate maneuvers, the velocity of the body can be assumed to be strictly coincident with its heading (body frame x). In this scenario, the body moves only in the direction it is pointing and is considered to be operating under the *no-slip* condition. For the no-slip case described above, the dynamic

relationships between the inertial measurements and navigation frame vehicle states of velocity and position simplify even further. These simplified relationships for the no-slip case are shown in Figure 4.4. Similar to the case with side-slip, the navigation frame values of velocity and position are ascertained from the subsequent integrations. However, in this no-slip case, the velocity is solely derived from integrating the longitudinal accelerometer, a_x. Consequently, the acceleration, requires no transformation with the integrated gyro and the lateral accelerometer, a_y, is not necessary for navigation. As a result, inertial navigation for the no-slip case requires one less integration and one less measurement. This observation is shown later in this chapter to offer some potential dead-reckoning improvement when such kinematic assumptions are valid.

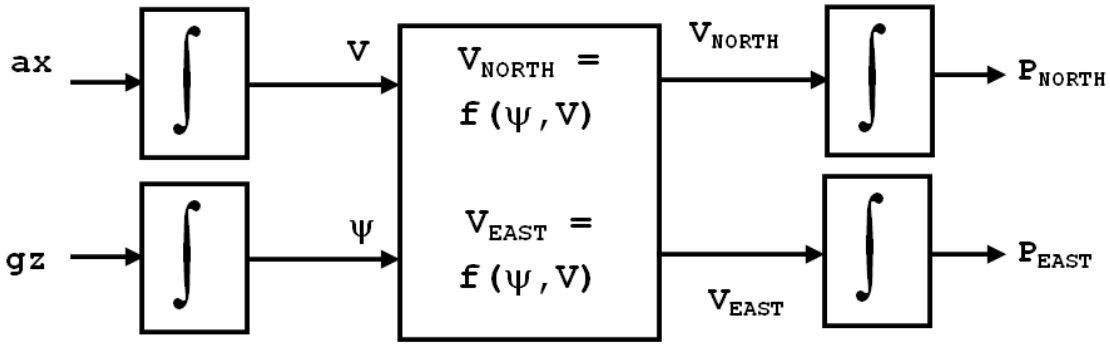

Figure 4.4: Navigation Relationships for Vehicle with No-Slip

Using results from and a similar approach to Chapter 3, this chapter presents a derivation of the propagation of navigation-frame velocity errors for the planar no-slip case as shown in Figure 4.4. For bodies that operate under such kinematic constraints, the resulting variance expressions provide the accuracy expected when dead-reckoning with the applicable dynamic equations and choice of inertial sensors. The resulting velocity expressions are validated with the same type of Monte Carlo simulations as used

in Chapter 3. Following the no-slip case is a discussion of the additional requirements for the case where a vehicle is expected to slip. Variance expressions for the transformation of accelerations for the no-slip case are presented. This chapter concludes by demonstrating the additional error induced when employing the slip equations for a non-slip trajectory.

4.2 Velocity Error in Navigation Frame Under No-Slip Planar Motion

This section derives expressions for the variance of the 2-D velocity as derived from the minimum amount of inertial measurements necessary. The basic method used below defines the simplest governing inertial navigation relationships, substitutes the inertial measurement errors, and applies the expectation operator to the squared expressions. Using small angle approximations, the expressions can be simplified to show a linear propagation of sensor errors from the IMU to the vehicle states.

For the navigating body in the planar scenario, the yaw angle of the vehicle is derived by direct integration of the rotation rate sensed about the axis aligned orthogonal to the plane, g_z.

$$\psi = \int g_z \, dt \tag{4.1}$$

The velocity, V, of the body is always tangential to its path under the no-slip condition, and therefore can be derived from the acceleration sensed along the its x axis (a_x accelerometer) by the integral relationship

$$V = \int a_x \, dt \tag{4.2}$$

Assuming Euler integration of the above quantities, the preceding integrals are reduced to summations

$$V_k = \Delta t \sum_{i=0}^{k-1} a_x + V_0 \tag{4.3}$$

$$\psi_k = \Delta t \sum_{i=0}^{k-1} g_z + \psi_0 \tag{4.4}$$

The rate gyro and accelerometer inertial measurements are corrupted by stochastic error sources, ϵ_g, and ϵ_a as introduced and quantified in earlier chapters. The total velocity and yaw angle can therefore be expressed as

$$\begin{aligned} V_k &= \Delta t \sum_{i=0}^{k-1} (a + \epsilon_a) + V_0 \\ &= \Delta t \sum_{i=0}^{k-1} a + \Delta t \sum_{i=0}^{k-1} \epsilon_a + V_0 \end{aligned} \tag{4.5}$$

$$\begin{aligned} \psi_k &= \Delta t \sum_{i=0}^{k-1} (g + \epsilon_g) + \psi_0 \\ &= \Delta t \sum_{i=0}^{k-1} g + \Delta t \sum_{i=0}^{k-1} \epsilon_g + \psi_0 \end{aligned} \tag{4.6}$$

For the clarity in the derivations following it is helpful to redefine the above equations with simpler notation. Note that despite the removal of subscript, k, the values are still

functions of time.

$$A = \Delta t \sum_{i=0}^{k-1} a + V_0 \tag{4.7}$$

$$B = \Delta t \sum_{i=0}^{k-1} \epsilon_a \tag{4.8}$$

$$\alpha = \Delta t \sum_{i=0}^{k-1} g + \psi_0 \tag{4.9}$$

$$\beta = \Delta t \sum_{i=0}^{k-1} \epsilon_g \tag{4.10}$$

In summary, A and α represent the velocity and yaw angle as derived from Euler integration of the mean sensor outputs and B and β represent the error due to the integrated accelerometer and rate gyro, respectively.

4.2.1 Mean and Variance of East Velocity

The velocity in the east direction under this scenario is computed by taking the resultant velocity from the accelerometer and transforming it into the east component direction using the resultant yaw angle from the rate gyro.

$$\begin{aligned} V_{EASTk} &= V \sin(\psi) \\ &= \left(\Delta t \sum_{i=0}^{k-1} a + V_0 + \Delta t \sum_{i=0}^{k-1} \epsilon_a \right) \sin(\Delta t \sum_{i=0}^{k-1} g + \psi_0 + \Delta t \sum_{i=0}^{k-1} \epsilon_g) \\ &= (A + B) \sin(\alpha + \beta) \end{aligned} \tag{4.11}$$

Using a trigonometric identity, the sine factor is expanded as shown below

$$V_{EASTk} = (A + B) \left(\sin(\alpha) \cos(\beta) + \cos(\alpha) \sin(\beta) \right) \tag{4.12}$$

Provided that the integrated gyro error, β, is sufficiently small, small-angle approximations of Equations (4.13) and (4.14) can be made.

$$\cos\beta \approx 1 \tag{4.13}$$

$$\sin\beta \approx \beta \tag{4.14}$$

In general, this small-angle approximation is valid within the typical range of interest. As the integrated sensor error grows outside the region for which the assumption is valid ($|\beta| < 10$ degrees), the resulting velocity and position errors exceed the range of accuracy in which this research seeks to quantify.

The small angle approximation results in the simplified expression for the east velocity

$$V_{EASTk} = (A+B)\left(\sin(\alpha)+\cos(\alpha)\beta\right) \tag{4.15}$$

The mean function of velocity in the east direction is found by taking the expected value.

$$\begin{aligned} \mathrm{E}\left[V_{EASTk}\right] &= \mathrm{E}\left[(A+B)\left(\sin(\alpha)+\cos(\alpha)\beta\right)\right] \\ &= A\sin\alpha + \sin\alpha\mathrm{E}[B] + A\cos\alpha\mathrm{E}[\beta] + \cos\alpha\mathrm{E}[B\beta] \end{aligned} \tag{4.16}$$

Since the stochastic errors are zero mean, the mean of the east velocity is simply the true value ascertained from the true part of the inertial measurements.

$$\mathrm{E}\left[V_{EASTk}\right] = A\cos\alpha \tag{4.17}$$

To derive the variance of the east velocity, it is first squared as shown below

$$\begin{aligned}(V_{EASTk})^2 &= \big(A\sin\alpha + \sin\alpha B + A\cos\alpha\beta + \cos\alpha B\beta\big)^2 \\ &= A^2\sin^2(\alpha) + A^2\cos^2\alpha\beta^2 + \sin^2\alpha B^2 + \cos\alpha^2 B^2\beta^2 \\ &\quad + 2A^2\sin\alpha\cos\alpha\beta + 2AB\sin^2\alpha + 4AB\sin\alpha\cos\alpha\beta \\ &\quad + 2AB\cos^2\alpha\beta^2 + 2B^2\sin\alpha\cos\alpha\beta \end{aligned} \tag{4.18}$$

Next, the expected value of the squared expression is taken as follows

$$\begin{aligned}\mathrm{E}\big[(V_{EASTk})^2\big] &= A^2\sin^2(\alpha) + A^2\cos^2\alpha\mathrm{E}\big[\beta^2\big] + \sin^2\alpha\mathrm{E}\big[B^2\big] + \cos\alpha^2\mathrm{E}\big[B^2\beta^2\big] \\ &\quad + 2A^2\sin\alpha\cos\alpha\mathrm{E}\big[\beta\big] + 2A\sin^2\alpha\mathrm{E}\big[B\big] + 4A\sin\alpha\cos\alpha\mathrm{E}\big[B\beta\big] \\ &\quad + 2A\cos^2\alpha\mathrm{E}\big[B\beta^2\big] + 2\sin\alpha\cos\alpha\mathrm{E}\big[B^2\beta\big] \end{aligned} \tag{4.19}$$

Assuming the two stochastic sources are independent, the expression reduces to

$$\begin{aligned}\mathrm{E}\big[(V_{EASTk})^2\big] &= A^2\sin^2(\alpha) + A^2\cos^2\alpha\mathrm{E}\big[\beta^2\big] \\ &\quad + \sin^2\alpha\mathrm{E}\big[B^2\big] + \cos^2\alpha\mathrm{E}\big[B^2\big]\mathrm{E}\big[\beta^2\big] \end{aligned} \tag{4.20}$$

Computing the variance of the expression gives the following result

$$\begin{aligned}\mathrm{VAR}\big[(V_{EASTk})^2\big] &= \mathrm{E}\big[(V_{EASTk})^2\big] - \mathrm{E}\big[(V_{EASTk})\big]^2 \\ &= A^2\cos^2\alpha\mathrm{E}\big[\beta^2\big] + \sin^2\alpha\mathrm{E}\big[B^2\big] + \cos^2\alpha\mathrm{E}\big[B^2\big]\mathrm{E}\big[\beta^2\big] \end{aligned} \tag{4.21}$$

Recall from Equations (4.8) and (4.10), that B is the integrated accelerometer error and B is the integrated gyro error. The variances of the integrated inertial sensors were derived in Chapter 3 and shown again here

$$\mathrm{E}\big[B^2\big] = \sigma^2_{\int \epsilon_a} \tag{4.22}$$

$$\mathrm{E}\big[\beta^2\big] = \sigma^2_{\int \epsilon_g} \tag{4.23}$$

Where, $\sigma^2_{\int \epsilon_a}$ is the variance of the integrated accelerometer errors and $\sigma^2_{\int \epsilon_g}$ is the variance of the integrated gyro errors.

The expressions are substituted below to yield the variance function of east velocity

$$\sigma^2_{V_{EAST}}(k) = V^2 \cos^2\psi \sigma^2_{\int \epsilon_g} + \sin^2\psi \sigma^2_{\int \epsilon_a} + \cos^2\psi \sigma^2_{\int \epsilon_a} \sigma^2_{\int \epsilon_g} \tag{4.24}$$

Equation (4.24) shows that the variance is a three-termed expression consisting of the trajectory (velocity and heading) and the variances of the integrate accelerometer and integrated gyro. The last term includes the product of the two latter variances indicating that the variance of east velocity is not Gaussian distributed. However, for sufficiently large values of velocity, V , the first term dominates and the east velocity is approximately Gaussian.

4.2.2 Mean and Variance of North Velocity

The velocity in the North direction under this scenario is computed by taking the resultant velocity from the accelerometer and transforming it into the North component

velocity using the resultant yaw angle from the rate gyro.

$$\begin{aligned} V_{NORTHk} &= V\cos(\psi) \\ &= \left(\Delta t\sum_{i=0}^{k-1} a + V_0 + \Delta t\sum_{i=0}^{k-1}\epsilon_a\right)\cos(\Delta t\sum_{i=0}^{k-1} g + \psi_0 + \Delta t\sum_{i=0}^{k-1}\epsilon_g) \\ &= (A+B)\cos(\alpha+\beta) \end{aligned} \tag{4.25}$$

Using a trigonometric identity, the cosine factor is expanded as shown below

$$V_{NORTHk} = (A+B)\left(\cos(\alpha)\cos(\beta) - \sin(\alpha)\sin(\beta)\right) \tag{4.26}$$

Using the same small angle approximations shown before in Equations (4.13) and (4.14), the expression reduces to

$$V_{NORTHk} = (A+B)\left(\cos(\alpha) + \sin(\alpha)\beta\right) \tag{4.27}$$

The mean function of velocity in the north direction is found by taking the expected value

$$\begin{aligned} \mathrm{E}\left[V_{NORTHk}\right] &= \mathrm{E}\left[(A+B)\left(\cos(\alpha)+\sin(\alpha)\beta\right)\right] \\ &= A\cos\alpha + \cos\alpha\mathrm{E}[B] + A\sin\alpha\mathrm{E}[\beta] + \sin\alpha\mathrm{E}[B\beta] \end{aligned} \tag{4.28}$$

Since the stochastic errors are zero mean, the mean of the north velocity is simply the true value ascertained from the true part of the inertial measurements

$$\mathrm{E}\left[V_{NORTHk}\right] = A\cos\alpha \tag{4.29}$$

To derive the variance of the north velocity, it is first squared as shown below

$$\begin{aligned}(V_{NORTHk})^2 &= \big(A\cos\alpha + \cos\alpha B + A\sin\alpha\beta + \sin\alpha B\beta\big)^2 \\ &= A^2\cos^2(\alpha) + A^2\sin^2\alpha\beta^2 + \cos^2\alpha B^2 + \sin\alpha^2 B^2\beta^2 \\ &\quad + 2A^2\cos\alpha\sin\alpha\beta + 2AB\cos^2\alpha + 4AB\cos\alpha\sin\alpha\beta \\ &\quad + 2AB\sin^2\alpha\beta^2 + 2B^2\cos\alpha\sin\alpha\beta \end{aligned} \tag{4.30}$$

Next, taking the expected value of the squared expression gives

$$\begin{aligned}\mathrm{E}\big[(V_{NORTHk})^2\big] &= A^2\cos^2(\alpha) + A^2\sin^2\alpha\mathrm{E}\big[\beta^2\big] + \cos^2\alpha\mathrm{E}\big[B^2\big] + \sin\alpha^2\mathrm{E}\big[B^2\beta^2\big] \\ &\quad + 2A^2\cos\alpha\sin\alpha\mathrm{E}\big[\beta\big] + 2A\cos^2\alpha\mathrm{E}\big[B\big] + 4A\cos\alpha\sin\alpha\mathrm{E}\big[B\beta\big] \\ &\quad + 2A\sin^2\alpha\mathrm{E}\big[B\beta^2\big] + 2\cos\alpha\sin\alpha\mathrm{E}\big[B^2\beta\big] \end{aligned} \tag{4.31}$$

Assuming the two stochastic sources are independent and zero mean, the expression reduces to

$$\begin{aligned}\mathrm{E}\big[(V_{NORTHk})^2\big] &= A^2\cos^2(\alpha) + A^2\sin^2\alpha\mathrm{E}\big[\beta^2\big] \\ &\quad + \cos^2\alpha\mathrm{E}\big[B^2\big] + \sin^2\alpha\mathrm{E}\big[B^2\big]\mathrm{E}\big[\beta^2\big] \end{aligned} \tag{4.32}$$

Computing the variance of the expression gives the terms

$$\begin{aligned}\mathrm{VAR}\big[(V_{NORTHk})^2\big] &= \mathrm{E}\big[(V_{NORTHk})^2\big] - \mathrm{E}\big[(V_{NORTHk})\big]^2 \\ &= A^2\sin^2\alpha\mathrm{E}\big[\beta^2\big] + \cos^2\alpha\mathrm{E}\big[B^2\big] + \sin^2\alpha\mathrm{E}\big[B^2\big]\mathrm{E}\big[\beta^2\big] \end{aligned} \tag{4.33}$$

Where, α is the integrated accelerometer error and B is the integrated gyro error. The variances of these integrated inertial sensors are derived in Chapter 3 and shown again here

$$\mathrm{E}\big[B^2\big] = \sigma^2_{\int \epsilon_a} \tag{4.34}$$

$$\mathrm{E}\big[\beta^2\big] = \sigma^2_{\int \epsilon_g} \tag{4.35}$$

Where, $\sigma^2_{\int \epsilon_a}$ is the variance of the integrated accelerometer errors and $\sigma^2_{\int \epsilon_g}$ is the variance of the integrated gyro errors.

Substituting the known integrated error variances gives the variance function for the north velocity.

$$\sigma^2_{V_{NORTH}}(k) = V^2 \sin^2\psi\sigma^2_{\int \epsilon_g} + \cos^2\psi\sigma^2_{\int \epsilon_a} + \sin^2\psi\sigma^2_{\int \epsilon_a}\sigma^2_{\int \epsilon_g} \tag{4.36}$$

As shown above for the east velocity in Equation (4.24) it is evident that for relatively large velocities, the north velocity is approximately Gaussian due to the dominance of the first term of Equation (4.36) over the third term.

4.2.3 Cross Covariance of North and East Velocity

To supplement the characterization of the velocity error for this planar no-slip scenario, the cross-covariance between the north and east components is derived as follows.

The cross covariance is defined as

$$\mathrm{COV}\big[V_{NORTHk}V_{EASTk}\big] =$$

$$\mathrm{E}\big[(V_{NORTHk} - \mathrm{E}[V_{NORTH}])(V_{EASTk} - \mathrm{E}[V_{EAST}])\big] \tag{4.37}$$

Using the linear approximation from Equations (4.13) and (4.14) results in

$$\begin{aligned}&\mathrm{COV}\big[V_{NORTHk}V_{EASTk}\big] = \\ &\mathrm{E}\big[(B\cos\alpha - A\sin\alpha\beta - B\sin\alpha\beta)(B\sin\alpha + A\cos\alpha\beta + B\cos\alpha\beta)\big] \end{aligned} \tag{4.38}$$

Next, the expectation operator is expanded and shown below

$$\begin{aligned}\mathrm{COV}\big[V_{NORTHk}V_{EASTk}\big] &= \mathrm{E}\Big[B^2\cos\alpha\sin\alpha + A\cos^2\alpha\beta + \cos^2\alpha B^2\beta - A\sin^2\alpha B\beta \\ &\quad -A^2\sin\alpha\cos\alpha\beta^2 - 2A\sin\alpha\cos\alpha B\beta^2 - \sin^2\alpha B^2\beta - \\ &\quad \sin\alpha\cos\alpha B^2\beta^2\Big] \\ &= \cos\alpha\sin\alpha\mathrm{E}\big[B^2\big] + A\cos^2\alpha\mathrm{E}\big[\beta\big] + \cos^2\alpha\mathrm{E}\big[B^2\beta\big] \\ &\quad -A\sin^2\alpha\mathrm{E}\big[B\beta\big] - A^2\sin\alpha\cos\alpha\mathrm{E}\big[\beta^2\big] \qquad (4.39) \\ &\quad -2A\sin\alpha\cos\alpha\mathrm{E}\big[B\beta^2\big] - \sin^2\alpha\mathrm{E}\big[B^2\beta\big] - \\ &\quad \sin\alpha\cos\alpha\mathrm{E}\big[B^2\beta^2\big] \qquad (4.40)\end{aligned}$$

Since the integrated accelerometer error, B, and integrated gyro error, β, are zero mean and uncorrelated, the expression reduces to

$$\begin{aligned}\mathrm{COV}\big[V_{NORTHk}V_{EASTk}\big] &= \cos\alpha\sin\alpha\mathrm{E}\big[B^2\big] - A^2\sin\alpha\cos\alpha\mathrm{E}\big[\beta^2\big] - \\ &\quad \sin\alpha\cos\alpha\mathrm{E}\big[B^2\beta^2\big] \end{aligned} \tag{4.41}$$

The final result is an expression for the cross-covariance of the velocity in the north and east component directions as shown below

$$\mathrm{COV}\big[V_{NORTHk}V_{EASTk}\big] \;=\; \sin\alpha\cos\alpha\Big(\sigma^2_{\int\epsilon_a} - A^2\sigma^2_{\int\epsilon_g} - \sigma^2_{\int\epsilon_a}\sigma^2_{\int\epsilon_g}\Big) \qquad (4.42)$$

4.2.4 Probabilistic Characterization of Velocity Errors

As discussed above, if the velocity is relative large, the north and east velocities ascertained from the no-slip mechanization are approximately Gaussian. Under this condition, the mean, variance, and cross covariance functions derived above completely characterize the propagation of the stochastic sensor errors into the velocity errors for this planar no-slip scenario. The resulting probabilistic characterization is captured for each step in time by a two-dimensional Gaussian surface as described by Equation (4.43).

$$f_V(V_N, V_E) = \frac{1}{2\pi\sigma_{V_N}\sigma_{V_E}\sqrt{1-\rho^2}}\exp\Big[\frac{1}{2(1-\rho^2)}\left(\frac{V_N}{\sigma^2_{V_N}} + \frac{V_E}{\sigma^2_{V_E}} - \frac{2\rho V_N V_E}{\sigma_{V_N}\sigma_{V_E}}\right)\Big] \qquad (4.43)$$

Where, ρ, the correlation coefficient is computed by

$$\rho = \frac{\mathrm{COV}\big[V_{NORTHk}V_{EASTk}\big]}{\sigma_{V_N}\sigma_{V_E}} \qquad (4.44)$$

and $\sigma^2_{V_N}$ and $\sigma^2_{V_E}$ are the variances of velocity in the north and east component directions as derived in the previous sections. Note that the Gaussian surface of Equation (4.43) is centered about zero and thus represents only the deviation from the mean values, which are known from the analysis of the preceding sections in Equations (4.17) and (4.29).

The expressions derived for the variance of the velocity error in the planar no-slip scenario indicate that the shape of the Gaussian surface described by Equation (4.43) is completely characterized at any given time by the instantaneous velocity and yaw angle. The width of its spread is dependent upon both the parameters of the stochastic processes present on the measurements and the time since integration. The stochastic characterization of the two-dimensional no-slip velocity error is therefore, at any given time, *independent of the trajectory history.* In other words, the variance in the velocity error is a function only of (in terms of vehicle trajectory) the instantaneous velocity and yaw angle of the navigating body. This implies that the velocity error for a vehicle that is inertially navigating under the no-slip assumption with the same initial and final conditions can be fully characterized by the variance expressions of Chapter 3.

4.2.5 Validation of the Velocity Error Characterization

The same Monte Carlo validation methodology as for the single axis case in Chapter 3 was used to validate the velocity variance expressions of the preceding sections. The basic idea of the simulation is to first define a North/East Position trajectory in time and numerically differentiate the trajectory to obtain the North/East Velocities. From the velocity, derive a yaw angle assuming the body points tangential to the path and then differentiate to obtain the body frame longitudinal acceleration and yaw rate (under a no-slip assumption). The stochastic errors are then added to the inertial values to simulate the body-frame sensor measurements. Next, the simulated measurements are transformed and integrated to attain the now-corrupted attitude and 2-D velocity. After collecting a sufficient number of simulated integrations, the mean, covariance, and cross-covariance values of the outputs are computed for each step in time. These resulting

variance functions are compared to the analytical expressions using the known simulation parameters.

Since the mean of the resulting velocity components is simply the processed value of the true measurements, only the errors about the mean need be considered. To both illustrate and validate the expressions derived for the velocity accuracy, a candidate position trajectory is chosen as shown in Figure 4.5.

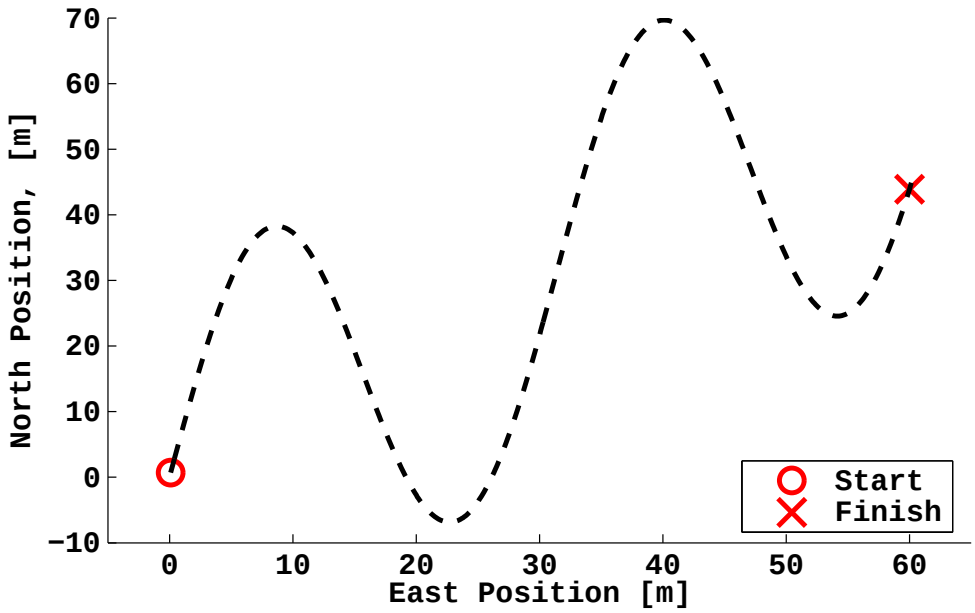

Figure 4.5: Simulated Position Trajectory

Sensor specifications for the accelerometer and gyro chosen relative to trajectory and are listed in Table 4.1. These specifications are taken from a rough identification of a 6-DOF Crossbow IMU-400CD, a medium grade ($3K-$4K) inertial measurement unit. Appendix A demonstrates sensor parameter identification on this particular device.

Table 4.1: Simulated Sensor Specifications

Gyro Spec	Value	Accel Spec	Value
f_s	10 Hz	f_s	10 Hz
σ^2_{rw}	0.14948 deg/s/sqrt(Hz)	σ^2_{rw}	0.000412 g/sqrt(Hz)
σ^2_b	0.0061183 deg/s	σ^2_b	0.000100 g
τ	1300 seconds	τ	500 seconds

The defined position trajectory is processed as described above, and the standard deviation of the velocity errors are computed. Figure 4.6 and 4.7 show comparisons of the computed velocity standard deviation to derived expression for the defined trajectory for the east and north component velocities, respectively. The y-axis is the $3-\sigma$ value of the component velocity representing the corridor of near perfect certainty (greater than 99% probability) within where the velocities are expected to reside.

As can be seen in the plots, the derived variance functions match well with the simulated data. The velocity variance expressions can be observed in Figures 4.6 and 4.7 to exhibit an oscillating type behavior. As can be seen in the derived Equations (4.24) and (4.36), the variance of the component velocities depends upon the instantaneous value of the Velocity, V, as well as the heading, ψ. As ψ is oscillating according to the sinusoidal position trajectory, the variance of the component velocities thus exhibits the effect above.

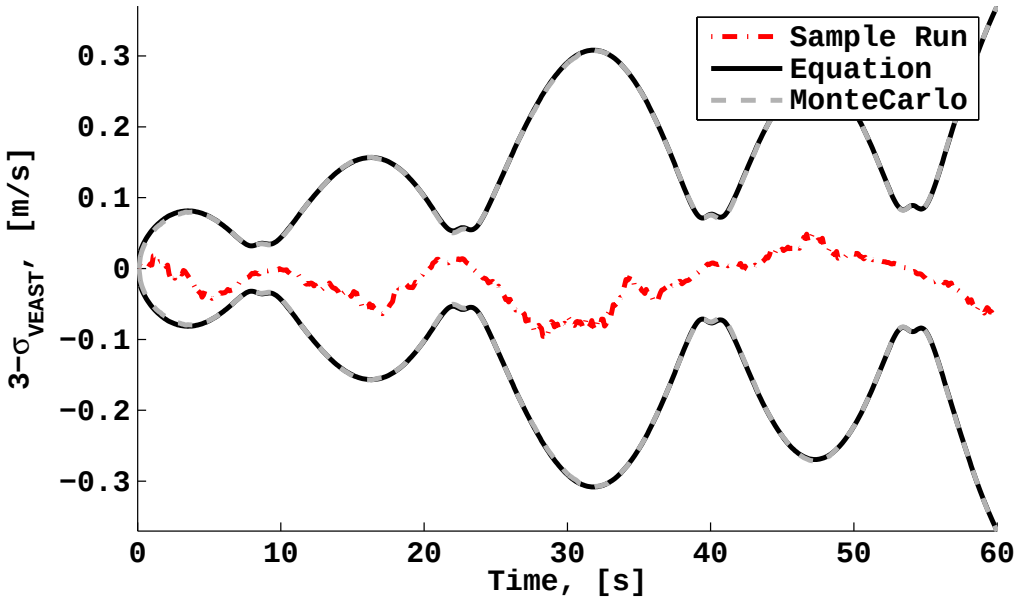

Figure 4.6: Standard Deviation of East Velocity, 2000 Monte Carlo iterations

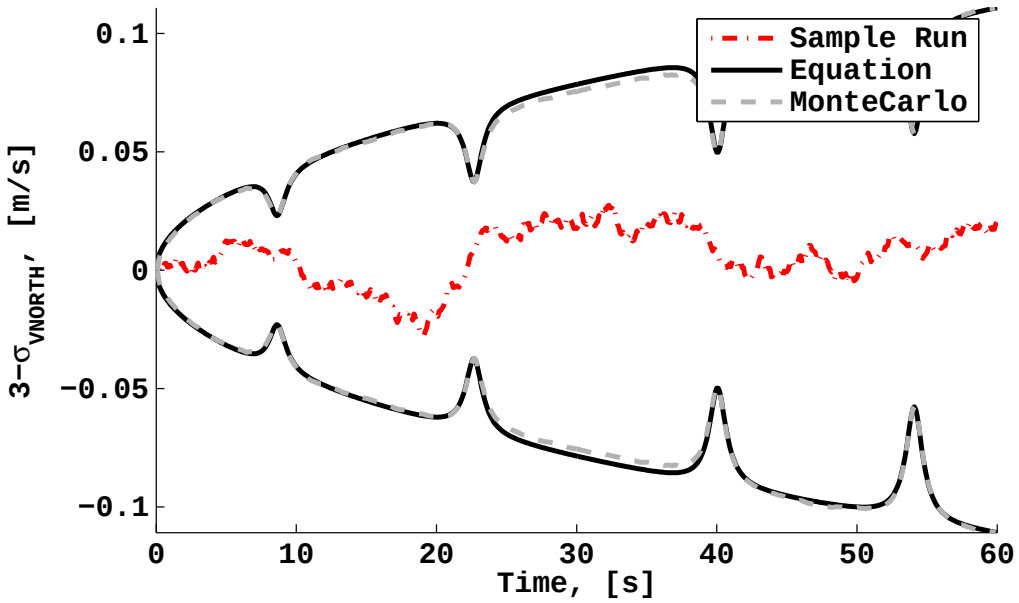

Figure 4.7: Standard Deviation of North Velocity, 2000 Monte Carlo iterations

4.3 Position Error in No-Slip Planar Motion

Due to the added analytical complexity in computing the variance of the planar position for the no-slip scenario, this analysis has not been not completed in closed-form. Instead, this section will show by example of the derivation of east position, the limitations of the current analysis approach and lack of necessary information. The end results of the example derivation make clear the need for more complete statistical characterization of the integrated sensor errors, and is an avenue of future work as described in Chapter 6.

Equation (4.45) below gives the velocity in the east direction using the small angle approximation from the earlier Equation (4.16).

$$\begin{aligned} V_{EASTk} &= (A+B)\left(\sin(\alpha)+\cos(\alpha)\beta\right) \\ &= A\sin\alpha+\sin\alpha B+A\cos\alpha\beta+\cos\alpha B\beta \end{aligned} \tag{4.45}$$

The east position can be derived using the Euler method of numerical integration. The result is expressed below in summation form with the initial condition $P_{EAST0}=0$.

$$P_{EASTk} = \Delta t\sum_{j=0}^{k-1}\left(A\sin\alpha+\sin\alpha B+A\cos\alpha\beta+\cos\alpha B\beta\right) \tag{4.46}$$

The mean value of the east position is straightforward since the stochastic processes, B and β are zero-mean and independent. The mean value is simply the numerical

integration of the deterministic terms in the summation.

$$\begin{aligned} \mathrm{E}\left[P_{EASTk}\right] &= \Delta t \sum_{j=0}^{k-1} \left(A\sin\alpha + \sin\alpha \mathrm{E}[B] + A\cos\alpha \mathrm{E}[\beta] + \cos\alpha \mathrm{E}[B\beta]\right) \\ &= \Delta t \sum_{j=0}^{k-1} A\sin\alpha \end{aligned} \tag{4.47}$$

Using the same approach from the previous sections, in order to derive the east position variance the expression is first squared.

$$\begin{aligned} {P_{EASTk}}^2 &= \left(\Delta t \sum_{j=0}^{k-1} \left(A\sin\alpha + \sin\alpha B + A\cos\alpha\beta + \cos\alpha B\beta\right)\right)^2 \\ &= \Delta t^2 \Bigg(\sum_{j=0}^{k-1} A\cos\alpha \sum_{j=0}^{k-1} A\cos\alpha + \sum_{j=0}^{k-1} \sin\alpha B \sum_{j=0}^{k-1} \sin\alpha B + \\ &\quad \sum_{j=0}^{k-1} A\cos\alpha\beta \sum_{j=0}^{k-1} A\cos\alpha\beta + \sum_{j=0}^{k-1} \cos\alpha B\beta \sum_{j=0}^{k-1} \cos\alpha B\beta + \\ &\quad 2\sum_{j=0}^{k-1} A\sin\alpha \sum_{j=0}^{k-1} \sin\alpha B + 2\sum_{j=0}^{k-1} A\sin\alpha \sum_{j=0}^{k-1} A\cos\alpha\beta + \\ &\quad 2\sum_{j=0}^{k-1} A\sin\alpha \sum_{j=0}^{k-1} \cos\alpha B\beta + 2\sum_{j=0}^{k-1} \sin\alpha B \sum_{j=0}^{k-1} A\cos\alpha\beta + \\ &\quad 2\sum_{j=0}^{k-1} \sin\alpha B \sum_{j=0}^{k-1} \cos\alpha B\beta + \\ &\quad 2\sum_{j=0}^{k-1} A\cos\alpha B \sum_{j=0}^{k-1} \cos\alpha B\beta \Bigg) \end{aligned} \tag{4.48}$$

Since the processes are independent and zero mean taking the expected value of the squared expression cancels out all the "cross-terms" leaving the following expression

$$\begin{aligned}
\mathrm{E}\left[{P_{EAST}}_k{}^2\right] &= \Delta t^2\Bigg(\mathrm{E}\left[\sum_{j=0}^{k-1} A\cos\alpha \sum_{j=0}^{k-1} A\cos\alpha\right] + \mathrm{E}\left[\sum_{j=0}^{k-1} \sin\alpha B \sum_{j=0}^{k-1} \sin\alpha B\right] + \\
&\quad \mathrm{E}\left[\sum_{j=0}^{k-1} A\cos\alpha\beta \sum_{j=0}^{k-1} A\cos\alpha\beta\right] + \\
&\quad \mathrm{E}\left[\sum_{j=0}^{k-1} \cos\alpha B\beta \sum_{j=0}^{k-1} \cos\alpha B\beta\right]\Bigg) \qquad (4.49)
\end{aligned}$$

Taking the variance of the above expression reduces to the following three terms

$$\begin{aligned}
\mathrm{VAR}\left[{P_{EAST}}_k{}^2\right] &= \Delta t^2\Bigg(\mathrm{E}\left[\sum_{j=0}^{k-1} \sin\alpha B \sum_{j=0}^{k-1} \sin\alpha B\right] + \\
&\quad \mathrm{E}\left[\sum_{j=0}^{k-1} A\cos\alpha\beta \sum_{j=0}^{k-1} A\cos\alpha\beta\right] + \\
&\quad \mathrm{E}\left[\sum_{j=0}^{k-1} \cos\alpha B\beta \sum_{j=0}^{k-1} \cos\alpha B\beta\right]\Bigg) \qquad (4.50)
\end{aligned}$$

Observing that each of the three terms in Equation (4.50) have the same basic form, a single expansion is illustrated with an expansion of the first term for $k = 5$.

$$\Delta t^2 \left(\mathrm{E} \left[\sum_{j=0}^{k-1} \sin \alpha\beta \sum_{j=0}^{k-1} \sin \alpha\beta \right] \right) =$$

$$\begin{aligned}
&\Delta t^2 \Big(\sin^2 \alpha_1 {B_1}^2 + \sin^2 \alpha_2 {B_2}^2 + \sin^2 \alpha_3 {B_3}^2 + \sin^2 \alpha_4 {B_4}^2 + \\
&2 \sin \alpha_1 \sin \alpha_2 B_1 B_2 + 2 \sin \alpha_1 \sin \alpha_2 B_1 B_3 + 2 \sin \alpha_1 \sin \alpha_3 B_1 B_4 + \\
&2 \sin \alpha_1 \sin \alpha_2 B_2 B_3 + 2 \sin \alpha_1 \sin \alpha_2 B_2 B_4 + \\
&2 \sin \alpha_1 \sin \alpha_2 B_3 B_4 \Big)
\end{aligned} \tag{4.51}$$

Recognizing the pattern of expansion, this first term can be generalized to the following expression

$$\Delta t^2 \left(\mathrm{E} \left[\sum_{j=0}^{k-1} \sin \alpha\beta \sum_{j=0}^{k-1} \sin \alpha\beta \right] \right) =$$

$$\Delta t^2 \mathrm{E} \left[\sum_{l=0}^{k-1} \sin^2 \alpha_l {B_l}^2 + \sum_{j=0}^{k-1} 2 \sin \alpha_j \sum_{i=j+1}^{k-1} \sin \alpha_i B_j B_i \right] \tag{4.52}$$

Distributing the expectation operator yields the following expression for the expansion of the first term of Equation (4.50)

$$\Delta t^2 \left(\mathrm{E} \left[\sum_{j=0}^{k-1} \sin \alpha\beta \sum_{j=0}^{k-1} \sin \alpha\beta \right] \right) =$$

$$\Delta t^2 \left(\sum_{l=0}^{k-1} \sin^2 \alpha_l \mathrm{E} \left[{B_l}^2 \right] + 2 \sum_{j=0}^{k-1} \sin \alpha_j \sum_{i=j+1}^{k-1} \sin \alpha_i \mathrm{E} \left[B_j B_i \right] \right) \tag{4.53}$$

The variables within the argument of the expectation operators are the integrated accelerometer error, B. While Chapter 3 provides the integrated sensor error variance, $\mathrm{E}\left[{B_l}^2\right]$ in the first summation, no analysis has been done to ascertain the autocorrelation, $\mathrm{E}\left[B_j B_i\right]$ expression in the second double-summation term. While further simplification may be possible by substituting the original integrated stochastic model form of B into the second term summation, the indexed coefficients still remain. Provided that the expectations of Equation (4.53) can be ascertained, the simplification of the expression still remains a difficult task due to the fact that that summations of the coefficients $\sin\alpha$ and $\sin^2\alpha$ may not be able to be simplified or represented by a closed-form expression. As the goal of this thesis is to provide closed-form expressions which bound the propagation of error in terms of ascertainable vehicle states (whether computed or measured), the above analysis remains to be explored in future work.

By example, the sample expansion of the first term of the variance expression of Equation (4.50) has shown difficulty in achieving a solid closed-form expression for the planar position for the no-slip case. In future work, other approaches of analysis may provide a more complete and successful characterization of the errors as propagated in the dynamic equations. However, with the use of Monte Carlo simulations, much insight can be gained regarding the behavior of inertial navigation in various scenarios. The remainder of this thesis will use simulation to exemplify claims resulting from the analysis of inertial navigation in more complex kinematic scenarios. The next section extends the current planar motion error analysis to a vehicle experiencing side-slip.

4.4 Propagation of Error in Planar Motion with Slip

The above sections have derived variance functions that quantify the propagation of inertial sensor errors when the no-slip assumption is valid and corresponding dynamic relationships employed. Under the simplified motion, the dynamic relationships between the body frame and navigation frame vehicle states are such that only one accelerometer and one gyro are required to describe the motion of the vehicle. However, a vehicle experiencing side-slip requires an additional measurement to describe all states of its motion. For the planar case with side-slip, two accelerometers mounted in the body frame x and y directions and a single gyro mounted orthogonal to the plane in the z direction can be used to derive the values of 2-D velocity and position (see Figure 4.2). Due to the kinematics of the slipping motion, the navigation frame states require a coordinate transformation of the two accelerometer measurements (see Figure 4.3). As this coordinate transformation is achieved with the use of the integrated gyro measurement, the resulting navigation frame acceleration components exhibit an unbounded error growth in time. As the states of velocity and position require additional integrations of the transformed accelerations, their accuracy will grow at even faster rates than that of the transformed accelerations. As a result, the slip-case navigation-frame acceleration, velocity, and position will exhibit much higher error growth rates than under the no-slip assumption.

4.4.1 Acceleration Error in Navigation Frame for Slip-Case

In order to illustrate the error growth when the no-slip assumption can not be made, the following characterization of the transformed accelerations is shown. The

acceleration in the planar North and East directions when the vehicle experiences side-slip can be derived from body frame inertial measurements ${a_x}'$ and ${a_y}'$. The navigation frame accelerations are related to the measurements by the following relationships.

$$a_{NORTH} = {a_x}' \cos\psi - {a_y}' \sin\psi \tag{4.54}$$

$$a_{EAST} = {a_x}' \sin\psi + {a_y}' \cos\psi \tag{4.55}$$

Where, as in the no-slip case, the the yaw angle of the vehicle can be derived by Euler integration of the g_z measurement.

$$\psi_k \quad = \quad \Delta t \sum_{i=0}^{k-1} g_z + \psi_0 \tag{4.56}$$

As the inertial measurements include a true acceleration, a, and a stochastic error component, ϵ_a, the expressions are expanded as

$$a_{NORTH} = (a_x + \epsilon_{a_x}) \cos\psi - \left(a_y + \epsilon_{a_y}\right) \sin\psi \tag{4.57}$$

$$a_{EAST} = (a_x + \epsilon_{a_x}) \sin\psi + \left(a_y + \epsilon_{a_y}\right) \cos\psi \tag{4.58}$$

Using the definition for the Euler-integrated yaw rate (Equation (4.9)) and Euler-integrated gyro error (Equation (4.10)) the expression becomes

$$a_{NORTH} = (a_x + \epsilon_{a_x}) \cos(\alpha + \beta) - \left(a_y + \epsilon_{a_y}\right) \sin(\alpha + \beta) \tag{4.59}$$

$$a_{EAST} = (a_x + \epsilon_{a_x}) \sin(\alpha + \beta) + \left(a_y + \epsilon_{a_y}\right) \cos(\alpha + \beta) \tag{4.60}$$

As in the no-slip velocity derivation, the trigonometric factors can be expanded by using the same identities and small-angle approximation. These operations give

$$a_{NORTH} = a'_x \cos(\alpha) - a'_x \sin(\alpha)\beta - a'_y \sin(\alpha) - a'_y \cos(\alpha)\beta \tag{4.61}$$

$$a_{EAST} = a'_x \sin(\alpha) - a'_x \cos(\alpha)\beta + a'_y \cos(\alpha) - a'_y \sin(\alpha)\beta \tag{4.62}$$

In order to calculate the variance of the north velocity, the simplified expression is first squared

$$\begin{aligned} {a_{NORTH}}^2 &= \left(a'_x \cos(\alpha) - a'_x \sin(\alpha)\beta - a'_y \sin(\alpha) - a'_y \cos(\alpha)\beta\right)^2 \\ &= {a'_x}^2 \cos^2(\alpha) + {a'_x}^2 \sin^2(\alpha)\beta^2 + {a'_y}^2 \sin^2(\alpha) + {a'_y}^2 \cos^2(\alpha)\beta^2 - \\ &\quad 2{a'_x}^2 \cos(\alpha)\sin(\alpha)\beta + 2a'_x a'_y \cos(\alpha)\sin(\alpha) + \\ &\quad 2a'_x a'_y \cos^2(\alpha)\beta + 2a'_x a'_y \sin^2(\alpha)\beta + \\ &\quad 2a'_x a'_y \cos(\alpha)\sin(\alpha)\beta^2 + 2{a'_y}^2 \cos(\alpha)\sin(\alpha)\beta \end{aligned} \tag{4.63}$$

Anticipating the expectation operator, the cross terms are removed from the expression as the error sources are independent and zero-mean. The accelerometer errors, ϵ_a are substituted and the expectation is applied to the resulting expression.

$$\begin{aligned} \mathrm{E}\left[{a_{NORTH}}^2\right] &= {a_x}^2 \cos^2(\alpha) + {a_x}^2 \sin^2(\alpha)\mathrm{E}\left[\beta^2\right] + {a_y}^2 \sin^2(\alpha) + {a_y}^2 \cos^2(\alpha)\mathrm{E}\left[\beta^2\right] + \\ &\quad \mathrm{E}\left[{\epsilon_{a_x}}^2\right]\cos^2(\alpha) + \mathrm{E}\left[{\epsilon_{a_x}}^2\right]\sin^2(\alpha)\mathrm{E}\left[\beta^2\right] + \\ &\quad \mathrm{E}\left[{\epsilon_{a_y}}^2\right]\sin^2(\alpha) + \mathrm{E}\left[{\epsilon_{a_y}}^2\right]\cos^2(\alpha)\mathrm{E}\left[\beta^2\right] + \end{aligned} \tag{4.64}$$

Subtracting the mean squared value yields the variance of the acceleration in the North direction.

$$\begin{aligned} \mathrm{E}\left[{a_{NORTH}}^2\right] &= {a_x}^2 \sin^2(\alpha)\mathrm{E}\left[\beta^2\right] + {a_y}^2 \cos^2(\alpha)\mathrm{E}\left[\beta^2\right] + \\ & \cos^2(\alpha)\mathrm{E}\left[{\epsilon_{a_x}}^2\right] + \sin^2(\alpha)\mathrm{E}\left[{\epsilon_{a_x}}^2\right]\mathrm{E}\left[\beta^2\right] + \\ & \sin^2(\alpha)\mathrm{E}\left[{\epsilon_{a_y}}^2\right] + \cos^2(\alpha)\mathrm{E}\left[{\epsilon_{a_y}}^2\right]\mathrm{E}\left[\beta^2\right] + \end{aligned} \tag{4.65}$$

The results from Chapter 3 can be substituted to yield the final variance of the North acceleration as resulting from the transformation of the acceleration measurements.

$$\begin{aligned} \mathrm{VAR}\left[{a_{NORTH}}^2\right] &= \left({a_x}^2 \sin^2(\hat{\psi}) + {a_y}^2 \cos^2(\hat{\psi})\right){\sigma_{\int \epsilon_{g_z}}}^2 + \\ & \cos^2(\hat{\psi}){\sigma_{\epsilon_{a_x}}}^2 + \sin^2(\hat{\psi}){\sigma_{\epsilon_{a_x}}}^2{\sigma_{\int \epsilon_{g_z}}}^2 + \\ & \sin^2(\hat{\psi}){\sigma_{\epsilon_{a_y}}}^2 + \cos^2(\hat{\psi}){\sigma_{\epsilon_{a_y}}}^2{\sigma_{\int \epsilon_{g_z}}}^2 \end{aligned} \tag{4.66}$$

Using the same procedure as above, the variance of the east acceleration reduces to the following expression

$$\begin{aligned} \mathrm{VAR}\left[{a_{EAST}}^2\right] &= \left({a_x}^2 \cos^2(\hat{\psi}) + {a_y}^2 \sin^2(\hat{\psi})\right){\sigma_{\int \epsilon_{g_z}}}^2 + \\ & \sin^2(\hat{\psi}){\sigma_{\epsilon_{a_x}}}^2 + \cos^2(\hat{\psi}){\sigma_{\epsilon_{a_x}}}^2{\sigma_{\int \epsilon_{g_z}}}^2 + \\ & \cos^2(\hat{\psi}){\sigma_{\epsilon_{a_y}}}^2 + \sin^2(\hat{\psi}){\sigma_{\epsilon_{a_y}}}^2{\sigma_{\int \epsilon_{g_z}}}^2 \end{aligned} \tag{4.67}$$

Where $\hat{\psi}$ is the integrated gyro measurement.

In the resulting variance expressions for the slip case accelerations, ${\sigma_{\epsilon_{a_x}}}^2$ and ${\sigma_{\epsilon_{a_y}}}^2$ are simply the output variances of the accelerometers. While these values are bounded

in time, the integrated gyro variance $\sigma_{\int \epsilon_{g_z}}{}^2$ is not. This unbounded acceleration error causes an even faster error growth in the integrated velocity and double-integrated position values. For the no-slip case, no such acceleration transformation is necessary. Consequently, the no-slip velocity and position error will grow at a slower rate than that for the slip case. This suggests that when such vehicle constraints are valid, better dead-reckoning performance is achieved when using the fewest possible measurements with the fewest possible integrations. The following sections seeks to support this claim with a simulation example.

4.5 Comparison of Slip and No-Slip Mechanizations

Since for the no-slip case, only a single accelerometer is required and no transformation is necessary, the velocity and position values derived with the simpler dynamic equations and therefore exhibit a slower error growth. The conclusion then is that if and only if the no-slip condition exists, better dead-reckoning performance can be achieved by using as few measurements as possible and few sensor integrations as possible. By using computer simulation tools, these claims are demonstrated as follows.

A comparison of the two methods can be realized with the use of a Monte Carlo simulation as used for the validation of the variance expressions earlier in this chapter. Within this particular simulation, a position trajectory is defined and the resultant vehicle orientation, velocities, and accelerations are computed under the no slip assumption. A Monte Carlo simulation is performed (3000 iterations) in which simulated inertial errors with assumed sensor error parameters are added to the inertial values of accelerations and rotation rates. The simulated inertial measurements are sent to two calculation routines: one in which the no-slip condition is assumed, the other in which the side-slip

assumption is assumed. For 3000 iterations, the variance of the velocity, position, and attitude for each time step is calculated and stored for comparison.

Figure 4.8 shows a sample North vs. East position trajectory defined in the navigation frame. Under the no-slip assumption, the 2-D velocity is computed and shown in Figure 4.9; the corresponding no-slip yaw angle is shown in Figure 4.10. Using the same sensor specifications as listed in Table 3.1 (with a faster sample rate of 100Hz), the inertial measurements are simulated and processed for both the no-slip case in Figure 4.4 and the slip case in Figure 4.3 for 2000 iterations. The variance functions of the yaw angle, 2-D velocity, and 2-D position are then computed for each case over the 3000 iterations.

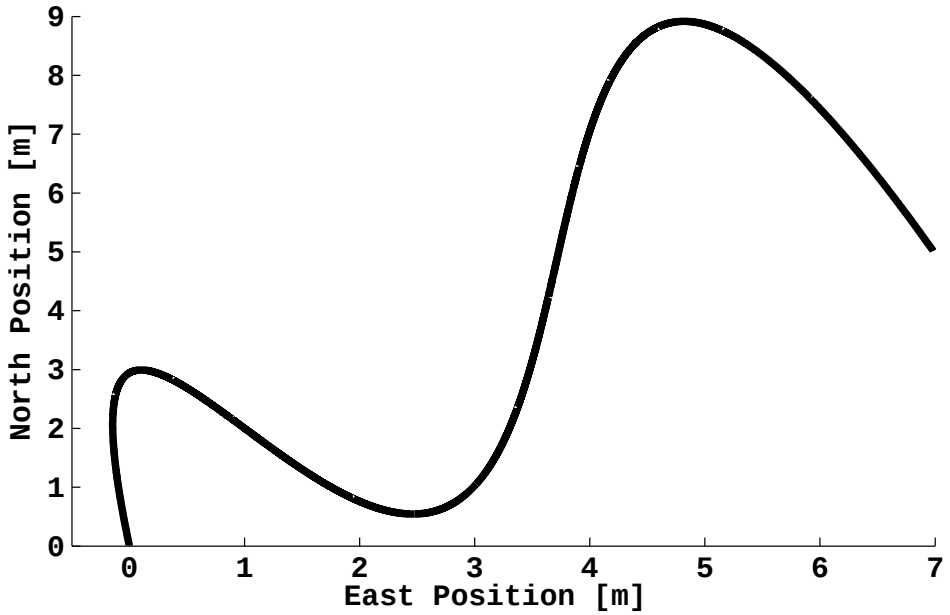

Figure 4.8: Defined Position Trajectory

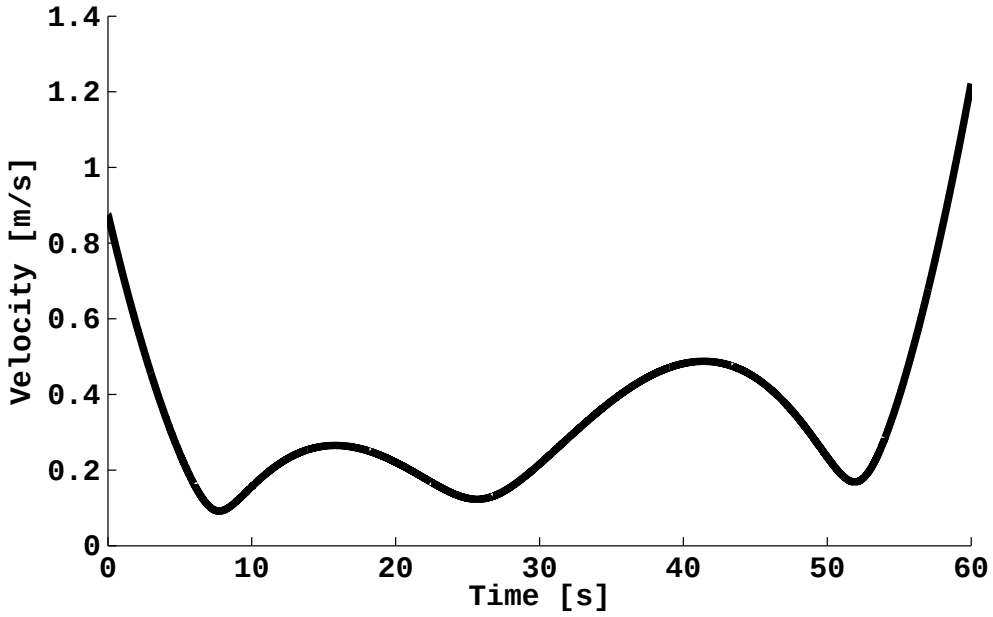

Figure 4.9: Velocity Trajectory With No Side Slip

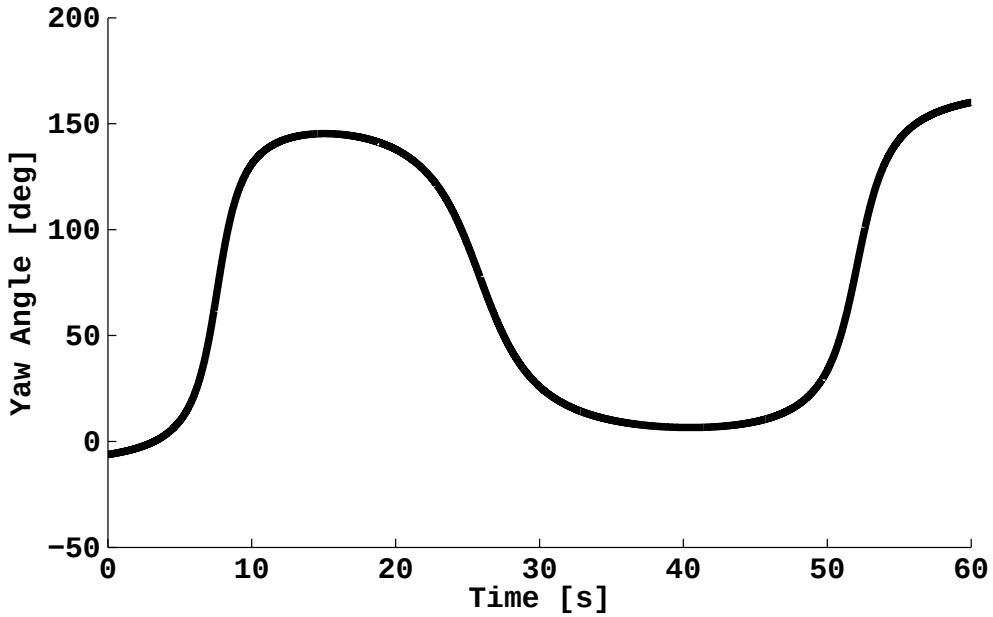

Figure 4.10: Yaw Angle Trajectory With No Side Slip

Figure 4.11 shows the 3-σ bounds for the yaw angle under each kinematic assumption. Since the processing is identical, the attitude of the body under each assumption exhibits identical variance growth curves. However, Figures 4.12 (Velocity) and 4.13 (Position) show a different result. Here, the growth in the integral states derived using the no-slip mechanization is slower than that using the slip mechanization thus exemplifying the effect claimed.

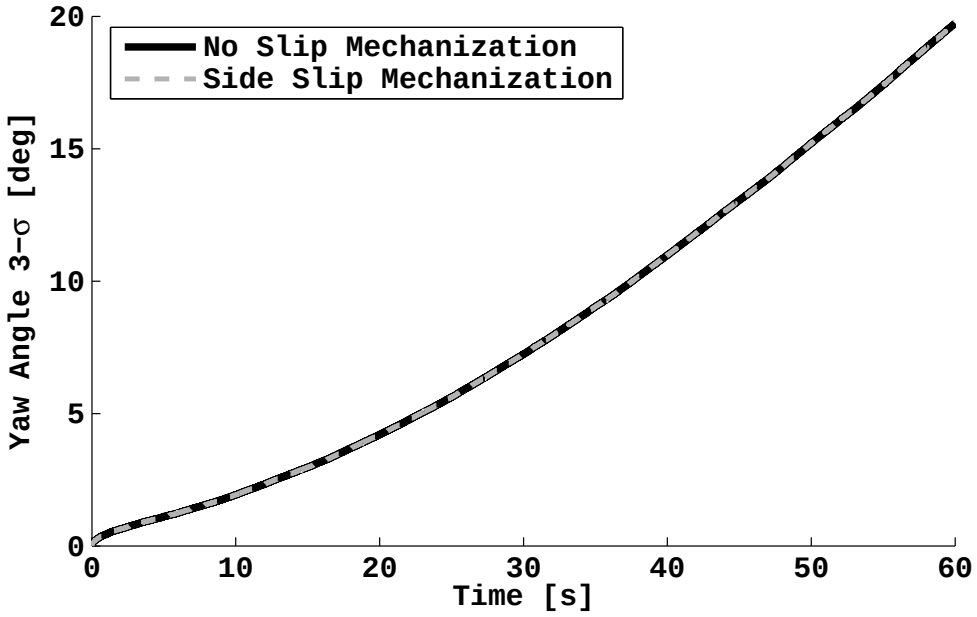

Figure 4.11: 3-σ Bounds on Simulated Yaw Angle

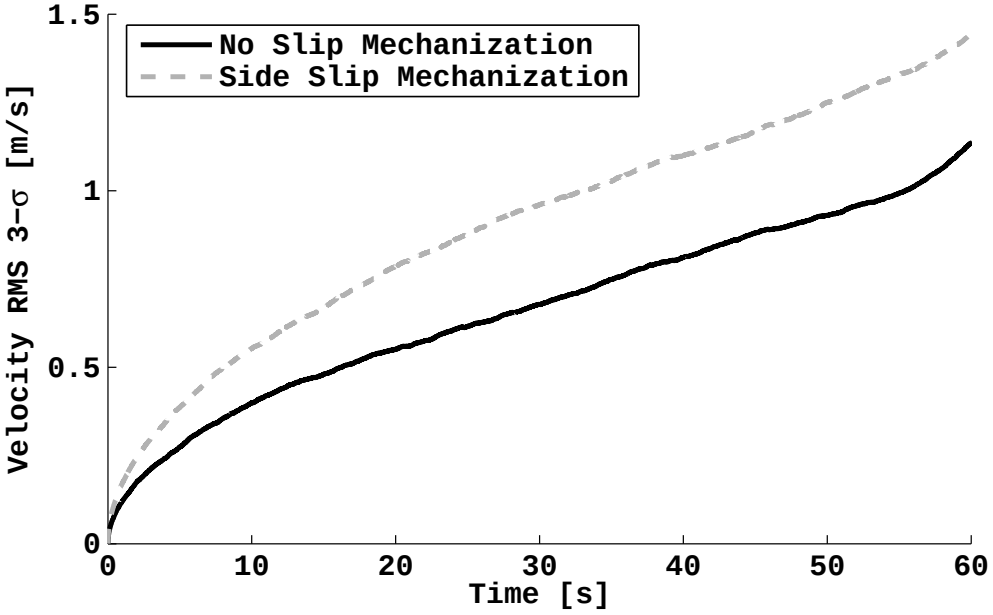

Figure 4.12: RMS 3-σ Bounds on Velocity

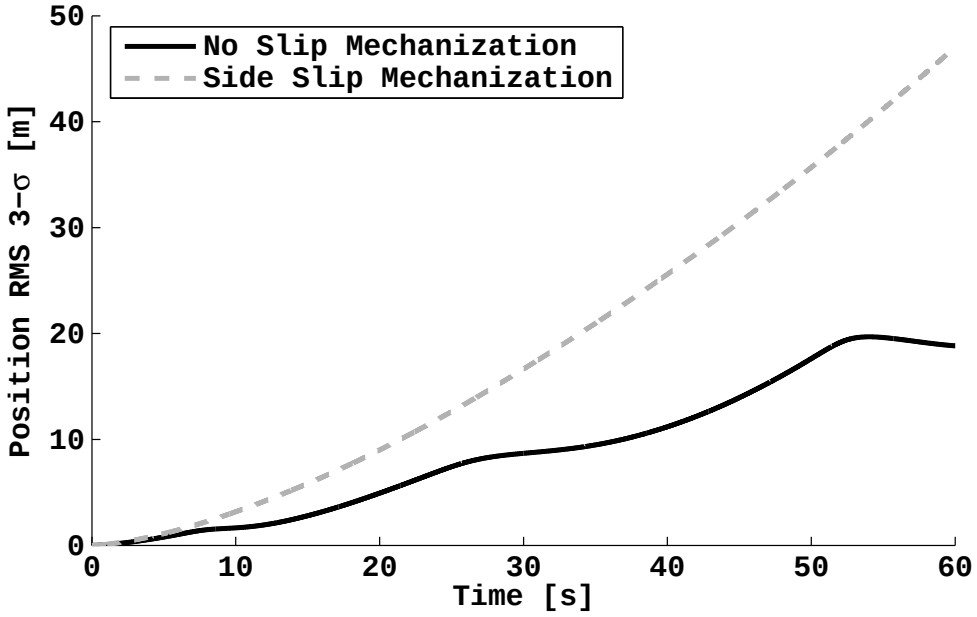

Figure 4.13: RMS 3-σ Bounds on Position

This example shows that when the no-slip assumption is valid, use of the no-slip dynamic equations results in more accurate dead-reckoning performance. In contrast, use of the side-slip equations result in a higher rate of error growth due to the unnecessary acceleration measurement and additional step of integration in the governing equations. It is emphasized again that the no-slip equations only provide a valid result when such a no-slip assumption can be made.

4.6 Conclusion

This chapter has presented an analysis of the propagation of the stochastic inertial sensor errors into the position, velocity, and attitude vehicle states for a body restricted to planar motion. For this planar case, it is shown that the vehicle's z axis is always aligned to the navigation frame ψ axis and therefore its errors are simply the integrated gyro errors. These integrated sensor errors can be quantified by direct application of the variance expressions derived in Chapter 3. Within this planar navigation scenario, two kinematic cases are studied: side-slip and no side-slip. For the no side-slip case, a vehicle's velocity vector is coincident with its heading, and velocity is ascertained from a single accelerometer integration. However, in the side-slip case the vehicle points away from its direction of travel and the velocity must be derived from an additional measurement and additional integration step. This chapter shows through analytical results and a simulation example that when a vehicle has no side-slip, better dead-reckoning accuracy is achieved by employing the simpler equations with fewer measurements for the no-slip mechanization, as compared to the added measurements of the side-slip mechanization. This chapter has also shown through the position derivation for the no-slip case, the difficulty in the current analysis approach. It is suggested that further analytical analysis

be performed using techniques which provide more comprehensive statistical information on the propagated inertial errors to analytically quantify the position errors in planar mechanization.

Chapter 5

Six DOF Analysis

5.1 Introduction

As mentioned in Chapter 4, six degrees of freedom (6-DOF) are required to kinematically describe the most general motion of a body in space. In modern-day inertial navigation these six degrees of freedom are typically measured with an inertial measurement unit (IMU) rigidly attached to the body. The IMU measures three orthogonal accelerations (a_x,a_y,a_z) and three orthogonal rotation rates (g_x,g_y,g_z) for a total of 6 degrees of freedom. For the purpose of navigation, such measurements need to be transformed into a coordinate system suitable for navigating. Figure 5.1 shows a common navigation-frame cartestian coordinate system as commonly employed on many inertial navigation systems, especially ground vehicles [25]. In one such cartesian frame, the navigating vehicle's state is described by its velocity, and position in terms of coordinates North, East, and Down (NED) and by its roll (ϕ), pitch (θ), and yaw (ψ) angles about the NED axes, respectively. The diagram from Chapter 4 is shown again in here in Figure 5.1 to illustrate the body and navigation frame axes.

This chapter presents the equations necessary to use body frame measurements from a 6-DOF IMU to describe a vehicle's state in the navigation frame. This 6-DOF navigation scheme is applicable to all of the scenarios introduced in the previous chapters as it captures the most general vehicle motion. As Chapters 3 and 4 have illustrated, the accuracy of any inertial navigation system degrades with time, sensor integrity, trajectory, and dynamic relationships employed without aid from external measurements. In

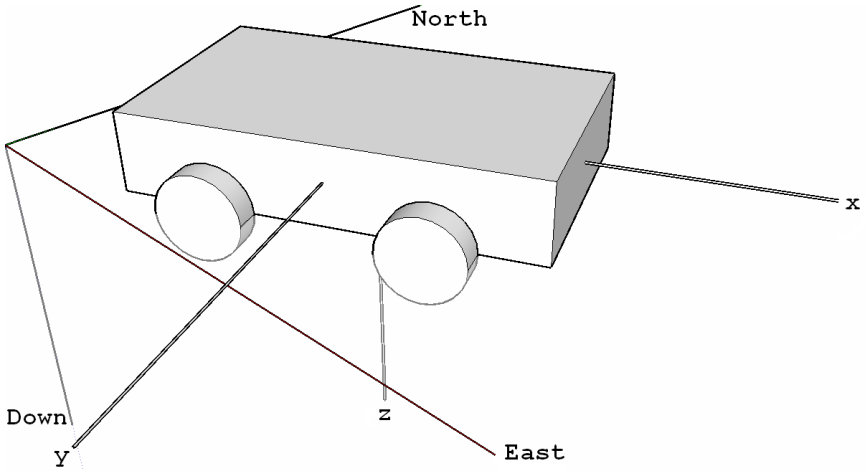

Figure 5.1: Simplified Coordinate Frame

specific regards to the effect of dynamic relationships, Chapter 4 showed a comparative example showing the relative decline in inertial navigation performance when unnecessary measurements and integrations are used in deriving the navigation-frame states. This chapter will extend this point with a similar example in which inertial navigation of a planar trajectory is compared using the planar equations of Chapter 4 and the general 6-DOF method presented in this chapter.

5.2 Equations of Motion

5.2.1 Orientation

Two common conventions are used to describe a body's orientation in the NED navigation frame: Euler angles and Quaternions. The Euler angle representation, while intuitive and straightforward to implement, exhibits a matrix singularity for pitch angles at 90 degrees. As this particular orientation is rarely encountered on many vehicles which use the NED frame, Euler angles remain as popular choice for ground vehicles. The

Quaternion approach involves a set of four linear differential equations which describe orientation in three dimensional space. The method has the advantage of being immune to any particular singularities and therefore is numerically stable for all orientations. However, as the quaternion values themselves lack strong physical meaning, they are commonly transformed from and to Euler angles using a nonlinear relationship. The advantage of the quaternion approach for ground vehicle applications therefore is mainly in numerical computation and the relative accuracy compared to the Eulerian angle method is negligible. A more complete comparison and discussion of the two methods can be found in [26]. For the simple study in this thesis, the Euler angle representation is presented as follows.

The Eulerian angular velocities are described in terms of the body frame rotation rates by the following set of first order differential equations

$$\begin{bmatrix} \dot{\phi} \\ \dot{\theta} \\ \dot{\psi} \end{bmatrix} = \frac{1}{\cos\theta} \begin{bmatrix} \cos\theta & \sin\phi\sin\theta & \cos\phi\sin\theta \\ 0 & \cos\phi\cos\theta & -\sin\phi\cos\theta \\ 0 & \sin\phi & \cos\phi \end{bmatrix} \begin{bmatrix} g_x \\ g_y \\ g_z \end{bmatrix} \tag{5.1}$$

where g_x, g_y, and g_z are the rotation rates as aligned to orthogonal axes on the body and (ϕ), (θ), and (ψ) are the rotation rates about the navigation frame axes. The nonlinear relationships of orientation given by Equations (5.1) are numerically integrated to obtain the resulting Euler angles describing the attitude of the navigating body in space.

It is instructive to note that when two angles are zero, the angular rate corresponding to the remaining angle holds a one-to-one relationship from the body frame to the navigation frame. Additionally, if the body frame rotation rates g_x and g_y are zero then

the relationship between the navigation-frame yaw rate, ψ, and body-frame rate g_z exhibit a one-to-one relationship. The latter situation is precisely the planar case studied in Chapter 3 in which the orientation of the body was constrained to rotate only about its z-axis.

5.2.2 Translation

The accelerations as measured in the body-frame, must be transformed into the navigation frame using the Euler angles obtained from the orientation calculations. The Euler angles are used to construct the direction-cosine rotation matrix [26], which simply re-orients the three accelerations as measured in the body frame, to the navigation frame North, East, Down directions. The relationships between body frame and navigation frame accelerations are shown by Equation (5.2).

$$\begin{bmatrix} a_N \\ a_E \\ a_D \end{bmatrix} = \begin{bmatrix} \cos\theta\cos\psi & -\cos\phi\sin\psi + \sin\phi\sin\theta\cos\psi & \sin\phi\sin\psi + \cos\phi\sin\theta\cos\psi \\ \cos\theta\sin\psi & \cos\phi\cos\psi + \sin\phi\sin\theta\sin\psi & \sin\phi\cos\psi + \cos\phi\sin\theta\sin\psi \\ -\sin\theta & \sin\phi\cos\theta & \cos\phi\cos\theta \end{bmatrix} \begin{bmatrix} a_x \\ a_y \\ a_z \end{bmatrix} \quad (5.2)$$

Once the accelerations are transformed, the gravity component is subtracted from the down acceleration to yield the kinematic acceleration of the body in the navigation frame. The resulting velocity and positions as described by the North, East, Down coordinate system are then derived by direct integration of the transformed accelerations.

This process in which the IMU outputs are transformed and integrated into usable navigational quantities is known as mechanization. The mechanized IMU rigidly attached to the navigating body is considered the Inertial Navigation System (INS). The 6-DOF IMU mechanization algorithm as introduced above is summarized by Figure 5.2.

The simple mechanization shown here neglects the coriolis, centripetal accelerations, and other effects experienced by an IMU moving on the rotating earth. For the short range (short time) for which many ground vehicles travel, these effects are small and the mechanization discussed here is sufficient to support the typical requirements.

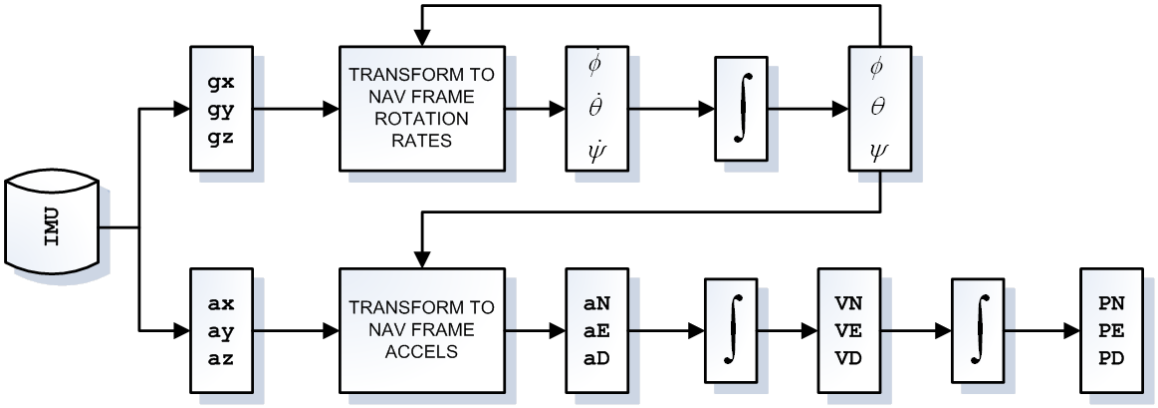

Figure 5.2: Mechanization of IMU Measurements

See Appendix B for a demonstration of the mechanization equations as presented. This appendix presents the mechanization of a medium grade IMU 6-DOF and compares its performance to position and velocity from a high-accuracy differential GPS receiver.

5.3 Comparison to Planar Mechanization

In Chapter 4 it was shown that for a planar vehicle trajectory where the body experiences no side-slip, the position and velocity error growth using the assumed-slip planar mechanization exhibited a faster variance growth than results from the no-slip planar method. The faster error growth observed with the slip equations was due to two contributing factors. The slip case required both an acceleration measurement and an additional step of numerical integration in the computation of its velocity and position

values. The 6-DOF navigation equations presented above are a natural extension of the 2-D slip case to the 6-DOF system. When the planar assumption can be made, using the 6-DOF equations will add unnecessary error into the system. As a result, the error growth for the 6-DOF case will be much worse. In the following, an example is shown using the same trajectory of Chapter 4 to show the amount of additional error induced when the 6-DOF method is employed.

Figures 5.3 5.4 and 5.5 show a sample position, velocity, and yaw angle trajectory. Like the identical trajectory of the chapter 4 slip/no-slip comparison, the velocity, and yaw angle are derived from the defined position trajectory.

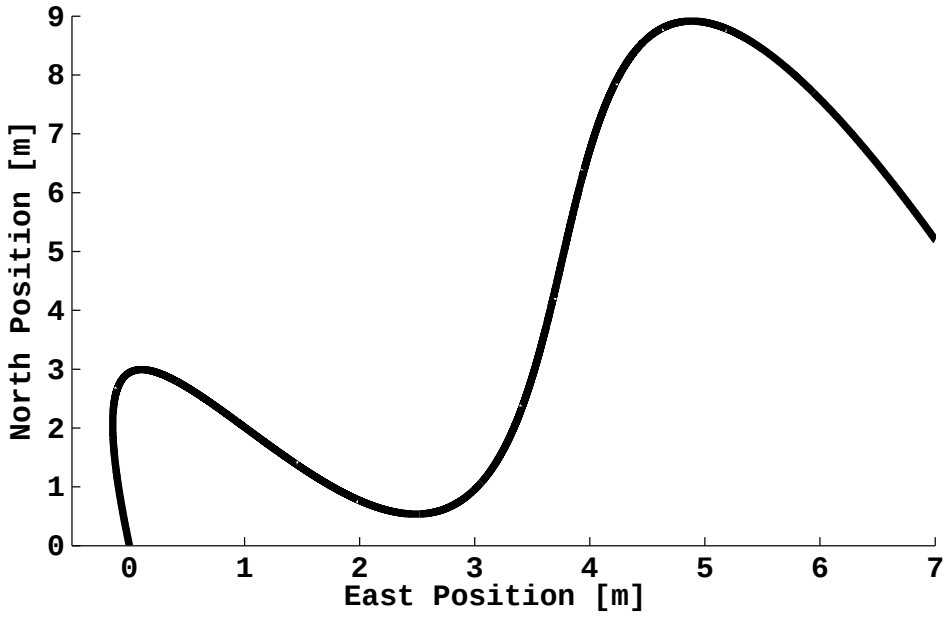

Figure 5.3: Defined Position Trajectory

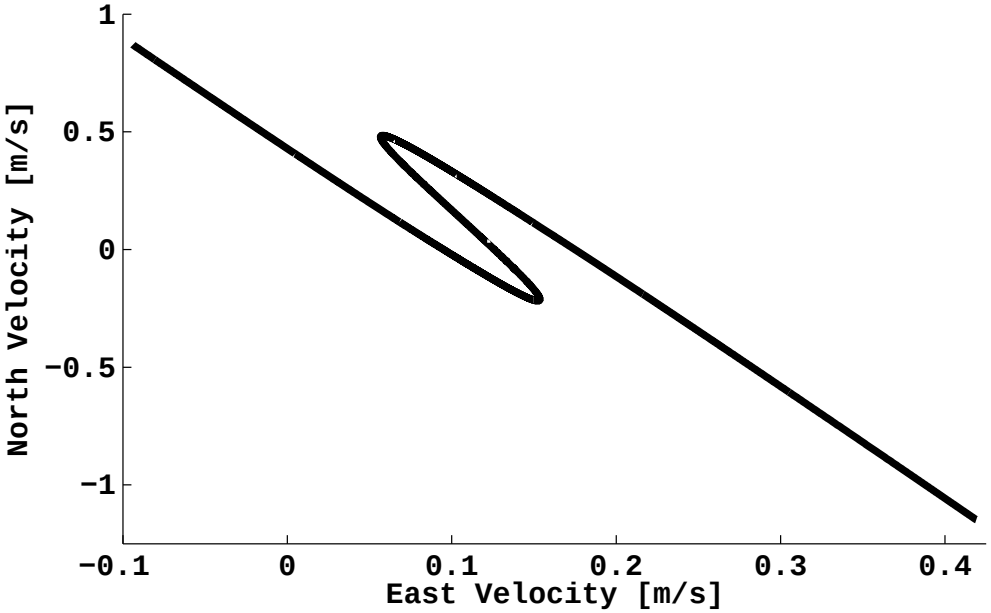

Figure 5.4: Velocity Trajectory for Planar Motion

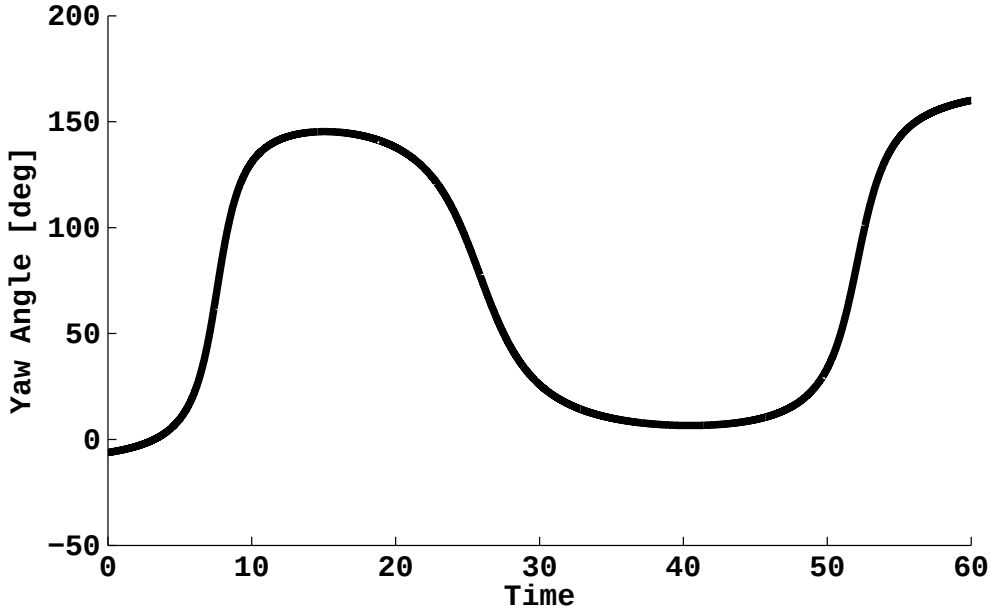

Figure 5.5: Yaw Angle Trajectory for Planar Motion

Using the sensor specifications as shown in Table 5.1, a Monte Carlo simulation was performed by computing 6-DOF position, velocity, and attitude with simulated acceleration measurements, a_x, a_y, a_z and rotation rates g_x, g_y, g_z. Another Monte Carlo simulation was then performed with the planar side-slip equations of Chapter 4 using simulated a_x, a_y and g_z with the same sensor specifications. Both simulations in this example were performed with 1200 iterations. The resulting standard deviations of the two dimensional rms velocity, rms position and the attitude angle are then plotted for comparison.

Table 5.1: Simulated Sensor Specifications (Comperable to Crossbow IMU-400C)

Gyro Spec	Value	Accel Spec	Value
f_s	100 Hz	f_s	100 Hz
σ_{rw}^2	0.14948 deg/s/sqrt(Hz)	σ_{rw}^2	0.000412 g/sqrt(Hz)
σ_b^2	0.61183 deg/s	σ_b^2	0.000100 g
τ	1300 seconds	τ	500 seconds

Figure 5.6 compares the standard deviation results for the yaw angle computed with the planar equations and then with the 6-DOF equations. It is evident that the error in the yaw angle for this trajectory is approximately the same. As the 6-DOF equations "take out" the effect of the roll and pitch angles on the yaw angle, the yaw orientation is the same.

Figures 5.7 and 5.8 compare the standard deviation results for the 2-D rms velocity and 2-D rms position, respectively. It is clear from these two plots that the additional measurements in the 6-DOF scheme cause a much more severe error growth as contrasted to the 3-DOF case.

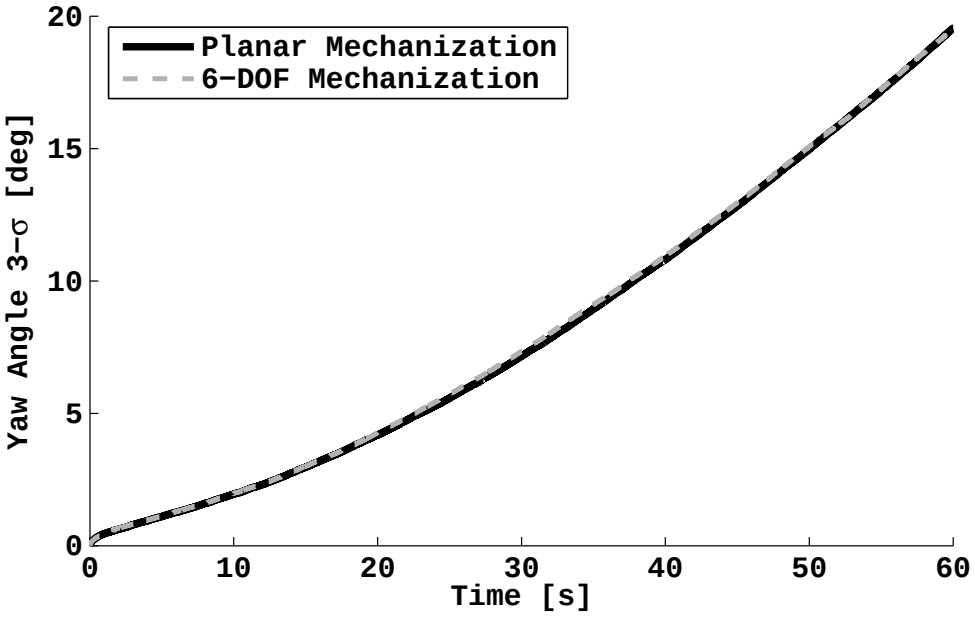

Figure 5.6: 3-σ Bounds on Yaw Angle Mechanization Comparison

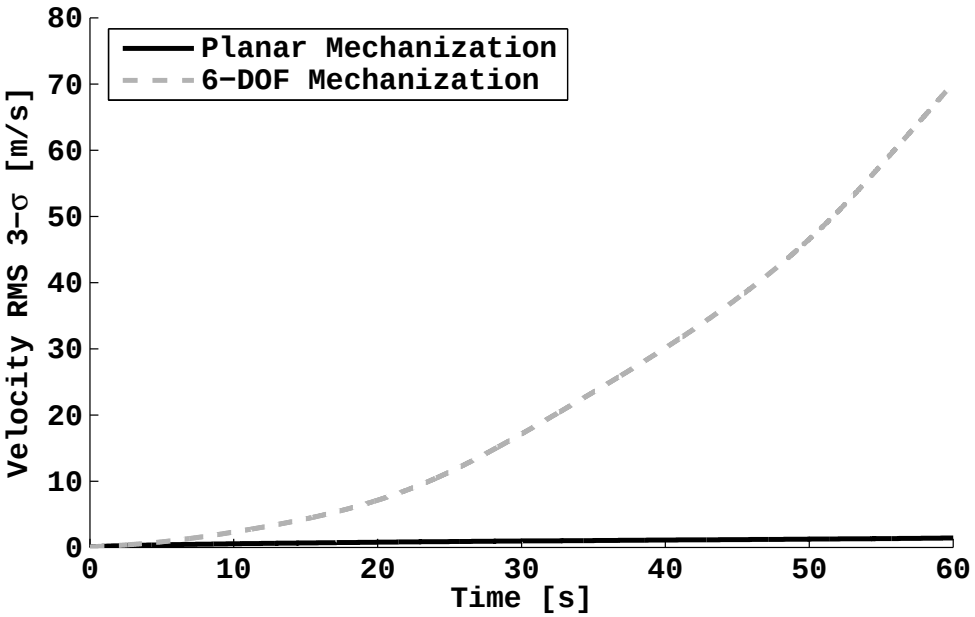

Figure 5.7: RMS 3-σ Bounds on Velocity Mechanization Comparison

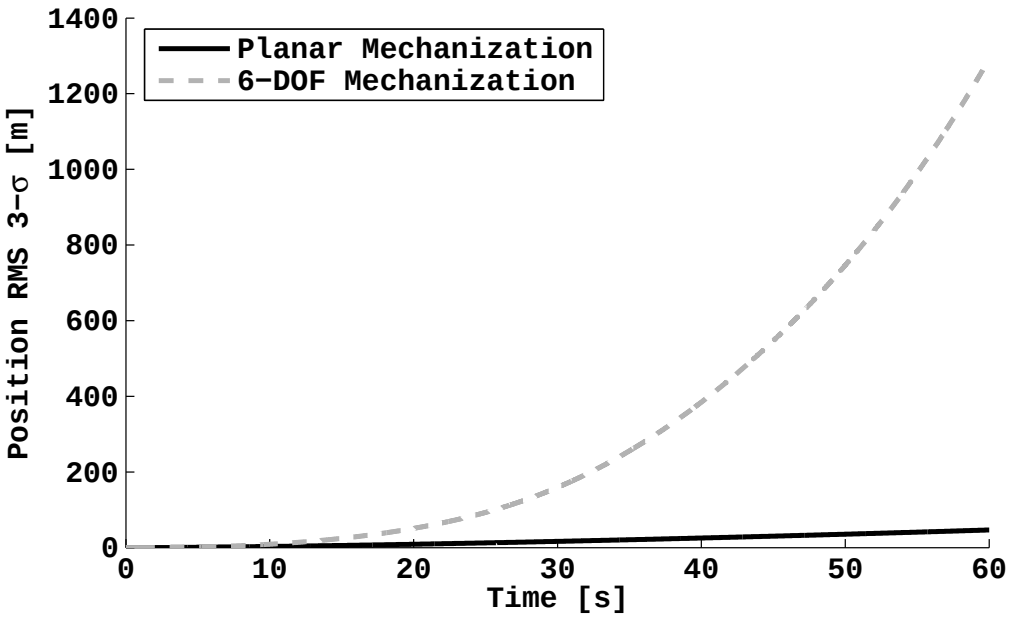

Figure 5.8: RMS 3-σ Bounds on Position Mechanization Comparison

Figure 5.9 and 5.10 show the standard deviation results for pitch and roll angles, respectively. These plots show precisely why the position and velocity growth is so large: the integrated stochastic errors on the additional roll and pitch measurements cause the accelerations to be rotated to an incorrect orientation. As a result, the mis-oriented accelerations are integrated along their incorrect directions to give a much more inaccurate North/East velocity and position.

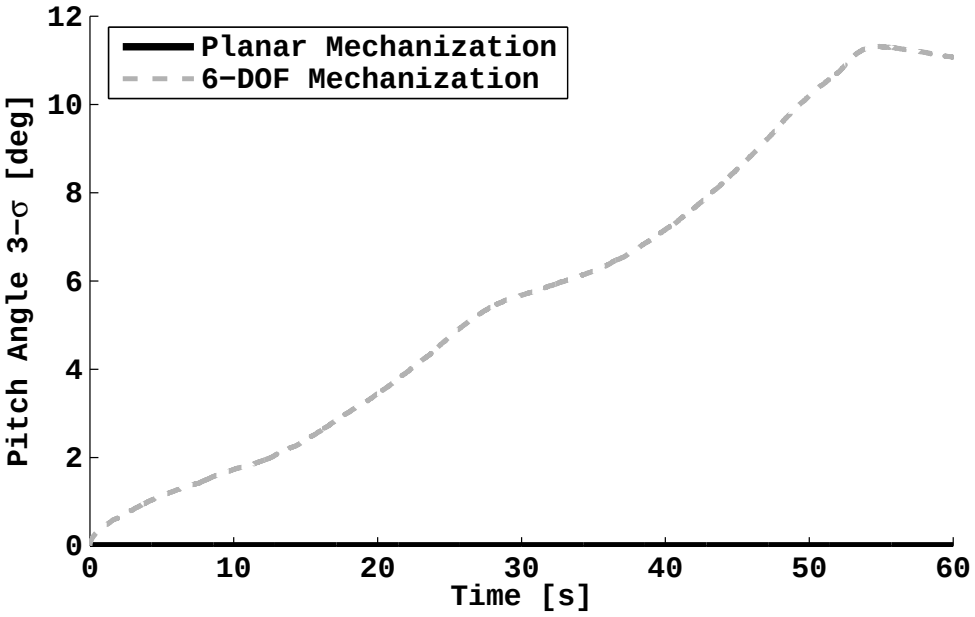

Figure 5.9: 3-σ Bounds on Pitch Angle DOF Comparison

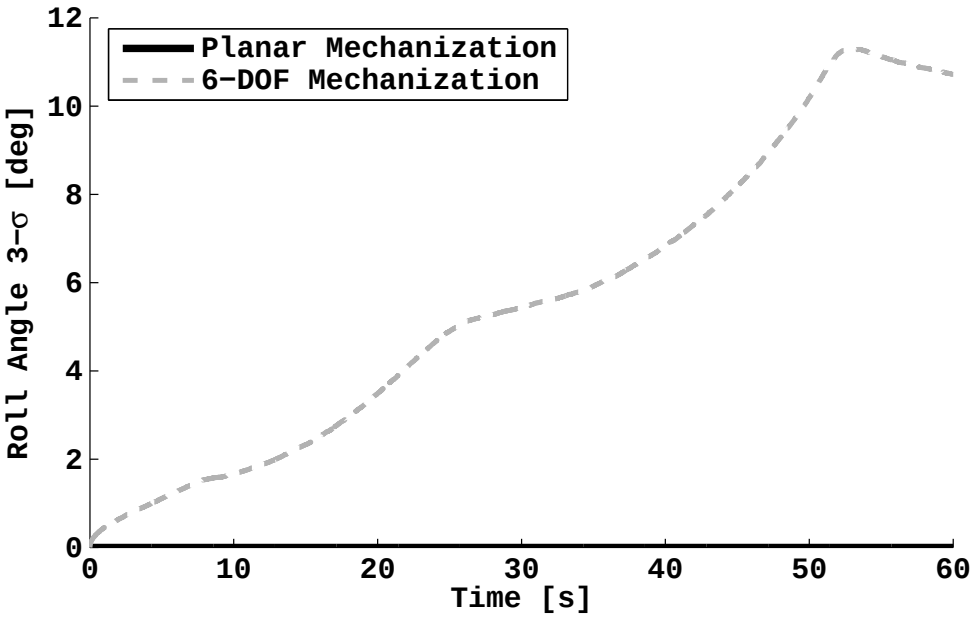

Figure 5.10: 3-σ Bounds on Roll Angle DOF Comparison

In the example above, it is clear that the body constrained to travel on the flat plane not only lacked the benefit of the extra gyro measurements - they greatly increased the overall error in the desired states. While this sample simulation has demonstrated the effect of unnecessary inertial measurements in dead-reckoning navigation, it should be re-iterated that if the body was indeed traveling in motion that required a 6-DOF characterization, no less than six inertial measurements can be employed to correctly compute the vehicle's trajectory. In other words, better navigation performance will most likely not be achieved by employing kinematic relationships which are simpler than the motion of the navigating body. In conclusion, when a vehicle in motion is under kinematic constraints, few measurements and integrations as required to completely describe the vehicle will yield the smallest amount of error.

Chapter 6

Conclusions

6.1 Overall Contributions

This thesis has presented an analysis of the expected accuracy of inertial dead-reckoning in a variety of navigation scenarios. First, stochastic models were proposed as approximations to the observed behavior of many common types and grades of accelerometers and rate gyros. The selected inertial sensor error model included the sum of two independent Gaussian processes characterized by three parameters. Parameter identification methods of Allan variance and experimental autocorrelation were presented as the means of extracting the model parameters from experimental data. Derivations of the variance of subsequent integrations of each sensor error component process were performed and validated using Monte Carlo simulations. An application of the integrated error source variance expressions were demonstrated for the single-axis navigation scenario in which a single accelerometer or single gyro is used to ascertain integral navigation states in its fixed direction. The single-axis results were then expanded to derive expressions for the propagation of the inertial sensor error into the mechanization equations used for planar navigation in which a traveling body experiences no side-slip. The results of the no-slip position were discussed and shown to have limitations due to the analysis techniques used. The planar no-slip inertial navigation mechanization was then compared to the planar mechanization with slip for the purpose of showing the errors induced by additional integrations and measurements required of the slip mechanization. The final chapter concluded the quantification of inertial navigation by presenting the

6-DOF kinematic relationships as applied in the navigation of a body unconstrained in three dimensional space. The concluding point of Chapter 4 was reiterated again with a simulation example illustrating the additional dead-reckoning error induced by employing unnecessary additional integrations and measurements in the 6-DOF equations for a simple planar trajectory.

In summary, this research has provided

1. Approximate stochastic models which capture the necessary behavior of accelerometer and rate-gyroscope outputs as measured from various grade inertial measurement units.

2. Derivations of the variance of the numerically integrated values of the inertial sensor error sources of wide-band noise and exponentially correlated noise (Gauss-Markov process) from the error models.

3. Derivations of the variance of the 2-D (North/East) velocity error for a planar navigation scenario in which a vehicle experiences no side-slip. The position derivation is performed to show the need for methods of analysis superior to that of this thesis.

4. Comparison of the no-slip and slip and general 6-DOF inertial navigation equations for the planar case.

5. The six degree of freedom equations used for the most general navigation scenario.

In addition to the derivations, this thesis has demonstrated the claim that the fewest number of integrations and measurements required to provide valid vehicle states in an inertial navigation system yields the minimal amount of error. It was shown through a simulation comparison of the planar no-slip, planar slip, and 6-DOF general

motion methods, that the inertial navigation with the simplest system had the best dead-reckoning performance (when the real vehicle trajectory was described by the simplest set of equations).

6.2 Difficulties

The quantity and nature of approximations presented in this thesis warrant a discussion of the limitations of the contributing results. It should first be noted that the variance expressions for the integrated sensor errors in Chapter 3 are derived based on the assumption that inertial sensors can be modeled with the approximations in Chapter 2. The experimental identification and validation of of simple models with real experimental data is a difficult process due to the extremely large amount of data required and the inadequacy of the assumed model forms. Based on these difficulties, the accuracy of the variance expressions based on the assumed model form should only reflect the accuracy of the experimental identification techniques by employing conservative parameter estimates.

The techniques used to ascertain the variance of the integrated inertial sensor errors in Chapter 3 proved useful in its straightforward and intuitive approach. However, as shown for the planar no-slip position variance derivation in Chapter 4, the autocorrelation information was needed to simplify the expression to closed-form. The straightforward method of derivation in Chapter 3, while yielding the desired variance expressions, did not allow for simple identification of higher order measures of statistics. Additional information such as the cross-correlation and autocorrelation are difficult to attain with the techniques employed in this thesis. In conclusion, other techniques are suggested for

use in quantifying the propagation of stochastic errors through various transformations and integration.

In Chapter 3, the variance of the integral values of the Gauss-Markov process assumes that the process is realized with a zero-initial condition at the onset of integration. This zero initial condition for some values of the Markov model parameters may not accurately reflect the desired nature of the process as it may exhibit some initial transients in reaching its stationary status.

The developed expressions in Chapter 4 for the variance of the planar case errors were based on small angle linear approximations for trigonometric operations on the integrated gyro error. For errors outside the range for which the approximations are valid, the error will propagate non-linearly and the resulting value will no longer be a Gaussian variable. The variance expression will then be inadequate to fully characterize the error of the nonlinearly processed inertial errors. However, the size of integrated gyro errors necessary to break the linear approximation is well outside the range for which a system designer is interested. Therefore the approximation is rarely an issue for the use of the variance expressions as practical analysis tools.

6.3 Future Work

In order to more fully and successfully characterize the stochastic outputs of acceleration and rotation rate outputs of many grade IMUs, it is suggested that much experimental data be taken and studied to ensure the feasibility of the approximations introduced in this thesis. As the stochastic models introduced in Chapter 2 do not include terms for temperature or range of motion, a study of such effects should be done to ensure that their influence is negligible. Given that the stochastic models from Chapter 2

are sufficient to match the behavior of the sensor errors, their corresponding parameters should be identified with higher confidence using appropriately the techniques of Allan variance and autocorrelation. Once the models are validated and parameters identified, the resulting variance expressions in Chapters 3 and 4 should be tested with experimental data to verify their use in real inertial navigation scenarios.

As discussed above, the methodology used to propagate the sensor errors has room for improvement. Other more comprehensive statistical analysis techniques may provide a better and more complete characterization of the inertial system errors and performance in dead-reckoning. Since the inertial navigation performance using the 6-DOF mechanization scheme depends highly on non-linear relationships, the Gaussian sensor errors do not propagate linearly into the velocity, position, and orientation states and thus exhibit non-Normal distributions. More complete probabilistic characterizations of the propagation of sensor errors into the applicable nonlinear equations may provide broader results to the navigation systems mechanized for general motion.

Using validated stochastic models and improved methods of error propagation analysis, future research may expand its scope to include analyses of dead-reckoning with inertial measurements in a larger range of scenarios. As other sensors such as odometry, laser scanners, and vision, are continually being fused into the navigation system, knowledge of the dead-reckoning performance of these systems becomes increasingly desirable. In addition, more sophisticated GPS/INS algorithms such as Tightly-Coupled GPS/INS allow for dead-reckoning aid from any available satellites when the number visible are less than that required for a position fix. Firm quantification of the increased performance from any type of vehicle constraint, GPS, or auxiliary sensors in the large

range of applicable mechanizations provides much valuable information to the navigation community at large.

Bibliography

[1] R. E. Kalman, "A new approach to linear filtering and prediction problems," *ASME: Journal of Basic Engineering*, vol. 82, pp. 34–45, 1960.

[2] M. Newlin, "Design and development of a gps intermediate frequency and imu data acquisition system for advanced integrated architectures," Master's thesis, Auburn University, December 2006.

[3] J. M. Clanton, D. M. Bevly, and A. S. Hodel, "Highway lane tracking using gps in conjunction with onboard imu and vision-based lane tracking measurements." Fort Worth, TX: Institute of Navigation: ION-GNSS Conference, September 2006.

[4] M. M. Veth and J. Raquet, "Fusion of low-cost imaging and inertial sensors for navigation." Fort Worth, TX: Institute of Navigation: ION-GNSS Conference, September 2006.

[5] C. R. Carlson, "Estimation with applications for automobile dead reckoning and control," Ph.D. dissertation, Stanford University, April 2004.

[6] W. Travis, A. T. Simmons, and D. M. Bevly, "Corridor navigation with a lidar/ins kalman filter solution." Las Vegas, Nevada: IEEE Intelligent Vehicle Conference, 2005.

[7] S. Nassar, "Improving the inertial navigation system (ins) error model for ins and ins/dgps applications," Ph.D. dissertation, University of Calgary, November 2003.

[8] S. Godha and M. E. Cannon, "Integration of dgps with a low cost mems-based inertial measurement unit (imu) for land vehicle navigation application." Long Beach, CA: Institute of Navigation GNSS, September 2005.

[9] M. M. Tehrani, "Ring laser gyro data analysis with cluster sampling technique," vol. 412. SPIE: International Society for Optical Engineering, 1983, pp. 207–220.

[10] H. Hou and N. El-Sheimy, "Inertial sensors errors modeling using allan variance." Portland, OR: Institute of Navigation GNSS, September 2003.

[11] D. Gebre-Egziabher, "Design and performance analysis of a low-cost aided dead reckoning navigator," Ph.D. dissertation, Stanford, 2004.

[12] H. Kim, J. G. Lee, and C. G. Park, "Performance improvement of gps/ins integrated system using allan variance analysis." Sydney, Australia: Internation Symposium on GNSS/GPS, December 2004.

[13] B. E. Grantham and M. A. Bailey, "A least-squares normalized error regression algorithm with application to the allan variance noise analysis method." Coronado, CA: Institute of Navigation: Position Location and Navigation Symposium, April 2006.

[14] W. Flenniken, "Modeling inertial measurement units and analyzing the effect of their errors in navigation applications," Master's thesis, Auburn University, December 2005.

[15] D. Bevly, "High speed, dead reckoning, and towed implement control for automatically steered farm tractors using gps," Ph.D. dissertation, Stanford University, August 2001.

[16] A. Gelb, *Applied Optimal Estimation*, A. Gelb, Ed. M.I.T. Press, 1974.

[17] S. J. Pethel, "Test and evaluation of high performance micro electro-mechanical system based inertial measurement units." Coronado, CA: Institute of Navigation: Position Location and Navigation Symposium, April 2006.

[18] J. Rankin, "Gps and differential gps: An error model for sensor simulation." IEEE, 1994.

[19] K. J. Astrom and B. Wittenmark, *Computer Controller Systems*, 2nd ed. Prentice Hall, 1990.

[20] K. Breitfelder, "Ieee standard specification format guide and test procedure for single-axis laser gyros," IEEE Aerospace and Electronic Systems Society, Tech. Rep., September 1995.

[21] D. W. Allan, "Statistics of atomic frequency standards," vol. 54, no. 2. IEEE, February 1966.

[22] L. C. Ng, "On the application of allan variance method for ring laser gyro performance characterization," Lawrence Livermore National Laboratory," Informal Report, October 1993.

[23] R. G. Brown and P. Y. C. Hwang, *Introduction to Random Signals and Applied Kalman Filtering*, 3rd ed. Wiley, 1997.

[24] W. Stockwell, "Bias stability measurement: Allan variance," Crossbow Technology, Inc., Tech. Rep.

[25] T. N. Gillespie, *Fundamentals of Vehicle Dynamics*. Warrendale, PA: SAE, 1992.

[26] P. H. Zipfel, *Modeling and Simulation of Aerospace Vehicle Dynamics*, J. Przemieniecki, Ed. Reston, VA: AIAA, 2000.

[27] W. Travis, "Methods for minimizing navigation errors induced by ground vehicle dynamics," Master's thesis, Auburn University, May 2006.

Appendices

Appendix A

Stochastic Parameter Identification with an Automotive-Grade IMU

This appendix serves to demonstrate the parameter identification techniques of Allan variance and autocorrelation on automotive-grade inertial measurements. The techniques are used to identify parameters of the assumed stochastic model from accelerometers and rate-gyros from a Crossbow IMU-400C logged using a PC with Windows XP via an RS-232 serial connection.

The accelerometers and gyros were logged at a sample frequency of $f_s = 5$ Hz for approximately 48 hours in a climate controlled office while resting on a level desk. The mean is removed from each sensor log and the outputs are filtered to reveal any underlying drifting bias. Figure A.1 shows the three Crossbow accelerometers zero-phase filtered (Matlab filtfilt() function) with a second-order low-pass Butterworth filter with cutoff frequency of 0.001 Hz. Figure A.2 shows the zero-phase filtered rate-gyros (second-order Butterworth with 0.001 Hz cutoff frequency).

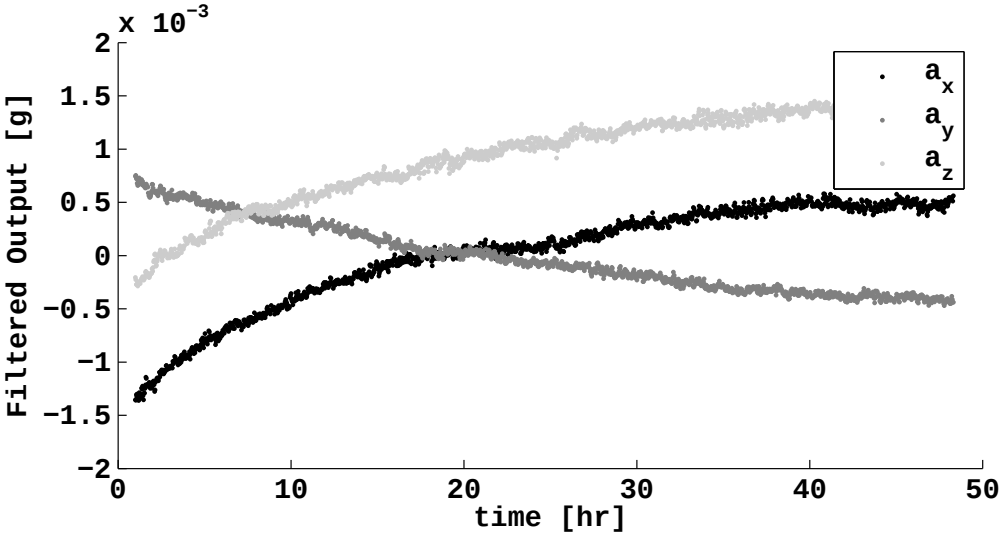

Figure A.1: Filtered Accelerometer Outputs

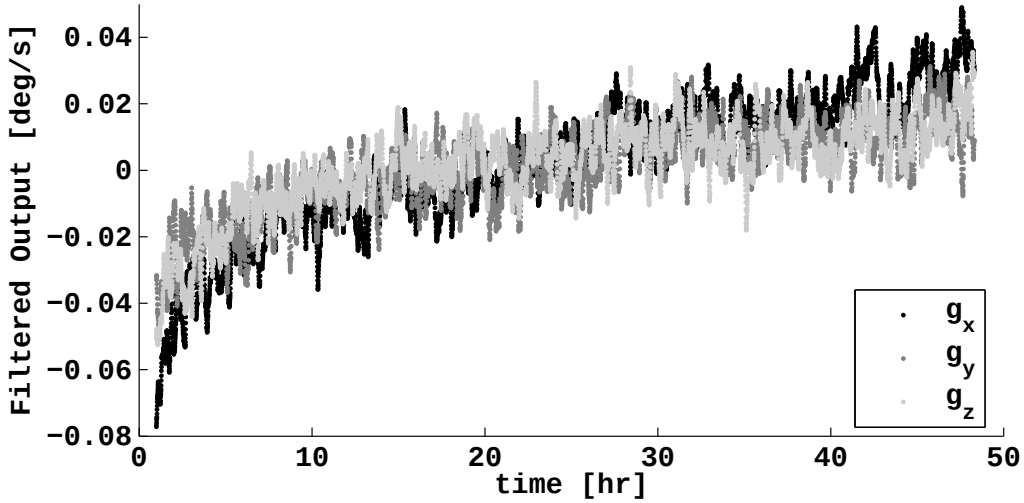

Figure A.2: Filtered Gyro Outputs

As can be seen in both sets of filtered outputs, the sensors exhibit a very slow drifting behavior over the 48 hour logging period. While this slow drift may effect navigation system performance for long spans of time, it is of primary interest to understand the drifting behavior within short time intervals (the intervals for which the sensors will be used to dead-reckon). In order to employ the identification techniques using the assumed Gauss-Markov model, focus is turned to the most steady of the outputs: the z-axis gyro, g_z, within its most constant interval from hour 20 to 45.

Figure A.3 shows the raw and filtered data for the g_z gyro within the interval selected. The data within this interval is filtered to remove the high frequency content of the wide-band noise, leaving the drifing bias for identification with the autocorrelation method. The filtered data shown in the plot was processed with the same low-pass filter as before with a cutoff frequency of 0.0005 Hz, a value determined after multiple iterations to yield the best identification results with the data used.

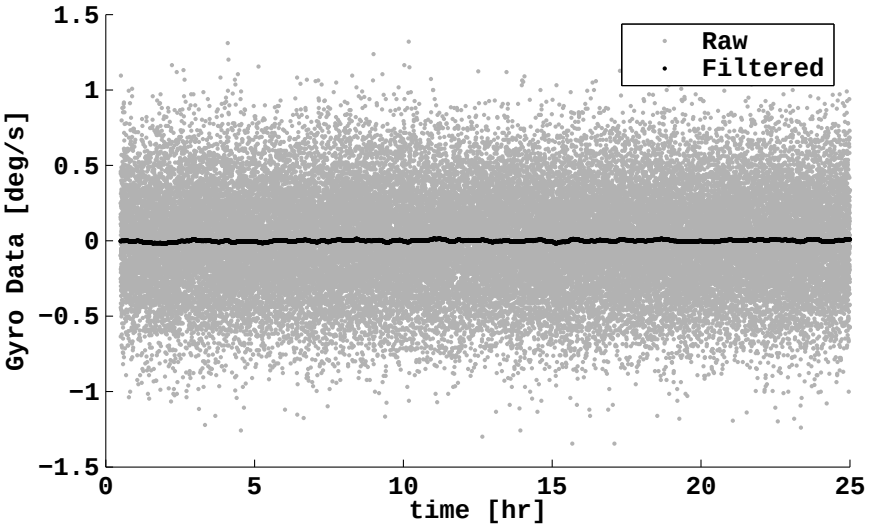

Figure A.3: Raw and Filtered Data Within Selected Section

Figure A.3 shows the filtered data by itself. This plot indicates the relatively long term stability of the selected data, while revealing the characteristic bias drift of interest.

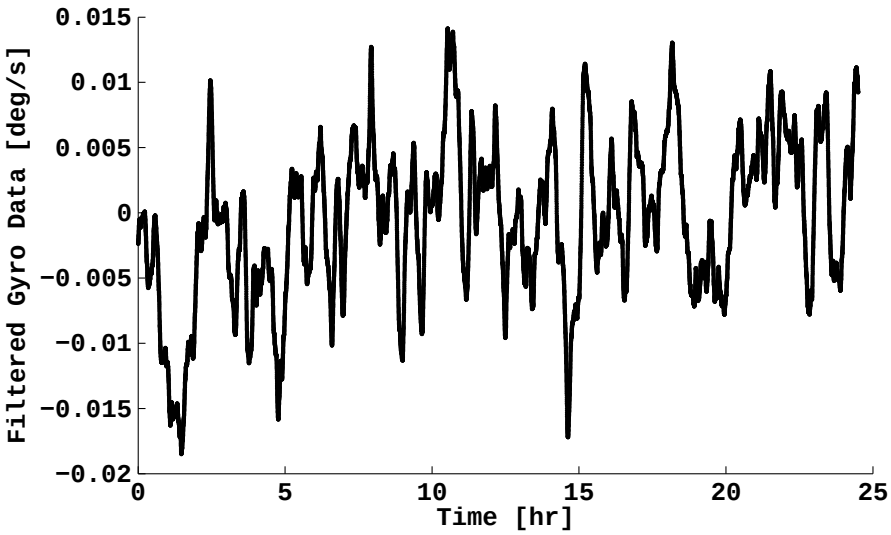

Figure A.4: Filtered Data Within Selected Section

The sectioned and filtered data is then processed with an autocorrelation function. The result is shown in Figure A.5. The run reveals an exponential function such as that exhibited by the Gauss-Markov model. From this data, the time constant is extracted by selecting the intersection on the $\frac{1}{e}$ horizontal line and the variance from the y-intercept. Note that these parameters are extracted only with the confidence reflected by the bound as shown which is referenced around the best-fit line.

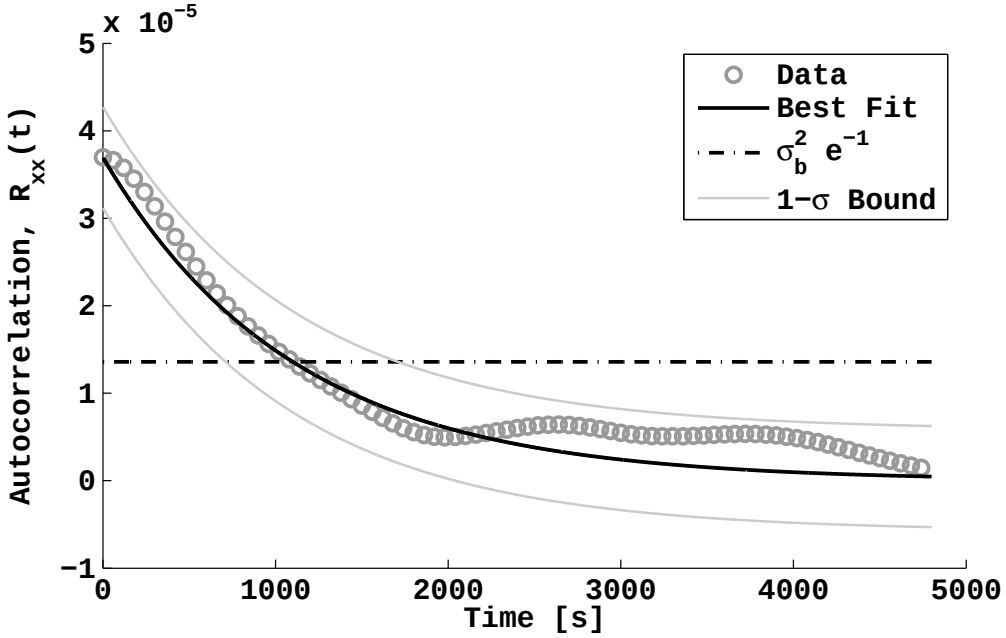

Figure A.5: Autocorrelation of Filtered Gyro Data

Now that rough Gauss-Markov parameters are identified, an Allan variance calculation is performed on the raw experimental data within the section selected. Figure A.6 shows the results of the Allan variance.

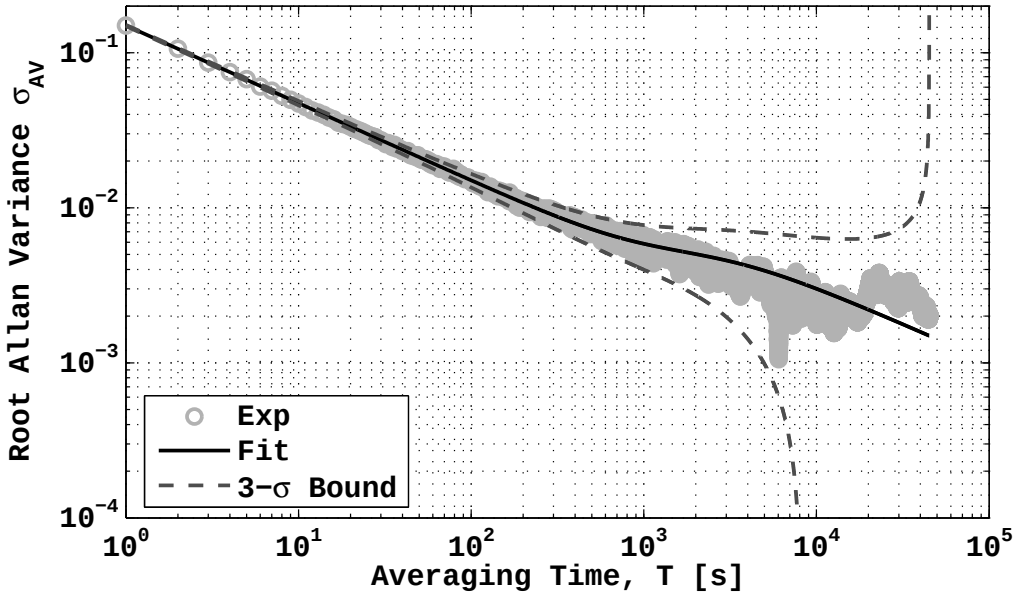

Figure A.6: Allan Variance of Gyro Data

Simple inspection of the Allan variance allows extraction of the random walk parameter (y-intercept of the graph); this parameter quantifies the wide-band noise. Using the identified parameters from the autocorrelation and the extracted random walk parameter, a best fit line is constructed and plotted to represent the Allan variance of the experimental gyro data with the assumed model form. The 3-σ bounds, based on the averaging time and total length of the data set (25 hours @ 5Hz) are plotted along with the fit and experimental data. The fit, while showing a fair agreement with the experimental data, is only a conservative representation as reflected by the large and spreading bounds.

Using the techniques above with the gyro data set, the parameters used to represent the rate-gyro of the Crossbow IMU-400C are shown in Table A.1.

Table A.1: Results of Crossbow Gyro Identification

Gyro Spec	Value
f_s	5 Hz
σ^2_{rw}	0.14963 deg/s/sqrt(Hz)
σ^2_b	0.0061 deg/s
τ	1100 seconds

As shown on the plots of Allan variance and autocorrelation, the bounds on the accuracy of each are very large. These bounds need to be smaller to reflect high confidence in the parameter estimation. Higher levels of confidence require longer sets of data. However, as shown by the long-term behavior of the filtered IMU outputs, it is difficult to ascertain a long set of static data stable enough to employ the techniques with the assumed model forms.

Appendix B

Demonstration of 6-DOF Mechanization of Experimental Inertial Measurements Taken at Talledega Superspeedway

This appendix serves to demonstrate the 6-DOF mechanization of an automotive grade 6-DOF IMU in a medium-sized vehicle traveling around a track at high speeds. The experimental setup is as follows. An Infiniti G-35 sedan was equipped with a single antenna Novatel Starfire^{TM} DGPS ($<$ 10cm accuracy) receiver mounted on a roof rack roughly in the planar center of gravity (CG) of the car. An automotive-grade Crossbow IMU-400C 6-DOF IMU was attached rigidly to the console of the vehicle, which is roughly located at the vehicle's CG. GPS position, velocity, and course was logged at 5 Hz from the GPS, and inertial measurements were logged at 133Hz from the IMU via RS-232 serial connections to a PC in the trunk running Windows XP. For a more complete description of the vehicle test-bed and data acquisition system see [27]. The data used in this appendix was logged with the experimental vehicle and sensors while driving 3 laps around the 2.66 mile track at Talledega superspeedway (Talledega, AL) for approximately 6.5 minutes. The track has bank angles of about 33 degrees in the turns, 16.5 degrees in the tri-oval, and 3 degrees in the straights. The inertial data logged during the laps was post-processed using the 6-DOF mechanization equations presented in Chapter 5 to provide position, velocity, and attitude in the North, East, Down (NED) coordinate system. The inertially-derived values are compared to the high-accuracy GPS information to show its performance in dead-reckoning.

Figure B.1 shows the North and East position from the 6-DOF mechanization of the IMU as compared to the GPS position. It is immediately evident that the dead-reckoning position from the IMU quickly drifts away from the true position of the track (represented by the sub-10cm GPS position). As time elapses for each lap around the track, the IMU-derived position, while coarsely resembling the ovular shape of the true trajectory, drifts with increasing variance from the actual position.

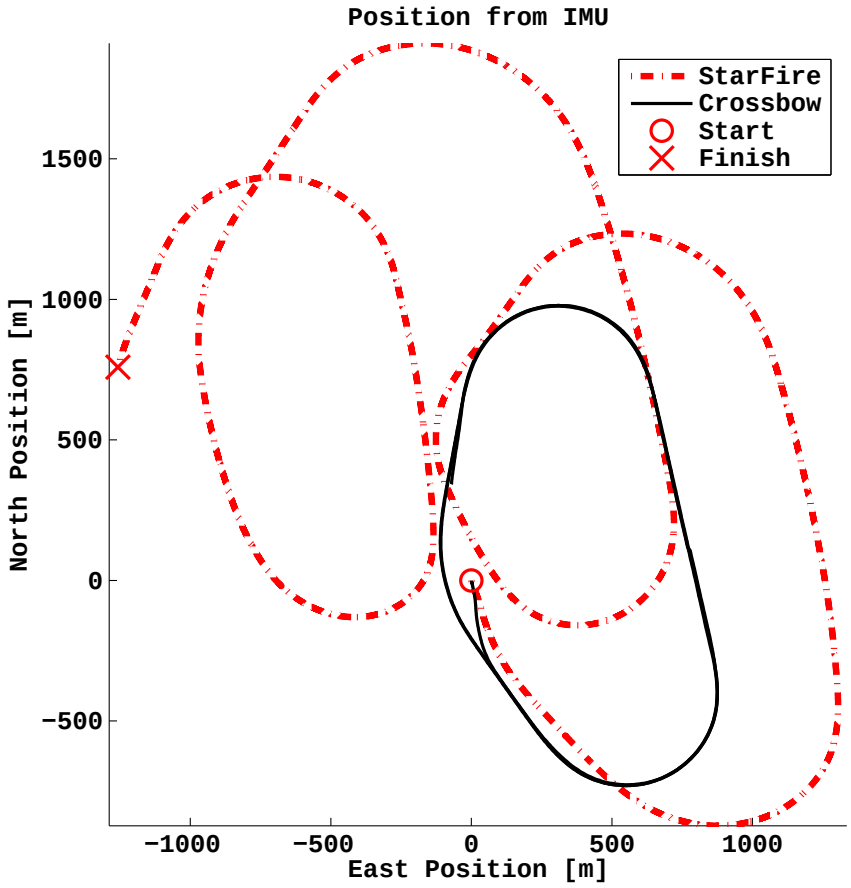

Figure B.1: Position of Track from Starfire GPS

Figure B.2 shows the velocity of the runs around the track as reported by the GPS receiver. As is shown, the large track allowed for velocities higher than are generally allowed on public highways.

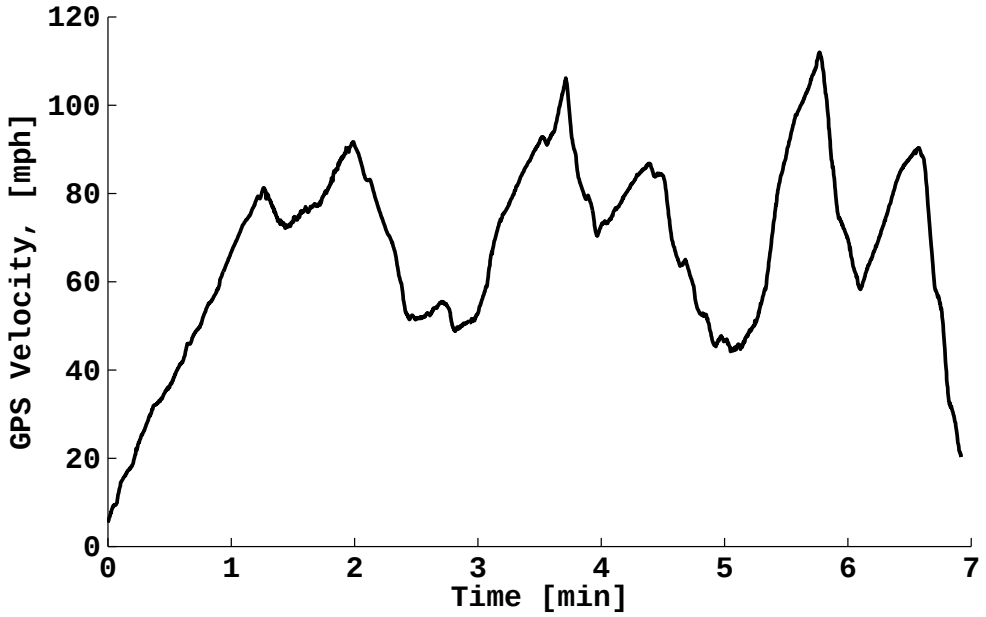

Figure B.2: Velocity from GPS

Figure B.3 shows a comparison of the yaw angles from the IMU and GPS as the vehicle travels around the track. For the high speed and moderate banked turns around the track, the true heading and course are expected to be the same (no vehicle side-slip). As time progresses however, the heading derived IMU drifts from the GPS-reported orientation due to the integration of the stochastic errors present on the three gyros used to compute the yaw angle.

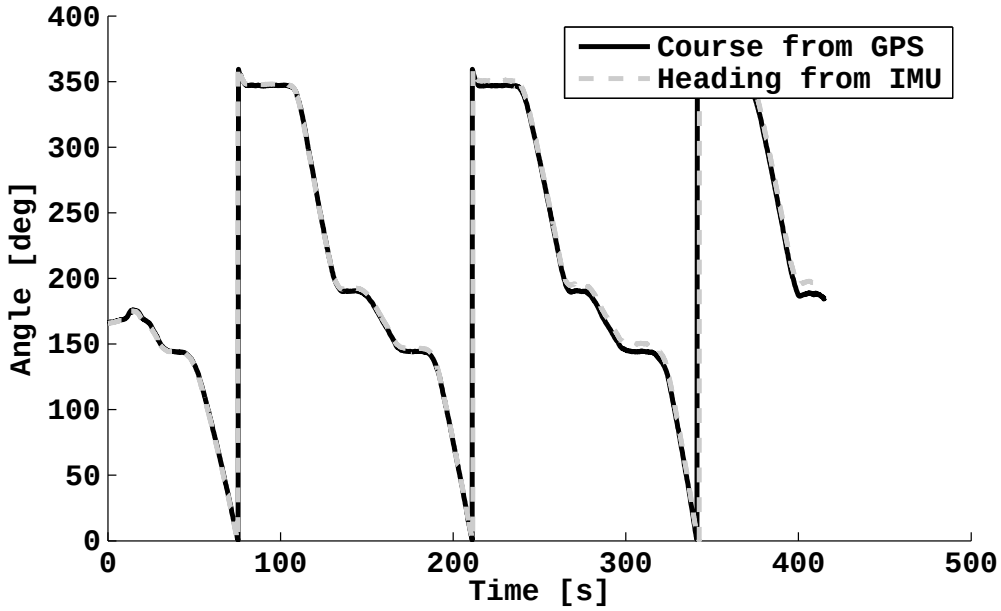

Figure B.3: Yaw Angle (Heading) from IMU

Figure B.4 shows the roll and pitch angles as purely derived from the IMU. As only a single antenna GPS was logged during the test, no un-biased estimate of these angles was available and so only the IMU-derived angles are shown. With knowledge of bank angles of the track, however, it is evident that the values of roll match fairly well to the slope of the track in the turns and straights.

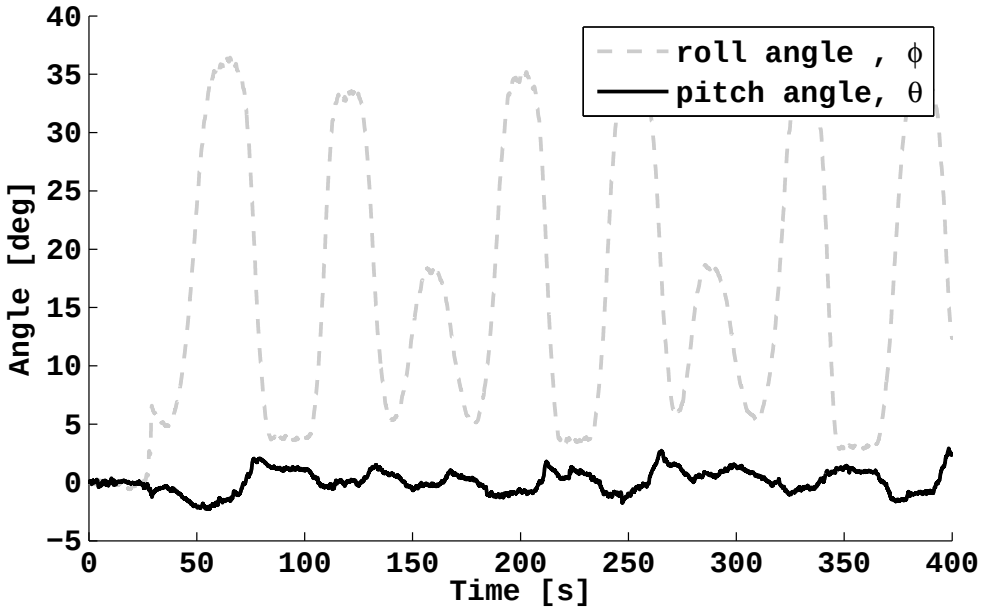

Figure B.4: Roll and Pitch Angles from IMU

Figure B.5 shows of comparison of the North and East component velocities from the IMU and GPS. As shown, the IMU component velocities resemble the shape of the trajectory but drift with increasing distance from the GPS values.

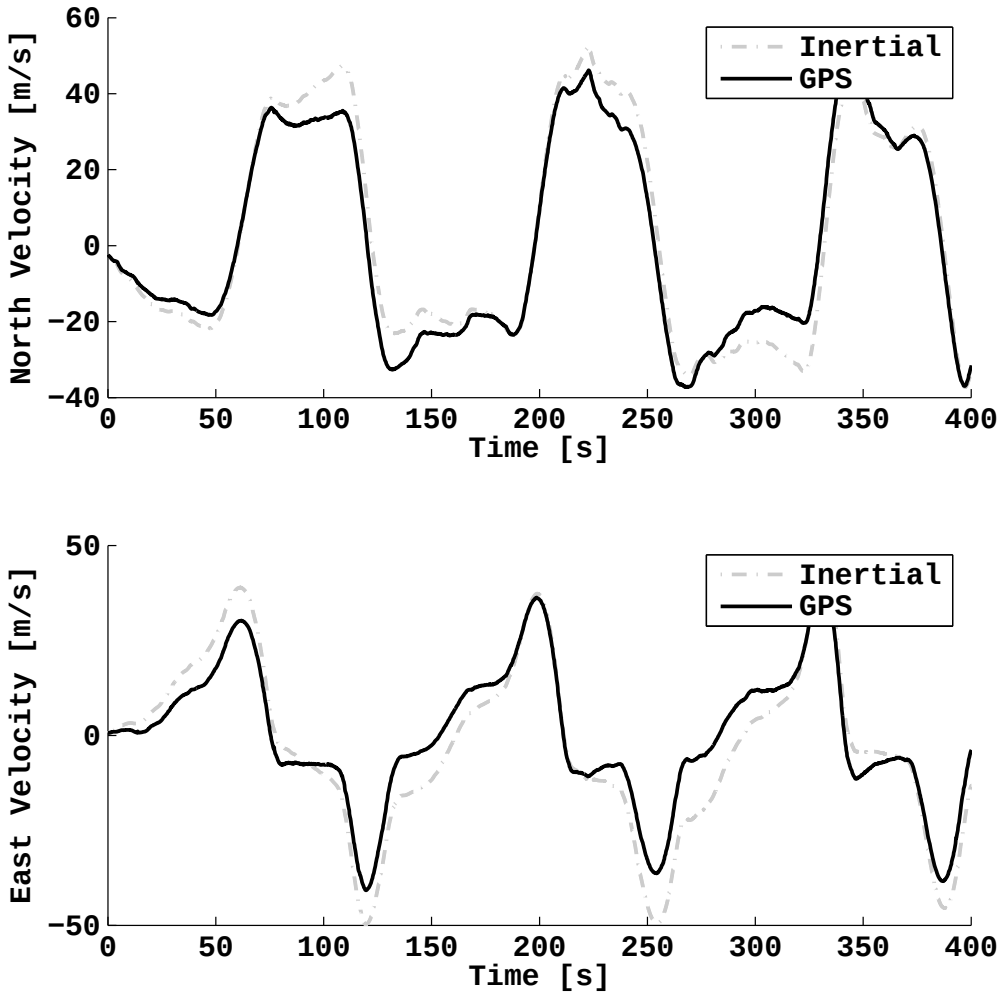

Figure B.5: North and East Component Velocities

Figure B.6 shows of comparison of the North and East component positions from the IMU and GPS. As shown, the IMU component positions resemble the shape of the trajectory but drift with increasing distance from the GPS values. It is evident that when compared to the velocity subplots of Figure B.5, the position error grows at a faster rate. Due to the additional level of integration (once more than velocity) of the stochastic sensor errors, this accelerated rate in position error growth is expected.

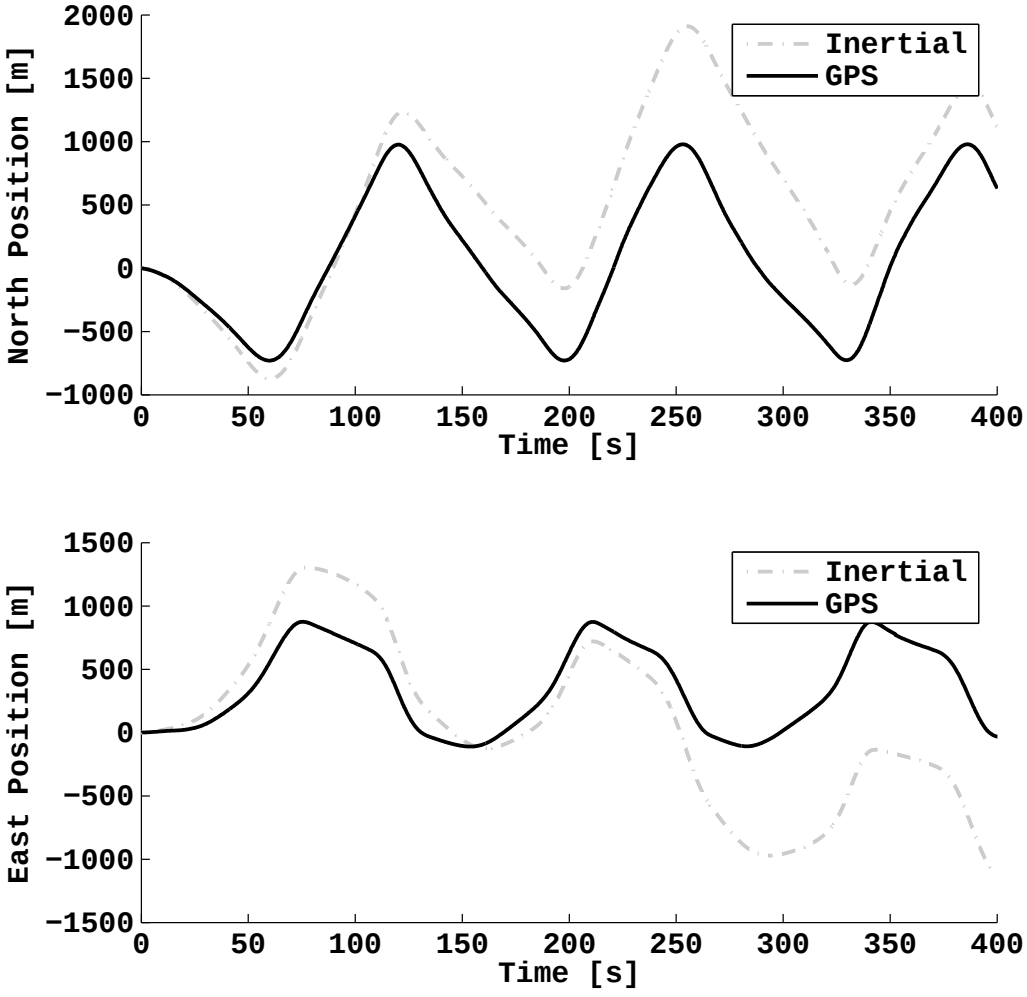

Figure B.6: North and East Component Positions